A Dissertation

entitled

Theories of Charge Transport and Nucleation in Disordered Systems

by

Marco Nardone

Submitted to the Graduate Faculty as partial fulfillment of the requirements

for the Doctor of Philosophy Degree in Physics

Dr. Victor G. Karpov, Committee Chair

Dr. Patricia Komuniecki, Dean
College of Graduate Studies

The University of Toledo
December 2010

An Abstract of

Theories of Charge Transport and Nucleation
in Disordered Systems

by

Marco Nardone

Submitted to the Graduate Faculty as partial fulfillment of the requirements
for the Doctor of Philosophy Degree in Physics

The University of Toledo
December 2010

A number of analytical theories related to disordered systems have been developed based on two major themes: (1) charge transport in non-crystalline semiconductor systems where localized states play the main role in the underlying mechanisms; and (2) crystal nucleation in the presence of a strong electric field. In this dissertation, five research topics based on these themes are presented: (1) charge transport through non-crystalline junctions; (2) admittance characterization of semiconductor junctions; (3) $1/f$ noise in chalcogenide glasses; (4) electric field-induced nucleation switching in chalcogenide glass threshold switches (TS) and phase change memory (PCM); and (5) relaxation oscillations in PCM. Although the theories are quite general in nature, their practical implications are discussed in the context of thin-film photovoltaics (PV), and chalcogenide glass TS and PCM.

It is shown that, even at practical temperatures, hopping conduction via optimum channels of localized states can be the prevailing charge transport mechanism in semiconductor junctions. That type of transport results in laterally nonuniform current flow that leads to shunting, device degradation, and variations between identical devices. Analytical expressions have been derived that relate important device characteristics, such as the diode ideality factor, saturation current, and open circuit voltage, to material parameters; the results are in agreement with experimental data.

Consideration of the laterally nonuniform current formed the basis of the phenomenological theory of admittance spectroscopy that properly accounts for the decay of an a.c. signal in a semiconductor structure with resistive electrodes. The theory facilitates a more informative analysis of admittance measurements, including additional device characteristics and the distribution of shunts. An important new insight is that blocking the entrance to the optimum channels, perhaps with surface treatments, can improve the performance of thin-films devices.

Localized atomic and electronic excitations, and generation-recombination processes in chalcogenide glasses are internal degrees of freedom that can cause low frequency current noise. On that basis, several mechanisms of $1/f$ noise are analyzed and quantified in terms of the standard measure of the Hooge parameter. Six experimentally testable expressions are derived with varying dependencies on material properties. Based on existing data, the most likely cause appears to be electronic double-well potentials (two-level systems) related to spatially close intimate pairs of oppositely charged negative-U centers.

The field-induced nucleation model describes how crystallization occurs in the presence of a strong electric field. As a thermodynamic model, it predicts in analytical form the observed features of threshold switching, including the characteristic voltages, delay time, and statistics. Here it is shown how the model forms a unifying framework for switching in chalcogenide TS and PCM devices, as well as others, which were previously considered to be fundamentally different. The unity is manifest in relaxation oscillations that are observed in both TS and PCM. Results for relaxation oscillation experiments are presented and discussed in terms of the field-induced nucleation model.

To my Father, Pietro Nardone

“Ci vuole solo la volontà”

Acknowledgments

I gratefully acknowledge the University of Toledo College of Graduate Studies for three years of financial support through the University Fellowship. I would also like to thank the Department of Physics and Astronomy, especially the office staff, for their guidance and support. Many thanks to Dr. ILya Karpov, not only for directing the financial support through Intel Corporation, but also for his patient mentoring throughout my studies and hospitality during my visit to Intel's headquarters.

I would like to thank my committee, especially Dr. Victor Karpov, my advisor. Not only did Dr. Karpov teach me the techniques that are essential in the trade of real-world physics, but his contagious passion for the pursuit of honest science was inspiring and will stay with me throughout my career. Striving for his creativity and depth of knowledge will always be a goal of mine.

My decision to pursue a Ph.D. in physics was a significant career change and I thank my parents and the rest of my family for always believing in me. Words cannot express my appreciation for my wife, Shannon Orr. If not for her unconditional love, support and encouragement, I would surely not have been able to achieve this goal. Because of her, this long and uncertain road has been a joyful and enriching experience. To my daughter Isabella, I am thankful for all the smiles, the laughter, and the reminder of the importance of a child-like curiosity.

Contents

List of Tables

List of Figures

Chapter 1

Introduction

Thin films of semiconducting material play an increasingly important role in modern technology. Such films are typically noncrystalline in structure, being polycrystalline, amorphous, or glassy, depending on the method of fabrication and chemical composition. Their disordered nature results in unique and useful characteristics but it also leads to technical challenges related to shunting, degradation over time, and manufacturing consistent and highly efficient devices. In addition, there are associated scientific challenges in theoretical understanding, numerical simulation, and experimental classification. The complexities are often amplified by the necessity of forming junctions between these materials and other semiconductors, metals, or insulators.

The purpose of this work is to provide a sound theoretical basis for the following disorder related phenomena:

1. Laterally nonuniform current flow in noncrystalline junctions that causes shunting, non-ideal behavior, degradation, and statistical variation between identical devices.

2. Admittance spectroscopy measurements on thin-film systems that have resistive electrodes and nonuniform current flow.

3. Low frequency current noise in chalcogenide glasses.

4. Similarity in the switching behavior of chalcogenide threshold switches (TS) and phase change memory (PCM), in particular, relaxation oscillations that have been observed in both types of devices.

The theories developed herein are rather general in nature, but for the sake of practicality and comparison to experimental data the focus is on thin-film photovoltaic (PV) devices and chalcogenide glass TS and PCM. Background information on these technologies is presented later in this chapter.

Although this work consists of a broad range of research topics, there are two major themes: (1) the effects of localized states on charge transport; and (2) phase transitions in the presence of a strong electric field. Given these two themes, the theories presented herein have evolved from the following hypotheses:

1. The established theory of optimum channel hopping in thin amorphous films can be applied to charge transport through non-crystalline junctions.

2. Consideration of resistive electrodes, lateral current flow, and laterally nonuniform material properties can lead to a more informative interpretation of admittance spectroscopy measurements.

3. Elemental fluctuators, such as localized atomic and electronic excitations in chalcogenide glasses, can be the underlying cause of the observed $1/f$ noise.

4. The theory of electric field induced nucleation can provide a common framework for understanding threshold switching and oscillations in TS and PCM, as well as other devices.

In this dissertation, Chapter 2 presents a theoretical basis for electronic transport via localized states in noncrystalline junctions that explains many of the observations related to nonuniform current flow. One consequence of nonuniform current is spatially separated "hot spots" of high current that lead to device inefficiency and

degradation. In Chapter 3, a theory of admittance spectroscopy is advanced that provides a diagnostic method for identifying the current hot spots (or shunts), along with other information that is not ascertainable from standard admittance techniques. Several conceivable mechanisms of $1/f$ noise related to the flexible nature of localized states in chalcogenide glasses are presented in Chapter 4. Chapters 5 and 6 present the theory of field-induced crystal nucleation as a unifying framework that describes relaxation oscillations in the seemingly different TS and PCM devices. Throughout this work, most of the data referred to is extracted from other sources, with the exception of the chapter on relaxation oscillations which presents the results an original comprehensive experimental study.

The following subsections provide background on the technological applications relevant to this work. For reference purposes, a comprehensive list of experimental observations and a table of typical parameter values for TS and PCM are provided in Appendix A.

1.1 Thin-Film Photovoltaics

Thin-film PV technology embodies a class of semiconductor devices that are non-crystalline in nature. Compositions of practical significance include hydrogenated amorphous silicon (a-Si:H), polycrystalline Cadmium Telluride (CdTe), and Copper Indium Gallium Selenide (CIGS). They are typically referred to as second generation devices, superseding the first generation of single-crystal PV cells. The advantages of thin films are lower material costs and amenability to large area, continuous flow manufacturing. The disadvantages include lower efficiency, faster degradation, and, in many cases, limited material feedstock.

Charge transport through semiconductor p/n or metal/semiconductor junctions often governs the overall performance of PV devices. The current state of under-

standing is that transport in noncrystalline junctions is similar to the classical band transport of crystalline junctions, with recombination processes limited to band to band [1] or single defect level mechanisms, such as Shockley, Read, Hall (SRH) [2] or Sah, Noyce, Shockely [3]. The work herein presents a theory of electronic transport in noncrystalline junctions which challenges the standard viewpoint and explains many of the typical yet puzzling observations; such as ideality factors greater than two, differences in identical devices, and rollover recovery in current/voltage (IV) curves under forward bias.

One unique feature of non-crystalline semiconductors is the high density of localized states in the mobility gap that is known to give rise to hopping transport, which dominates at low temperatures. Although at temperatures of practical interest, the primary transport mechanism in *bulk* materials is typically band conduction, hopping transport can dominate in *sufficiently thin* non-crystalline materials at room temperature or higher [4]. The viewpoint adopted here is that junctions in noncrystalline PV devices can form such thin structures and the related physics can dictate device operation and explain the observed phenomena.

1.2 Phase Change Memory and Threshold Switches of Chalcogenide Glasses

The unique phase transformation properties of chalcogenide glasses has made them ubiquitous in information storage technology. The predominant alloy in use is comprised of Germanium (Ge), Antimony (Sb), and Tellurium (Te) with stoichiometry $Ge_2Sb_2Te_5$. The ability of the material to repeatedly switch back and forth from amorphous to crystalline phases has made possible the technology of optical discs wherein the phase change is caused by laser induced heating of a small region of the device. In optical discs, the phase change is characterized by a dramatic change in the

reflectivity of the material which can be detected by a low intensity laser. Therefore, controlled differences in the reflectivity comprise the bits of data with "off" as high reflectivity and "on" as low reflectivity. Optical disc technology has proved to be reliable and practical.

Phase Change Memory (PCM) also exploits the switching property of chalcogenide glasses to enable state-of-the-art, non-volatile computer memory. Instead of using a laser to heat the material, a controlled electrical pulse is applied to induce the phase change. The abrupt phase change of the material not only results in a change in reflectivity but also a dramatic change in electrical resistance, with the amorphous phase having high resistance (reset state) and the crystalline phase having low resistance (set state). A lower voltage is applied to read the state of a small region of the device without disrupting the phase. PCM devices have promise to be faster and more robust than other types of non-volatile memory.

In threshold switches (TS), a sustaining voltage (or holding voltage) is required for the low resistance state to exist, while for memory switches no holding voltage is required and the low resistance state persists without outside influence. In either case, switching back to the high resistance state can be accomplished by application of an appropriate voltage pulse. Although only memory switching is employed in PCM devices, the commonalities between threshold and memory switching require investigation of both to develop a more complete understanding. In fact, it is shown in Chapter 5 that the field-induced nucleation model can describe the observed switching phenomena in both TS and PCM.

Theoretical models of switching in chalcogenide glasses can be divided into three broad categories, namely, thermal, electronic and electric field-induced nucleation. Although most researchers agree that both thermal and electronic processes play important roles in the observed phenomena, the predominant voice in the literature since the mid-1970s has been in favor of electronic models for understanding thin

devices (i.e. thickness less than 10 μm) [5]. In this work we show that a more complete understanding can be gained from the field-induced nucleation model.

The various electronic models [5, 6, 7, 8, 9, 10, 11] purport that switching is initiated by an electronic 'hot' filament that can (in PCM) or cannot (in TS) trigger crystal nucleation. The implication is that TS remains amorphous in the low resistance state, i.e. a highly conductive glass, while in PCM a crystalline filament forms some time after the hot filament. Related numerical models have been developed [11] based on an extension of crystalline physics and the use of customizable semiconductor modeling software. The numerical models are able to successfully reproduce several experimental results, but they are based on a large set of tunable parameters. Moreover, the progress made with electronic models has not provided a clear understanding of the characteristic voltages and currents or the statistical behavior of switching (e.g. distribution of threshold voltages and delay time).

Recently, our group developed an analytical theory of switching in chalcogenide glasses based on crystal nucleation induced by an electric field [12, 13, 14]. The motivations were:

1. the statistical nature of the phenomenon;

2. the need for a quantitative theory relating device characteristics to material and external parameters; and

3. the understanding of glasses that has accumulated since the 1970s.

In conjunction with the theory, unique experiments were conducted to study switching under conditions far beyond the standard. Also studied were the statistics of switching events and relaxation oscillations in PCM devices [15, 16, 17]. A brief description of the field induced nucleation model is provided in Chapter 5.

Chapter 2

Electronic Transport in Noncrystalline Junctions

Junctions between two non-crystalline semiconductors or between a non-crystalline semiconductor and a metal underly the operation of many important devices of modern technologies. One important feature of non-crystalline materials is the high density of localized states in the mobility gap. Such states are present in many materials that form junctions of practical significance, such as a-Si:H based structures [18], polycrystalline CdTe [19], and CIGS [20] (all used in thin-film photovoltaics), and junctions in phase change memory devices [21] based on chalcogenide materials that can be in either glassy or polycrystalline states.

A high density of localized states $[g_0(E_F)]$ at the Fermi level (E_F) in non-crystalline semiconductors is known to give rise to hopping transport which dominates at low temperatures (T) and is described by the Mott law [22],

$$\sigma = \sigma_0 \exp\left[-\left(\frac{T_0}{T}\right)^{1/4}\right], \quad T_0 = \frac{\beta}{k g_0 a^3}, \tag{2.1}$$

where k is the Boltzmann constant, a is the localization radius of the electron wave function, and β is a numerical factor. However, at room or higher T of practical interest, the primary transport mechanism in bulk materials is typically band con-

duction. This may suggest that transport in non-crystalline junctions is similar to that of their crystalline counterparts. Indeed, most non-crystalline device modeling tacitly assumes classical band transport.

As a challenge to advocacy of the latter understanding, this work concentrates on hopping transport through non-crystalline junctions. Our rationale is that transverse hopping through non-crystalline thin films, with thicknesses in the micron or sub-micron range, is known to be qualitatively different and relatively much more efficient than in bulk materials. The concept of gigantic transverse hopping conduction through thin films was introduced by Pollak and Hauser [23] and later developed in a number of works summarized in the review by Raikh and Ruzin [24].

We recall that in bulk materials hopping occurs on the macroscopically isotropic percolation cluster with the characteristic mesh size well below the sample linear dimensions [25]. However, when the film (or junction) thickness L_0 falls below a certain critical value L_c, the transverse conductivity shows exponential thickness dependence described by [24]

$$\sigma = \sigma_0 \exp\left(-2\sqrt{\frac{2L_0\lambda_T}{a}}\right), \tag{2.2}$$

with $\lambda_T \approx \ln\lambda_T - \ln(g_0 kTaL_0^2)$ and is governed by the 'untypical' hopping chains of spatially close localized states, as illustrated in Fig. 2-1(a). Although comprised of exponentially rare configurations of localized states, these chains are exponentially more conductive than the hopping pathways of percolation clusters due to the reduced tunneling distance between states.

The critical thickness can be estimated by setting equal the exponents in Eqs. (2.1) and (2.2):

$$L_c \sim \frac{a}{\lambda_T}\sqrt{\frac{T_0}{T}}. \tag{2.3}$$

Assuming the typical parameters [22, 23] $a \sim 1$ nm, $\lambda_T \sim 10$, and $T_0 \sim 10^8 - 10^9$ K yields $L_c \lesssim 1$ μm; consistent with the experimentally estimated [23] $L_c \sim 0.4$ μm for

a-Ge films. For thin films and junctions with $L_0 < L_c$, transverse hopping becomes exponentially more efficient and can become dominant even when the bulk conduction is due to band transport.

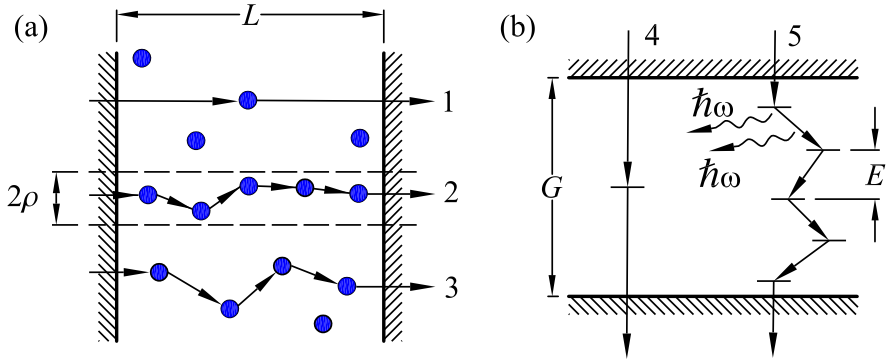

Figure 2-1: Charge transport via optimal chains in (a) real space and (b) energy space. (a) three different channels of length L_0 corresponding to: (1) lower than average localized state concentration with a 2-step (one defect) chain; (2) optimum chain with radius ρ having a number of defects greater than the average; and (3) 'average' chain whose configuration is most likely, yet the transmission rate is exponentially low. (b) two different ladders corresponding to recombination through the gap G via: (4) one state located near mid-gap, similar to Ref. [2]; and (5) optimum ladder with N steps and multiple phonons of energy $\hbar\omega$ emitted per step.

Along with the above described hopping in real space, there is a similar hopping process through the energy space of the mobility gap [26] which provides an effective mechanism for nonradiative recombination in non-crystalline semiconductors. As shown in Fig. 2-1(b), clusters of localized states facilitate recombination by forming ladders in energy space. The interband transition of charge carriers occurs via such states where each step in energy E is accompanied by the simultaneous emission of multiple phonons. These ladders exponentially increase the recombination rate by decreasing the number of phonons $M = E/\hbar\omega$ required per step of energy E (more detail is provided in Sec. 2.1.1). The resulting recombination rate is described by

[26],

$$R \propto \exp\left(-2\sqrt{\frac{G\lambda_E}{\varepsilon}}\right), \tag{2.4}$$

where G is the width of the mobility gap, ε is on the order of the characteristic phonon energy (~ 0.01 eV), and $\lambda_E = \ln\left[8\varepsilon^{1/2}/(27ga^3G^{3/2})\right] \gg 1$; here, the density of localized states g is assumed to be independent of energy. Recombination via ladders can be orders of magnitude greater than through a single defect [see Fig. 2-1(b)] where the necessity to emit $M = G/(2\hbar\omega) \gg 1$ phonons makes the recombination rate proportional to $\exp\left[-G/(2\varepsilon)\right]$.

The purpose of this chapter is to develop a theory of electronic transport in non-crystalline junctions based on hopping conduction. To this end, we extend the previous work [23, 24, 26] by considering optimal chain hopping transport simultaneously in real space (through the junction) and energy space (through the mobility gap) forming 'hopping channels', as illustrated in Fig. 2-2(b). As a specific example, we will describe the current voltage (IV) characteristic relating the current density J (A/cm^2) to the applied voltage V applicable to junctions in non-crystalline photovoltaics (PV).

We recall that the standard IV characteristic is given by

$$J = J_0\left[\exp\left(\frac{qV}{AkT}\right) - 1\right] - J_L, \tag{2.5}$$

where q is the electron charge, A is the diode ideality factor, and J_L is the photogenerated component. According to the classical model [1, 27], the forward current is due to thermal activation over the junction barrier W_0 [see Fig. 2-2(a)] with a probability proportional to $\exp(-W_0/kT)$. Because in equilibrium the forward current $J_{00}\exp(-W_0/kT)$ is balanced by the reverse current $J_0 \equiv J_{00}\exp(-W_0/kT)$, where J_{00} depends on material parameters, the IV characteristic takes its standard form in Eq. (2.5) with $A = 1$ and where $qV = \Delta W$ is the bias induced change in the junction

barrier height. Another known mechanism [3], also sketched in Fig. 2-2(a), includes recombination via a single energy level, so that the electron and hole overcome comparable activation barriers $\approx W_0/2$ corresponding to $A = 2$ in Eq. (2.5).

More recent work [28] considered tunneling-enhanced recombination via localized states in the space charge region and the energy distribution of those states in heterojunctions (the idea of tunneling was put forward earlier [29] in connection with the mechanism of thermionic emission through Schottky barriers). The resulting IV characteristics displayed the appropriate temperature dependence and allowed for ideality factors $A > 2$ at low temperatures. However, the concept and consequences of optimal channel hopping were not considered.

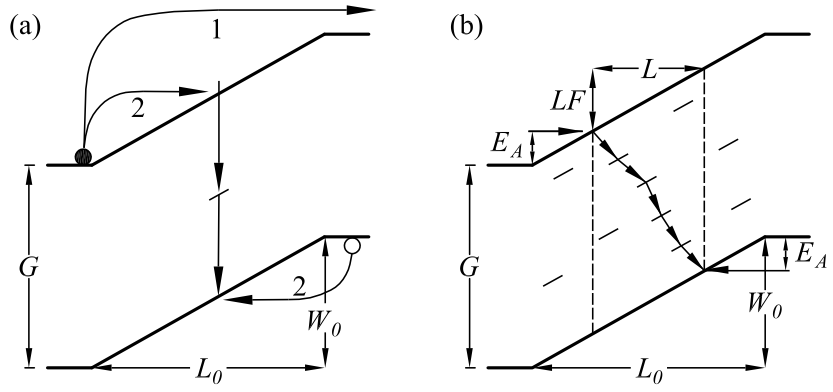

Figure 2-2: (a) Arrow 1 represents the classical model of forward current due to thermal activation over the junction barrier W_0, upon which the electrons and holes recombine; arrows 2 represent the mechanism of forward current due to recombination via a single energy level [3]. (b) Our proposed model of multi-step recombination channels for a simplified p-n junction of length L_0, barrier W_0, and linear built-in field F. G is the mobility gap. An electron is thermally activated to an energy E_A and tunnels via N steps through a channel of length L and total energy $G - LF$.

2.1 Recombination and Generation Channels

According to our model, nonradiative electronic processes in non-crystalline junctions evolve by hopping between localized states that form compact clusters (in real and energy space), which we refer to as channels. We consider systems of random localized states in non-crystalline junctions and we describe how recombination and generation are dominated by certain optimum channels which are, generally speaking, different for these two processes.

2.1.1 Recombination Channels

Our model assumes hopping between localized states that are closer to each other than the average distance, as illustrated in Fig. 2-1(a). Such clusters of states will play the role of recombination channels (extending the concept of recombination centers), whose parameters include the number N of participating localized states, the channel length L and radius ρ, and the activation energy E_A that the electrons and holes must overcome in order to enter the channel [refer to Figs. 2-2(b) and 2-3].

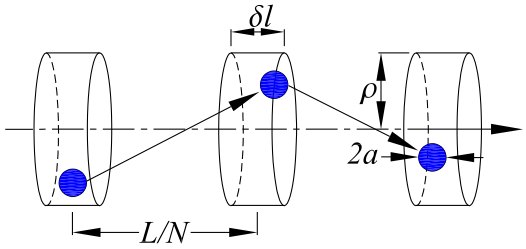

Figure 2-3: Geometric parameters of the optimum channel; δl is the dispersion in axial coordinate, L/N is the average inter-center distance, and a is the localization radius.

Upon entering the channel, each step in energy E requires the simultaneous emission of M phonons, each with energy $\hbar\omega$. The probability of exchanging energy E into $M = E/\hbar\omega \gg 1$ phonons is proportional to [22, 26, 30] $p_{ph}^{M} = \exp(-E/\varepsilon)$ with

$\varepsilon = \hbar\omega/[\ln(1/p_{ph})]$, where $p_{ph} \ll 1$ is the one-phonon probability. The total energy E of the phonons emitted at one step of the N-step staircase is related to the total energy $E_{tot} = G - LF$ dissipated in recombination via $E = E_{tot}/N$, where F is the built-in field of the junction [see Fig. 2-2(b)].

Based on the above, the probability (per time) of a 1-step electronic transition through energy and real space in a channel is estimated as

$$\nu = \nu_0 \exp\left(-\frac{E}{\varepsilon} - \frac{2R}{a}\right) \tag{2.6}$$

where ν_0 ($\sim 10^{13}$ s^{-1}) is the characteristic phonon frequency and the second exponent describes tunneling across a distance R with a being the localization radius. It follows then that the transition rate for a multiple-step process will exponentially increase with the number of defects N in the channels due to the decrease in both R and E. However, channels with large N are less likely. Therefore, among a variety of possible channels, the most effective recombination pathways will have defect numbers N optimized between high enough transition rates and not too small configuration probabilities. These unlikely yet exponentially efficient *optimum channels* will dominate the junction transport.

We note the following properties of optimum channels [24]: 1) their localized states are almost equidistant in real space and energy space; and 2) the occupation numbers of those states are close to 1/2. The first property is derived from noticing that the exponential dependence in Eq. (2.6) suggests that the transmission rate of a channel will be dominated by its slowest step. Therefore, making other steps shorter than that will not improve the transmission rate, while increasing the number of steps will decrease the probability of channel formation. Hence, the inter-center distances are nearly equal with averages L/N and E_{tot}/N in real and energy spaces, respectively. Yet, as illustrated in Fig. 2-3, some dispersion in the location and energy of the

localized states is required to allow for the formation of anomalously clustered sites. The second property is due to the requirement of equal channel transmission rates for electrons and holes, which implies that all the participating states must have almost equal occupation numbers close to 1/2.

The probability of finding a channel with $N \gg 1$ uncorrelated states is estimated as

$$p_N = p_1^N = (\pi\rho^2\delta l g\Delta)^N \equiv \exp(-N\Lambda), \tag{2.7}$$

with $\Lambda = -\ln(\pi\rho^2\delta l g\Delta)$, where g is the density of localized states (here assumed a constant) and each site lies within an energy interval Δ. In writing the transition probability ν_N of such a chain, we take into account the dispersion of states within the channel radius ρ ($\ll L/N$), which adds to the tunneling distance a small contribution $\delta\rho = \sqrt{(L/N)^2 + \rho^2} - L/N \approx N\rho^2/2L$. Another addition comes from the longitudinal dispersion of states $\delta l \ll L/N$ (refer to Fig. 2-3). As a result, the partial current due to channels of total energy $E_{tot} = G - LF$ and length L becomes

$$q\nu_N p_N \equiv q\nu_0 \exp(-\Phi) \tag{2.8}$$

with

$$\Phi = \frac{G - LF}{N\varepsilon} + \frac{\Delta}{\varepsilon} + \frac{2L}{Na} + \frac{\rho^2 N}{La} + \frac{2\delta l}{a} + N\Lambda. \tag{2.9}$$

The exponential argument Φ has a maximum (Φ_0) as a function of N and other parameters, which we find via minimization $\partial\Phi/\partial\rho = \partial\Phi/\partial\delta l = \partial\Phi/\partial\Delta = \partial\Phi/\partial N = 0$. As a result, we obtain the optimum channel parameters

$$\rho_0 = \sqrt{La}, \quad \delta l_0 = N_0 a, \quad \Delta_0 = N_0\varepsilon, \tag{2.10}$$

with

$$N_0 = \sqrt{\frac{2L}{a\Lambda} + \frac{G - LF}{\varepsilon\Lambda}}, \tag{2.11}$$

where Λ is determined by the equation

$$\Lambda = \ln \Lambda - \ln \left[\pi g L a^2 \varepsilon \left(\frac{2L}{a} + \frac{G}{\varepsilon} \right) \right]. \tag{2.12}$$

As a numerical estimate, we use $L = 10$ nm, $a = 1$ nm, $\varepsilon = 0.01$ eV, $G = 1$ eV, and $g = 10^{16}$ cm^{-3}eV^{-1}, which yields $\Lambda \sim 10$.

Inserting the optimum channel parameters from Eqs. (2.10) and (2.11) into Eq. (2.8) yields the recombination current through one optimum channel of length L,

$$\begin{aligned} I_{opt} &= q\nu_0 \exp(-\Phi_0 + \Lambda N_0) \\ &= q\nu_0 \exp\left[-\sqrt{\left(\frac{2L}{a} + \frac{G - LF}{\varepsilon} \right) \Lambda} \right]. \end{aligned} \tag{2.13}$$

The factor $\exp(\Lambda N_0)$ was included in Eq. (2.13) to account for the fact that the requirement of finding the optimum channel configuration was already imposed in the optimization process. In other words, Eq. (2.13) implies that we are dealing with a particular channel (the optimum one) and, therefore, the factor p_N in Eq. (2.8) can be excluded.

To ensure continuity, the current through the optimum channel from Eq. (2.13) should be matched with the activated current

$$\begin{aligned} I_{act} &= qnv\sigma \exp\left(-\frac{E_A}{kT} \right) \\ &= qnv\sigma \exp\left[-\frac{W_0}{2kT} \left(1 - \frac{L}{L_0} \right) \right] \end{aligned} \tag{2.14}$$

entering the channel, where n is the electron concentration, v is their thermal velocity, and σ is the capture cross-section.

By equating Eqs. (2.13) and (2.14) we obtain a quadratic equation for L with a

solution that reduces to the intuitively transparent form of Eq. (2.13) with $L/L_0 \approx 1$,

$$I_{opt} = q\nu_0 \exp\left[-\sqrt{\left(\frac{2L_0}{a} + \frac{G - L_0 F}{\varepsilon}\right)\Lambda}\right] \tag{2.15}$$

for the case of low temperatures defined by,

$$\alpha \equiv \left(\frac{W_0}{kT}\right)^2 \frac{a}{2L_0\Lambda} \gg 1. \tag{2.16}$$

On the other hand, in the high-T regime determined by the opposite inequality, one can write $L/L_0 = \alpha\beta \ll 1$ with

$$\beta \equiv \left[1 + \frac{2kT}{W_0} \ln\left(\frac{\nu_0}{n\sigma v}\right)\right]^2 - \frac{G\Lambda}{\varepsilon}\left(\frac{2kT}{W_0}\right)^2, \tag{2.17}$$

where the logarithmic term can be rather large; $\ln(\nu_0/n\sigma v) \sim 20 - 30$.

Our formulation leads to two critical temperatures that are defined by: 1) a low temperature regime ($T \lesssim T_l$) where tunneling through real space is the primary mode of transport; and 2) a high temperature regime ($T \gtrsim T_h$) where tunneling is suppressed and Eq. (2.14) describes recombination with activation energy $W_0/2$ and $A = 2$, matching a single defect model [3]. By using numerical values of $\Lambda = 10$, $a = 1$ nm, $L_0 = 1000$ nm, $W_0 = 1$ eV, $G = 1$ eV, and $\varepsilon = 0.01$ eV, we estimate $T_l \approx 100$ K from the condition of Eq. (2.16) and $T_h \approx 1000$K defined by the condition $L \propto \beta = 0$. Therefore, our model predicts that a combination of activation and tunneling transport occurs at typical operating temperatures (100 K $< T <$ 1000 K).

A reasonably compact interpolation between the cases of low and high T has the form

$$\frac{L}{L_0} = 1 - \frac{1 + \beta\sqrt{\alpha}}{1 + \alpha\beta + \beta\sqrt{\alpha}}. \tag{2.18}$$

We note that these results are written under several assumptions, such as *e. g.* uniform built-in field and uncorrelated localized states, which can be an oversimplifi-

cation. In real non-crystalline materials the field is generally non-uniform and grain boundaries can make the distribution of localized states correlated. Nevertheless, we hope that our model can be qualitatively adequate.

2.1.2 Generation Channels

In our model, generation channels are responsible for hopping processes that are opposite to the above considered recombination channels. They can be visualized by properly modifying Fig. 2-1(b) such that activation to the channel entrance is eliminated and all the step arrows are reversed. The latter inversion implies thermal activation at each step, the probability of which is by a factor of $\exp(-E/kT)$ lower than the downhill multi-phonon probability used in the preceding section, and can be presented as

$$\exp\left(-\frac{E}{kT^*}\right) \quad \text{with} \quad \frac{1}{kT^*} = \frac{1}{\varepsilon} + \frac{1}{kT}. \tag{2.19}$$

One other important modification to the case of recombination channels is that at each step of energy E the electron has a higher probability to decrease its energy returning back to the previously occupied state, and the relative probability of moving up is

$$\frac{\exp(-E/kT^*)}{\exp(-E/kT^*) + \exp(-E/\varepsilon)} \approx \exp(-E/kT).$$

The product of N such multipliers adds $-NE/kT = -(G - LF)/kT$ to the exponent of the generation rate. We observe that, for a channel of given length L, the generation and recombination rates are related through the Boltzmann multiplier $\exp[-(G - LF)/kT]$, exactly as required by the equilibrium condition for any recombination-generation process. The generation current in the junction due to an optimum channel of length L then becomes [cf. Eq. (2.13)]

$$I_{gen} \propto \exp\left[-\sqrt{\left(\frac{2L}{a} + \frac{G - LF}{kT^*}\right)\Lambda} - \frac{G - LF}{kT}\right], \tag{2.20}$$

where the definition of Λ is similar to that of Eq. (2.12) but with ε replaced by kT^*. The condition of current continuity exploited to determine the optimum channel length L for the recombination process is not required here since the activation current of Eq. (2.14) does not apply to the generation process.

For relatively high temperatures of practical interest, such that

$$\frac{2kT^*}{Fa} = \frac{2kT^*}{W_0}\frac{L_0}{a} > 1, \tag{2.21}$$

the generation current of Eq.(2.20) is a maximum when $L = 0$ [the latter inequality and its corresponding regimes should not be confused with the inequalities and regimes described in Eqs. (2.16) and (2.17)]. Consequently, the generation rate is proportional to $\exp(-G/kT)$ (similar to the classical case) and does not depend on W_0 or applied bias, thus the generation current is not enhanced in the junction, i.e. it is the same inside and outside of the junction. Qualitatively, we observe that recombination in the junction is enhanced because hopping transport provides a means for lowering the activation energy E_A; the generation current is not afforded the same opportunity. Hence, according to our model, a unique feature of non-crystalline semiconductors is that the recombination rate can exceed that of generation in the junction region.

For the case of medium to large reverse bias ($|qV| > G - W_0$, where q is the electron charge and V is the external bias), charge carriers can move directly from the valence to the conduction band with minimal cost in energy, as illustrated in Fig. 2-4. Therefore, optimal channel hopping is primarily through real space and the length of the optimal channel depends on the applied bias according to $L(U) = GL_0/U$ (see Fig. 2-4), which assumes a uniform electric field.

This type of non-ohmic transport was introduced in Ref. [31], which can be understood in terms of our approach by noting that the optimum reverse current has the same exponential dependence as Eq. (2.2) with $L \to L(U)$. Therefore, the

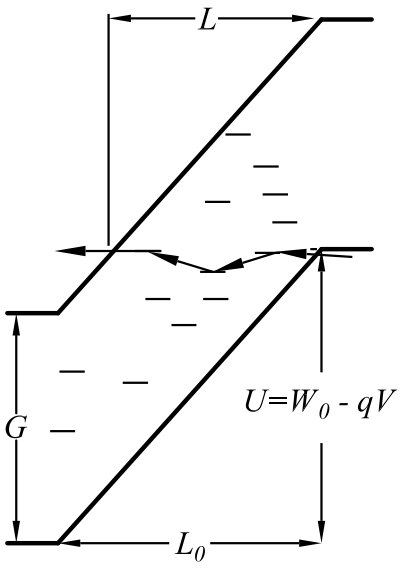

Figure 2-4: Linear p-n junction under reverse bias. Optimal channel hopping occurs through a distance $L = GL_0/U$ with minimal hopping in energy space. G is the mobility gap energy, L_0 is the depletion width, and U is the applied bias qV relative to the built-in potential W_0.

optimum current under reverse bias follows,

$$I_{rev} \propto \exp\left(-2\sqrt{\frac{2GL_0\Lambda_E}{aU}}\right) \tag{2.22}$$

where $\Lambda_E = \ln(\Lambda_E U^2/2\pi gakTG^2L_0^2)$. Note that in the expression for Λ_E, the phonon related term ε in Eq. (2.12) has been replaced by kT to allow for thermal activation between localized states. Eq. (2.22) indicates that, rather than saturating under reverse bias, the current continues to increase in absolute value due to optimal channel conduction.

2.2 Current-Voltage Characteristics of Noncrystalline p-n Junctions

To derive the IV characteristics for a small to medium forward bias [retaining the qualitative form of Fig. 2-2(b)], we replace $W_0 \rightarrow W_0 - qV = U$ in Eqs. (2.13) - (2.18). In what follows, it is understood that, according to the standard electrostatics of p-n junctions [27], the barrier parameters L_0 and W_0 depend on external bias V, i. e. $W_0 \rightarrow W_0 - qV$ and, in the approximation of uniform doping, $L_0 \propto \sqrt{W_0 - qV}$.

Normalizing I_{opt} to the area of influence per optimum channel $S_{opt} = \rho_0^2 \exp(N_0\Lambda)$ yields the forward current density which takes the form of the first term in Eq. (2.5) with

$$\frac{1}{A} = 1 - \frac{L}{L_0} \quad \text{and} \quad J_0 = J_{00} \exp\left(-\frac{W_0}{AkT}\right), \tag{2.23}$$

where L/L_0 is approximated by Eq. (2.18) and

$$J_{00} = \frac{q\,(n\sigma v)^2}{La\nu_0} \exp\,(3N_0). \tag{2.24}$$

We note that Eq. (2.23) does not depend on the assumption of our model that the density of localized states is energy independent, which is, however, essential for Eq. (2.24). While Eq. (2.23) reflects the approximation of uniform built-in field, it can be readily modified for other field distributions.

The above forward (recombination) current needs to be combined with the reverse (generation) and photocurrent components to describe the current-voltage characteristics. Here, we limit ourselves to the practically important case of high temperatures [Eq. (2.21)], in which the generation current is voltage independent and is the same as in the bulk, outside the junction.

Care should be taken when adding the generation and recombination currents, whose rates are different due to recombination enhancement in the junction region

[cf. the discussion after Eq. (2.21)]. The result can be presented in the form

$$J = J_0 \left[\exp\left(\frac{qV}{AkT} \right) - 1 \right] - (J_L - \Delta J_0), \tag{2.25}$$

where $\Delta J_0 \equiv J_{gen} - J_0 > 0$ is the difference between the generation current density J_{gen} and that of optimum channels in the dark. The condition of equilibrium in the dark ($J_L = 0, J = 0$) then leads to the contradictory conclusion of the junction being under reverse bias $V_{eq} = -(AkT/q)\ln(J_0/J_{gen})$, implying that the equilibrium Fermi level varies across the structure.

In the standard spatially homogeneous generation-recombination models, a constant Fermi energy is ensured by the condition $J_{rec} = J_{gen}$ which is always maintained by properly establishing the equilibrium carrier concentration n. However, equalizing $J_{rec} = J_{gen}$ by changing n would not apply here because n is fixed by the bulk of the material outside the junction. Since W_0 and G are fixed as well, we conclude that L_0 remains the only parameter that can self-consistently change to ensure that E_F does not vary across the structure. Physically, the required change can be due to spatially redistributed charge carriers, including change in occupations of the localized states in the mobility gap, creating a macroscopic polarization. In what follows we simply set $\Delta J_0 = 0$ assuming that L_0 already includes the effects of charge carrier redistribution. While this can violate the standard relation $L_0 \propto \sqrt{W_0 - qV}$, we note that the above redistribution effect is expected to be rather insignificant due to the very strong inequality $J_L \gg J_0$ for any reasonable light intensity (down to millionths of one sun) in all the known structures.

Combining Eqs. (2.18) and (2.23) predicts that in the low temperature regime ($\alpha \gg 1$) the ideality factor is given by

$$A = 1 + \frac{U}{kT}\sqrt{\frac{a}{2L_0\Lambda}}, \tag{2.26}$$

and for higher temperatures ($\alpha \ll 1$) it is given by

$$A = 1 + \frac{2a}{L_0 \Lambda} \left\{ \left[\frac{U}{2kT} + \ln\left(\frac{\nu_0}{n\sigma v}\right) \right]^2 - \frac{G\Lambda}{\varepsilon} \right\}. \tag{2.27}$$

The inequality $A \geq 1$ is ensured by the criterion $L > 0$, which follows from Eq. (2.17) and its related discussion. In both cases, $A \geq 1$ can be much greater than one.

The open-circuit voltage ($J = 0$) is expressed as

$$V_{oc} = \frac{W_0}{q} - \frac{AkT}{q} \ln\left(\frac{J_{00}}{J_L}\right). \tag{2.28}$$

Simply stated, the V_{oc} loss described by the second term in Eq. (2.28) is due to the shunting action of the optimum recombination channels. Note the prediction of temperature independent V_{oc} in the low-T region of Eq. (2.26).

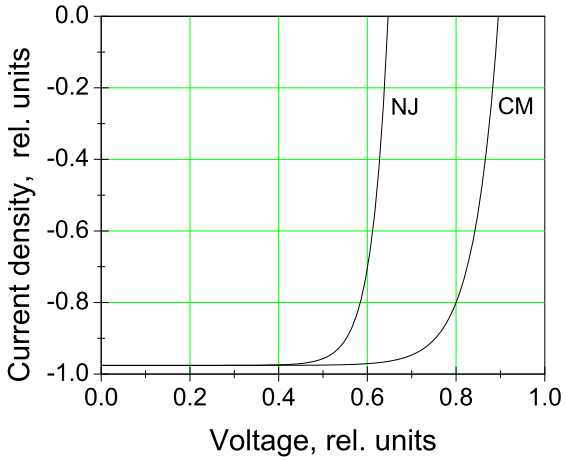

Figure 2-5: Comparative sketches of the IV curves for the non-crystalline junction (NJ) model presented here and the classical model (CM). Similar parameters were used for both models with an ideality factor of $A = 1$ for the classical model while A was given the bias dependence of Eq. (2.23) for the NJ model.

Practically, it may be difficult to determine whether the present model or the classical model prevails based solely on the shape of measured IV curves, as illustrated

in Fig. 2-5. We note that the present model yields a more square IV curve with relatively better fill factor and lower V_{oc} compared to that of the classical model with the same built-in voltage [the gain in squareness is immediately seen from Eq. (2.23) predicting large A at $V = 0$ and $A \approx 1$ at $V = V_{oc}$, since the junction is suppressed and $L = 0$ in the latter case].

To compare the effectiveness of the hopping current to that of the classical model, we take the pre-exponential of the latter in the form of $J_0 \sim qDn/L_D \exp(-W_0/kT) \equiv J_{00} \exp(-W_0/kT)$, where D is the diffusion coefficient and L_D is the diffusion length of the charge carriers [27]. While D and L_D vary between different non-crystalline materials, we assume somewhat intermediate values $D \sim 0.01$ cm^2/s (corresponding to the mobility ~ 1 cm^2 V^{-1} s^{-1}) and $L_D \sim 1$ μm. Taking also $n \sim 10^{15}$ cm^{-3}, $\sigma \sim 10^{-15}$ cm^2, $v \sim 10^7$ cm/s, $L \sim 1000$ nm, $a \sim 1$ nm, and $N_0 \sim 10$, leads to the conclusion that the pre-exponentials J_{00} in the classical and present models are comparable to within the accuracy of our very rough estimates. However, the exponential in the expression for J_0 of the present model is much higher than that of the classical model due to the ideality factor $A > 1$; hence, in non-crystalline junctions, hopping transport turns out to be more efficient than classical model transport.

The consideration in this section has been limited to forward or moderate reverse bias. For a strong reverse bias, corresponding to the diagram in Fig. 2-4, the IV characteristic will follow Eq. (2.22), exponentially deviating down from the classical prediction of $J = -J_L$. Reverse characteristics of this type have been observed many times but rarely documented since they appear in what is considered a practically unimportant region of the IV curve (see, however, Ref. [32]).

A comment is in order regarding the condition of equilibrium in a stand alone system under consideration. It may seem that such a system will violate the second law of thermodynamics by liberating Joule heat due to lateral currents flowing between the regions of generation and recombination. We believe that the second law

is maintained through negative feedback which prevents lateral currents by creating charge/temperature distributions. However, there is no fundamental restriction (similar to the second law of thermodynamics) on the lateral currents when the system is far from equilibrium. At this time we do not have a quantitative theory of such lateral currents but we note that many effects of the corresponding lateral nonuniformities can be described in the framework of the weak diode model [33]. In the context of that model, the vicinity of an optimum recombination channel can be represented as a local, low-V_{oc} micro-diode.

Related to lateral nonuniformity is the distinction between large and small area devices. We have tacitly implied in the above that the device area is large enough to contain the rare optimum channels. This is only possible when it is larger than some critical area S_c such that one optimum channel can be found with certainty. We define the density (per unit area) of optimum channels as p_N/ρ_0^2, where $\rho_0^2 = La$ is the area of an optimum channel. Thus, we determine the critical area from $S_c p_N/\rho^2 = 1$ yielding,

$$S_c = La \exp(N_0 \Lambda). \tag{2.29}$$

For large area devices ($S_d \gg S_c$), optimum channels are always available and the current will increase in direct proportion to the area, resulting in a self-averaging, constant current density. When the device area is small ($S_d \ll S_c$) the current density will be determined by the most efficient of the existing recombination channels. In that case, the current density should be a strong function of area and will vary between nominally identical devices of the same size due to the statistical dispersion of channel properties. Such variations will also lead to differences in V_{oc}, A, and J_0 between samples prepared under the same conditions.

Finally, we note that the above theory equally describes hopping transport and its related IV characteristics in Schottky junctions, including the cases of both forward and reverse currents.

2.3 Implications and Experimental Verification: Thin Film Photovoltaics

The set of experimental data used in this section was composed of several thousand IV curve readings for a variety of CdTe based photovoltaic cells prepared with different recipes as described in our previous work [34, 35, 36, 37, 38, 39, 40, 41, 42].

In comparing our above theory with the data, it should be understood that non-crystalline photovoltaics are typically comprised of several junctions, one of which creates a domain of the built-in field responsible for photovoltage, while others result from various material interfaces. Because of several barriers in the system, the resulting IV characteristics are some combination of those discussed above. In this section we consider an example of CdS/CdTe or CdS/CIGS devices. Shown in Fig. 2-6 is a possible band diagram representing these devices; the presence of a front (CdS related) barrier [34, 35, 43, 44] remains a relatively new and not commonly accepted feature, but we keep it here as an important conceptual example. The effect of a back metal contact forming a Schottky barrier (back barrier) can be rather significant in CdTe based devices [45].

When the entire device and its main junction is under forward bias, the back and front barriers operate as though they were under a corresponding reverse bias. As illustrated in Fig. 2-7, the difference between the latter two barriers is that the front one has a fixed width L_0 equal to the CdS thickness, while the back barrier thickness $L_0 \propto \sqrt{W_0}$ increases with its height W_0 and, hence, with the reverse bias. That dichotomy in barrier behavior results in the qualitatively different IV curves illustrated in Fig. 2-8. The back barrier contributes a rollover saturation at high voltages (curve 2 in Fig 2-8), which reflects the fact that increasing the voltage across it increases both the barrier width L_0 and the hopping distance L. Contrarily, under reverse bias, the front barrier maintains its base width L_0 while the hopping distance

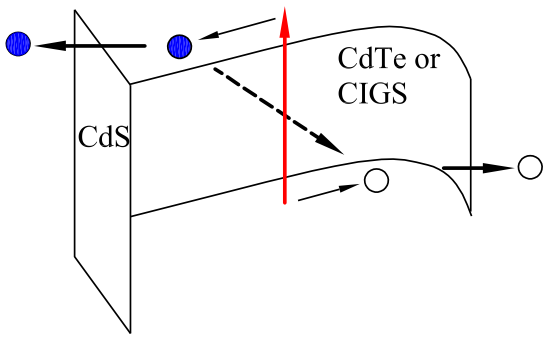

Figure 2-6: Possible band diagram of CdTe or CuIn(Ga)Se_2 (CIGS) based photovoltaics showing front (CdS) barrier, main junction, and back barrier. Horizontal arrows represent hopping through the back and front barriers, vertical arrow depict photoexcitation of electrons-hole pairs (filled and empty circles), dashed arrow shows recombination through a channel in the main junction of the type presented in Fig. 2-2 (b).

L decreases. Therefore, under high enough bias, hopping conduction through the front barrier increases, resulting in rollover recovery (curve 3 in Fig 2-8).

In comparing the latter predictions with the data, we note that, generally, either the back or front barrier will determine the form of the rollover; comparable contributions from both of them would be a shear coincidence. Therefore, one can expect either rollover with saturation or recovery depending on the device recipe. For example, our data in Fig. 2-9 show these two types of rollover in cells of different recipes. The significant variations of the back barrier effect between nominally identical cells shown in Fig. 2-9 (a) can be understood based on the concept of hopping transport in small area cells, as explained in the discussion following Eq. (2.29).

We now turn to verifications concerning the ideality factor. The following values of A have been extracted from the data based on the standard routine in which A is voltage independent, contrary to the predictions in Eq. (2.23); therefore we can, at best, count on qualitative agreement between the data and our theory.

It follows from Eq. (2.23) that A is expected to increase under light compared to

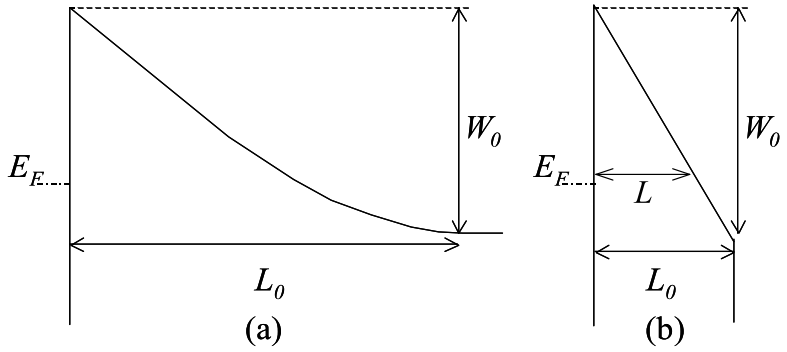

Figure 2-7: Diagrams of possible (a) back and (b) front barriers under reverse bias (relative to those barriers) in thin-film photovoltaic devices of the type shown in Fig. 2-6. The Fermi level (E_F) moves up with reverse bias while its distance from the top of the barrier remains fixed. (a) represents the standard Schottky barrier whose width L_0 and slope increase with reverse bias and barrier height W_0. (b) is a fixed thickness barrier whose effective width L for hopping *decreases* with W_0 and reverse bias.

the 'dark' condition due to shrinking of the depletion width L_0 related to the light induced increase in screening carrier concentration. The dependence of A on illumination is verified in Fig. 2-10 where it is evident that the average A over a large number of samples increases under light conditions. The difference between (a) and (b) shows that larger values of A are associated with lower device efficiencies. Furthermore, since our theory associates larger values of A with a higher recombination rates, we expect devices to deteriorate more quickly under light.

The connection between large A and poor device performance is also implied by Eq. (2.28) which predicts a negative correlation between V_{oc} and A. The latter should be treated as a statistical trend given the many other factors affecting V_{oc} in real devices. That trend is verified by the data presented in Fig. 2-11.

Similarly, we have verified the statistical correlation between J_0 and A, which according to Eq. (2.23) should have the form $\ln J_0 = \ln J_{00} - W_0/AkT$ shown with the solid line in Fig. 2-12. Again, there is a clear qualitative agreement between the data and the theory.

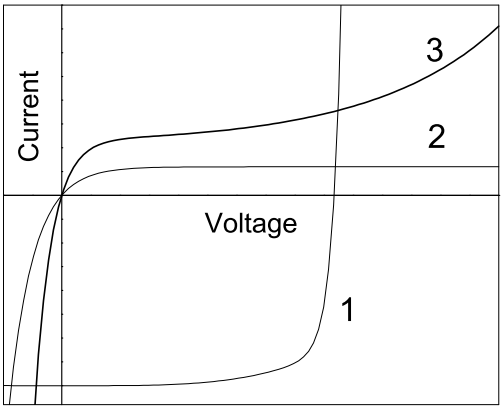

Figure 2-8: Partial IV curves corresponding to the device components: 1) main junction; 2) back barrier; and 3) front barrier. While curves 2 and 3 describe the reverse bias condition, they are represented under the transformations $V \rightarrow -V$ and $I \rightarrow -I$ to fit the definition of forward and reverse bias for the entire device. Their addition obeys the series connection rule (voltages add at any given current) and results in the rollover shaped characteristics.

Another conceivable test of our model (not yet conducted) is the prediction of $A \propto 1/T$ in Eq. (2.26) and thus temperature independent V_{oc} in the low T regime, according to Eq. (2.28).

We shall end this section with a comment that can be of practical significance. While the phenomenological approach where A is kept as a fitting parameter of the otherwise classical model can give a satisfactory IV curve fit of the above considered mechanism, the strategy of junction improvement will significantly depend on which model is accepted. The model presented here suggests that V_{oc} loss can be mitigated by suppressing the recombination channels, while the classical model would advocate suppressing recombination related to defects, which depends on material chemistry and morphology. A significant difference between these approaches is that the channels can be suppressed by blocking their entrances without affecting other material properties. Channel blocking can be achieved through various surface treatments, in

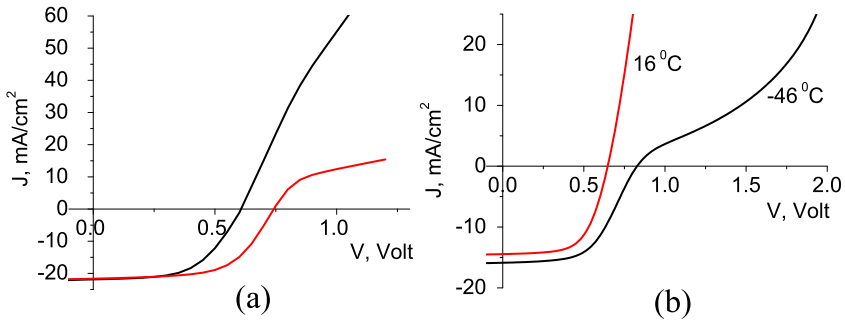

Figure 2-9: (a) IV curves of two nominally identical CdTe based cells on the same substrate at room temperature showing different degrees of rollover which do not recover. (b) IV curves of one CdTe cell of a different recipe than (a) measured at two different temperatures (shown at the curves) exhibiting the rollover recovery.

particular, by introducing interfacial layers as was previously emphasized on empirical grounds [46].

2.4 Conclusions

Optimal channel hopping can be the primary electronic transport mechanism in non-crystalline thin films at typical operating temperatures. On that basis, we have developed a theory of electronic transport in non-crystalline junctions that correlates current-voltage characteristics to material parameters. Compared to classical models, we convey a qualitatively different picture wherein current flow is laterally nonuniform and concentrated in the region of optimum channels.

While the theory is quite general, we have applied it to the technologically important case of thin-film photovoltaics (PV). Our theory provides a physical origin of the diode ideality factor, which can be greater than two under typical operating conditions. In addition, an explanation of the observed variations in nominally identical devices is given in terms of the statistical nature of the optimal channels. Some of

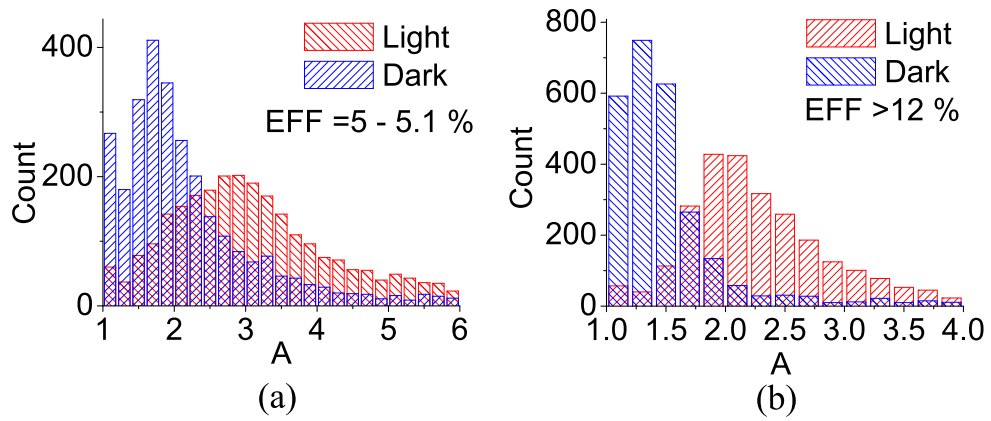

Figure 2-10: Ideality factor under 'dark' and 'light' (1 sun) conditions for two databases (of about 2500 samples each) representing CdTe/CdS solar cells with efficiencies (a) in the interval 5-5.1 %, and (b) greater than 12 %.

our more specific predictions are listed below.

1) Depending on material parameters, such as the density of localized states and depletion width, the ideality factor A can be in the range from almost unity to much greater than two at typical operating temperatures. In addition, A has two distinct temperature regimes.

2) A generally depends on both T and applied bias V; it is large near $V = 0$ and close to unity at $V = V_{oc}$.

3) A depends on illumination intensity and increases under light.

4) There is a negative correlation between A and V_{oc}.

5) At low temperatures, A is inversely proportional to temperature, which results in temperature independent V_{oc}.

6) The saturation current J_0 increases exponentially with A.

7) Optimum channel transport can dominate the operation of not only photovoltaic junctions, but also back and front barriers, the effects of which appear in the IV curve rollovers at large forward bias. Our consideration predicts that the rollover can either saturate or recover with forward bias depending on the contact barriers for a

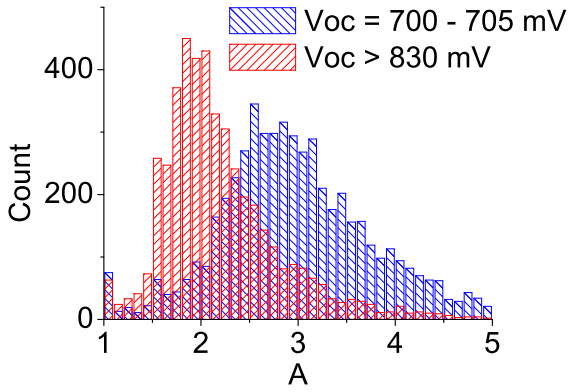

Figure 2-11: Statistical distributions of ideality factors for two databases (of about 5000 samples each) representing CdTe/CdS solar cells with $V_{oc} > 830$ mV and in the interval of $700 - 705$ mV. There is a negative correlation between V_{oc} and A as predicted by Eq. (2.28).

particular device.

The predictions of our theory are in qualitative agreement with the available experimental data, some still require experimental verification, including the voltage dependent ideality factor and temperature independent V_{oc} in the low T regime.

While our theory does not provide much advantage over the classical models in terms of fitting the operationally important fourth quadrant of the IV curve, of greater practical importance is a better understanding of the recombination mechanism which can lead to improvements in device efficiency and stability. Our theory suggests that PV performance can be improved by blocking the entrances to optimal channels, possibly using surface treatments, while other models may purport controlling defect chemistry.

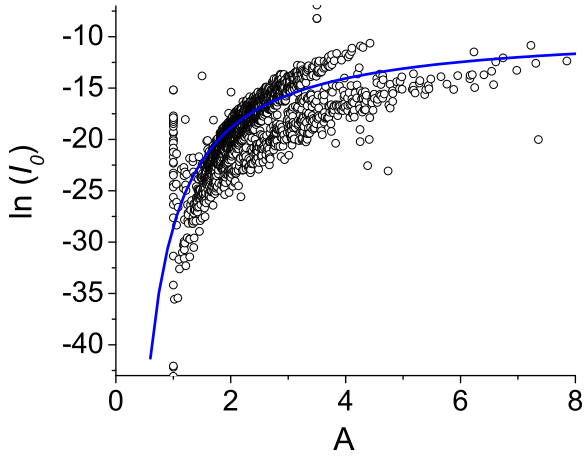

Figure 2-12: Correlation between the ideality factor A and saturation current I_0 extracted from a database of approximately 2500 CdTe based PV cells with efficiency greater than 12%. Cells of different recipes used in our experiments exhibit themselves in the form of somewhat different groups of points. Here we show the general trend fit using Eq. (2.23), although a more detailed analysis indicates that some rare cells can have I_0 independent of A, corresponding to classical junction transport rather than hopping transport.

Chapter 3

Admittance Characterization of Semiconductor Junctions

Admittance spectroscopy has long been a routine characterization technique in semiconductor science and technology [18, 47, 48]. It provides information about the space charge distribution (capacitance-voltage, C-V) and the density of states distribution (capacitance-frequency, C-F) in crystalline [48], amorphous [18, 49], and polycrystalline [20, 50, 51, 19] semiconductor materials and devices.

The standard understanding of admittance characterization is based on the model of a leaky flat plate capacitor. Its equivalent circuit (in Fig. 3-1) represents a tested sample leading to the admittance

$$Y \equiv \frac{J}{V} = G + i\omega C, \tag{3.1}$$

where J is the current and $V = V_0 \exp(i\omega t)$ is the testing ac voltage of frequency ω. The real and imaginary parts of the admittance provide the equivalent conductance G and the capacitance C, as shown in Fig. 3-1. To maintain the conditions of linear response, the testing voltage amplitude is typically very small, $V_0 \ll kT/q$, where T is the temperature, k is the Boltzmann's constant, and q is the electron charge. The admittance measurements conducted at different frequencies (ω), biases (V),

and temperatures are interpreted assuming a model where all the physical quantities (such as defect states, doping profiles, etc...) vary along one spatial coordinate perpendicular to the system electrodes.

The latter assumption implies that the electrodes are equipotentials, so that there is no lateral current in the system. However, many practically important device structures have sufficiently resistive electrodes that are not equipotentials and exhibit significant currents in the lateral directions. For example, many photovoltaic structures utilize transparent conductive oxides (TCO) of a finite sheet resistance ρ ($\sim 10\ \Omega/\square$). Another important example is a Schottky barrier structure with a metal electrode on one side and a semiconductor on the opposite side with very high sheet resistance (say, $\sim 10^9 - 10^{12}\ \Omega/\square$ measured in Ref. [52]).

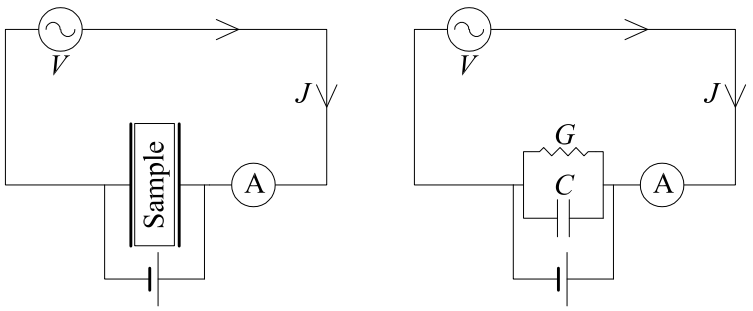

Figure 3-1: Sketch of the experimental setup for admittance measurements (left) and the equivalent circuit (right).

Here we present a theory of admittance characterization for systems with resistive electrodes allowing for significant lateral currents. More specifically, we consider a distributed system exhibiting leaky photo-diode and capacitive properties, whose discrete equivalent circuit is shown in Fig. 3-2. The fundamental element of the system includes the following components in parallel with each other: 1) a photo-diode characteristic of the semiconductor material; 2) a capacitance related to the

material response to an ac voltage; and 3) a shunt resistance. The elements are connected via two electrodes, one of which is of finite resistance and the other a metal. This model and the following theoretical development make no references to specific material combinations. Also, we consider both one-dimensional (1D) and two-dimensional (2D) systems.

A similar but simpler model, without distributed capacitance and shunt resistance, was analyzed earlier [53] to describe dc operations of photovoltaics. The previous work introduced a characteristic decay length of a small electric perturbation in the lateral direction,

$$L_0 = \sqrt{\frac{kT}{qj_o\rho}}, \tag{3.2}$$

where j_0 is the photo-diode saturation current density (Fig. 3-3). It was shown that the decay length delineates the region in which current is collected (the active area) and, therefore, influences the I/V characteristics of the device. Moreover, the previous results indicated that the decay length concept could be applied to determine the characteristic area affected by a shunt, thereby providing a means of diagnosing device nonuniformities.

In the present work, the concept of decay length is extended to include systems with distributed shunt resistance and capacitance that are subject to small ac test voltages. Simultaneously, various regimes of applied dc voltage are considered. The addition of shunt resistance and capacitance results in two new characteristic lengths, L_R and L_C, that describe the decay of an ac perturbation in the system and determine the frequency dependent admittance. It will be shown that an understanding of these decay lengths plays a vital role in effective device characterization.

This chapter is organized as follows. In Sec. 3.1 we present a qualitative analysis of the problem allowing for simple semi-quantitative results including the concepts of large and small systems. Sec. 3.2 and 3.3 introduce a rigorous approach for respectively the one-dimensional and two-dimensional systems. Practical implications

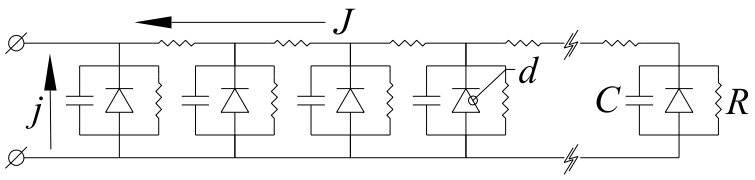

Figure 3-2: Equivalent circuit of a device with a resistive electrode in the lateral direction and distributed diode, capacitance, and shunt resistance in the transverse direction.

of our results are discussed in Sec. 3.4 and Sec. 3.5 contains concluding remarks.

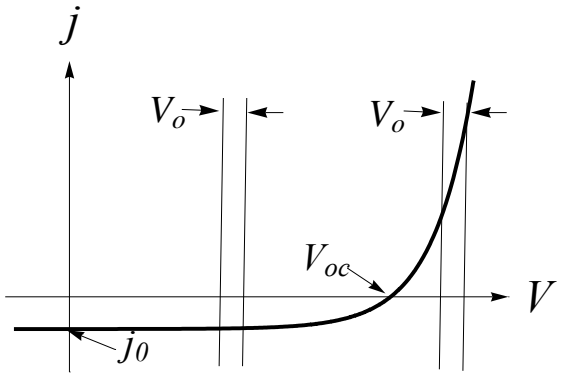

Figure 3-3: Sketch of the diode current-voltage characteristics with major parameters used in this chapter. The domains of the ac testing voltage, V_0, are shown for the cases of significant forward ($V \gg V_{oc} + kT/q$) and reverse ($V \ll V_{oc} + kT/q$) biases.

3.1 Qualitative Analysis

A small electric perturbation δV at the input of the circuit in Fig. 3-2 will decay in the lateral direction over the characteristic length L determined by the electrode resistance and current leakage through the transverse resistors, diodes, and capacitors. The decay length, L, together with the linear dimension, l, of the electrode will

determine the active region of the system. Depending on the device structure and the relationship between L and l, the size of the active region can be close to either L or l, as discussed below.

A complete description of the decay length approach requires that we clearly define all conceivable scenarios. First of all we note the obvious division into the regimes of geometrically large ($l \gg L$) and small ($l \ll L$) cells, each of which can be either 1D or 2D systems. In addition, one has to discriminate between two types of electrode configurations, namely, substrate (*e.g.* CuIn(Ga)Se or a-Si:H) and superstrate (*e.g.* CdTe) devices. Therefore, there are a total eight conceivable, nominally different scenarios (*i.e.* all combinations of small and large cells, 1D and 2D, and substrate vs. superstrate). The four 1D scenarios are presented in Fig. 3-4. Fortunately, many of these scenarios are not completely distinct. For example, the 1D and 2D cases are only quantitatively different. Furthermore, it will be shown that a large substrate cell behaves similar to a small superstrate cell and a large superstrate cell is similar to a small substrate cell.

If the decay length, L, is given, then a phenomenological description of the four possible scenarios shown in Fig. 3-4 can be obtained by considering the various combinations of electrode configuration and cell size. The transverse current generated in the semiconductor structure is collected through the lateral electrodes, one of which is resistive (TCO) and the other is of negligibly small resistance. It should be understood that under stationary conditions transverse current generation is always limited to the region of the device where current collection is possible in the lateral direction. By definition, the lateral current in the resistive electrode decays over the length L, as indicated in Fig. 3-4(a). Similarly, the active region of the device in Fig. 3-4(b) is $L + l \approx l$. Due to the same limitation, the current can only be collected from the region of length $L \ll l$ in Fig. 3-4(c). Finally, in the case of Fig. 3-4(d), although the decay length is larger than the cell size, current collection is limited to the small

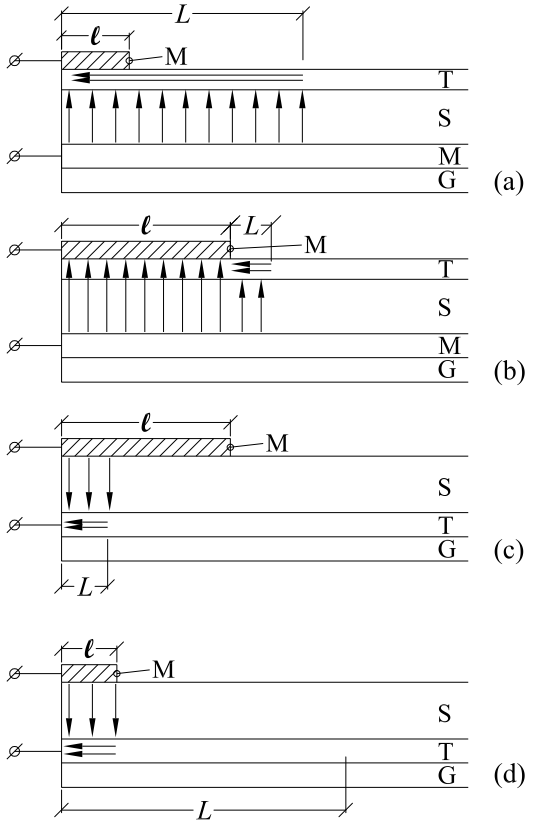

Figure 3-4: Examples of four possible 1D device scenarios: (a) small, substrate; (b) large, substrate; (c) large, superstrate; and (d) small, superstrate. The device components are labeled as M, T, S, and G for metal, TCO, semiconductor, and glass, respectively. The arrows represent the active regions of current collection defined by the decay length L in each case relative to the cell size l.

electrode size $l \ll L$.

Referring to Fig.3-4, we observe that the cases of (b) and (d) are trivial, corresponding to the geometrical interpretation of Fig. 3-1, where the contact area fully determines the admittance. The concept of decay length becomes important in cases (a) and (c) where L dictates the collection length (the active area). Also, switching from the 1D to the 2D case does not cause any significant changes: for cases (b) and (d) the electrode area rather than its length determines the impedance; for case (a) the active area is $\sim L^2$; finally, the active area is $\sim lL$ for case (c).

With the pertinent physical scenarios defined, we can now determine the appropriate forms of the measured capacitance and conductance for each case. Setting aside the trivial cases (b) and (d), we start with the large superstrate system regime $l \gg L$. For the 1D systems, the measured capacitance and conductance can be estimated as

$$C = cL \quad \text{and} \quad G = gL. \tag{3.3}$$

Here c and g are the capacitance and conductance per length; these quantities can be frequency dependent reflecting the material parameters behind our circuitry. For the 2D case, the corresponding definitions will depend on the electrode configuration. To maintain similarity and connection between the 1D and 2D cases of a large superstrate cell, we assume a circular electrode of radius $a \gg L$ for the 2D case, as shown in Fig. 3-5. Taking into account that current collection will be determined by a narrow area $2\pi aL$, the measured capacitance and conductance will be given by

$$C = 2\pi acL \quad \text{and} \quad G = 2\pi agL, \tag{3.4}$$

where c and g are the capacitance and conductance per unit area in the 2D system.

A small 1D substrate cell [Fig. 3-4(a)] is similar to a large superstrate cell [Fig. 3-4(c)] with the measured capacitance and conductance given by Eq. (3.3); while its 2D counterpart uses the entire area of a circle πL^2 (assuming a small contact far from the structure edge) instead of the narrow region used in Eq. (3.4). The case of a small 2D substrate cell is discussed in detail in Sec. 3.3.

The decay length can be frequency and bias dependent, $L = L(\omega, V_d)$, as specified next. Since the three partial decay lengths, L_d (diode related ac decay length), L_R, and L_C, are determined by sufficiently different physical processes, they are generally quite different. In the framework of this qualitative analysis, the effective decay length

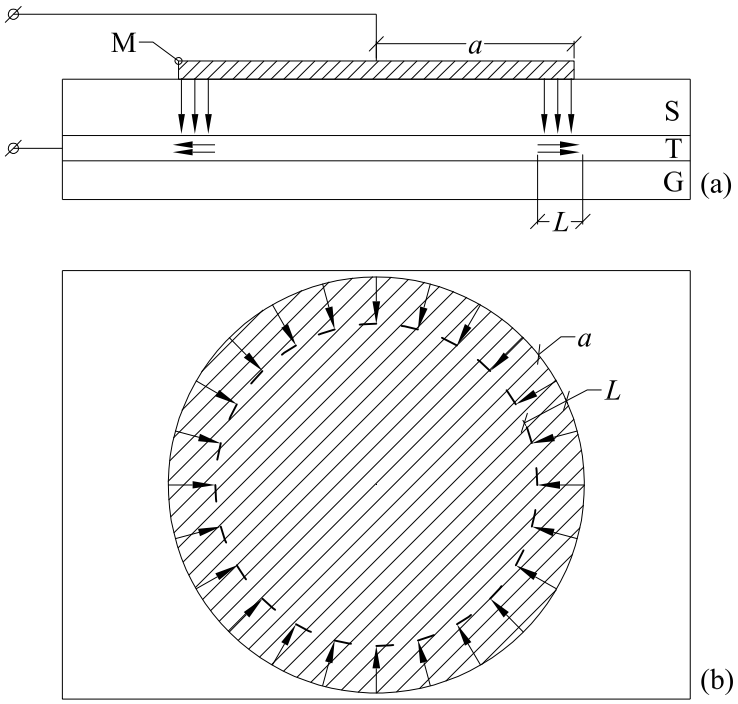

Figure 3-5: The 2D version of a large ($a \gg L$) superstrate cell with the cross-sectional view shown in (a) and the top view in (b). Current is collected in the small annular area of width L near the perimeter of the circular metal contact of radius a. The device components are labeled as in Fig. 3-4.

in Eqs. (3.3) and (3.4) will be the minimum of the three partial lengths, that is,

$$L = \min\{L_C, L_R, L_d\}. \tag{3.5}$$

To estimate the above lengths, we consider separately three simplified versions of the circuit in Fig. 3-2 with each containing just one of the three elements, shunting resistance, capacitance, or photo-diode. Because the R- and C-elements operate in the linear (Ohmic) regime, the related lengths, L_C and L_R, can be analyzed by simply calculating the distance at which the total lateral resistance equals the total transverse resistance.

For example, assuming the 1D specific shunt resistance R (in units Ω·m), the

domain of length L_R will possess the shunt resistance R/L_R, while the corresponding lateral resistance is estimated as ρL_R. Setting the latter two resistances equal determines the characteristic decay length,

$$L_R = \sqrt{\frac{R}{\rho}}, \tag{3.6}$$

which is well known from the transmission line theory (see *e. g.* Ref. [54]). Similarly, considering the specific capacitance c (in units F/m) and replacing the shunt resistance with the reactance $(\omega c L_C)^{-1}$ gives the decay length related to the capacitance,

$$L_C = \sqrt{\frac{1}{\rho c \omega}}. \tag{3.7}$$

Consider next the decay length related to the diode, L_d. We recall that the characteristic length in Eq. (3.2) can be qualitatively understood [33] based on the ideal diode current-voltage characteristics

$$j = -j_0 \left[\exp\left(\frac{q(V - V_{oc})}{kT} \right) - 1 \right], \tag{3.8}$$

where V_{oc} is the open-circuit voltage and j and j_0 are the current densities. At $V = V_{oc}$, the slope $dV/dj = R_{oc} = kT/qj_0$ defines the open-circuit specific resistance (in same units as R above). Substituting R_{oc} in place of R in Eq. (3.6) gives L_0 from Eq. (3.2). We note that, from a phenomenological standpoint, Eq. (3.8) does not necessarily imply an ideal diode, but rather any rectifying device, including non-ideal diodes, metal-insulator-semiconductor structures, heterojunctions, etc. In particular, the diode nonideality factor can be added in front of kT, or j_0 can have different meanings corresponding to different models [27].

Since the diode elements are nonlinear (non-Ohmic), the decay lengths for the reverse and forward bias regions are calculated by determining the point at which the

lateral current through the resistive electrode equals the cumulative transverse current through the diode elements. The decay length in Eq. (3.2) significantly changes for the regimes of strong reverse ($V_{oc} - V \gg kT/q$) and forward ($V - V_{oc} \gg kT/q$) bias. In the former case, the condition of diode current $j_0 L$ being equal to the Ohmic, lateral current, $(V_{oc} - V)/L\rho$, introduces the decay length of a dc reverse bias,

$$L_- = \sqrt{\frac{V_{oc} - V}{j_0 \rho}} \quad (\gg L_0). \tag{3.9}$$

For the latter case, we take into account that a significant forward bias increases the diode current by the factor of $\exp[q(V - V_{oc})/kT] \gg 1$. As a result, Eq. (3.9) transforms into

$$L_+ = \sqrt{\frac{V - V_{oc}}{j_0 \rho}} \exp\left[-\frac{q(V - V_{oc})}{2kT}\right] \quad (\ll L_0), \tag{3.10}$$

which gives the decay length of a dc forward bias.

While Eqs. (3.9) and (3.10) will prove to be useful in the more rigorous analysis presented in Sec. 3.2 and 3.3 below, one should bear in mind that these lengths delineate the region of the system which contributes to the lateral current due to a *dc* perturbation and as such are irrelevant to the case of small ac perturbation. However, an ac testing perturbation can be applied in conjunction with a significant dc bias, either reverse or forward.

Given a small amplitude ac test voltage ($\delta V \ll kT/q$), the diode elements remain in a linear resistance regime. Therefore, under reverse dc bias, the ac decay length, L_d, due to the diode elements can be derived with the same analysis employed for Eqs. (3.6) and (3.7), and by noting [cf. discussion following Eq. (3.8)] that the biased system resistance becomes greater than R_{oc} by a factor of $\exp[q(V_{oc} - V)/kT]$, which

yields

$$L_d = L_0 \exp\left[\frac{q(V - V_{oc})}{2kT}\right] \quad (\ll L_0). \tag{3.11}$$

In particular, under very strong reverse bias where the current-voltage curve is completely flat, a small perturbation does not generate any feedback current and thus does not decay.

Under forward dc bias, the characteristic ac decay length remains L_0. Indeed, since the resistance there is smaller than R_{oc} by the factor of $\exp[q(V_{oc} - V)/kT]$ and the current is by the same factor higher than j_0, these two effects completely balance each other without any effect on L_0.

So far we have been discussing the decay lengths for the 1D case. However the above results are equally applicable to the 2D case, to which all the above consideration can be extended by changing the dimensions of resistances and currents. For example, in the 2D case ρ will have the dimension of $\Omega/\Box$, R and R_{oc} units become $\Omega{\cdot}\mathrm{m}^2$, and the current densities j, j_0 will be in units of A/m^2. With these dimensional modifications in mind, it is straightforward to observe that the expressions for all of the decay lengths remain the same as in the 1D case.

We shall conclude this section by providing an specific example of the above derived qualitative results. Consider a 2D large superstrate system of perimeter $2\pi a$ whose linear dimension is large compared to the above described decay lengths and the shunt resistance is very high. If the system is subjected to a small ac bias of frequency ω, without dc bias, then the effective capacitance is given by Eqs. (3.4) and (3.5) as,

$$C = 2\pi ac \min\{L_0, L_C\} \tag{3.12}$$

For a sufficiently high frequency such that,

$$\omega \gg \omega_c \equiv \frac{1}{c\rho L_0^2}, \tag{3.13}$$

Eq. (3.12) yields,

$$C = 2\pi a\sqrt{\frac{c}{\omega\rho}}, \tag{3.14}$$

while for $\omega \ll \omega_c$, $C = c2\pi aL_0$, which is frequency independent. Since L_0 can depend on light intensity (through j_0), this example shows how the above results can be used to determine system parameters, such as sheet resistance, specific capacitance, etc. To avoid repetition, further examples will not be considered here since the corresponding closed form results are given below.

3.2 One-Dimensional Systems

In this section we develop a rigorous derivation for the admittance of a 1D system. A general formalism is introduced, then different cases of dc bias are considered separately. Here we consider the circuit of Fig. 3-2 implying that it can describe both cases (a) and (c) of Fig. 3-4. In both cases it is understood that the probe contact is at the cell edge ($x = 0$), meaning that the cell size, l, is negligibly small in the case (a).

3.2.1 General Formalism

The transverse flow of electrical current per unit length through the device is described by the equation,

$$j = -j_0\left[\exp\left(\frac{q(V - V_{oc})}{kT}\right) - 1\right] - c\frac{\partial V}{\partial t} - \frac{V}{R}, \tag{3.15}$$

where the first, second, and third terms correspond respectively to the diode, capacitor, and shunt resistance currents in parallel. For brevity, we do not explicitly include the diode ideality factor assuming that it is included in the definition of T. The electrical properties of the system are then described by Ohm's law for the lateral

current and conservation of charge law,

$$J = -\frac{1}{\rho}\frac{\partial V}{\partial x}, \quad \frac{\partial J}{\partial x} = j \tag{3.16}$$

with j from Eq. (3.15). The latter equations can be combined into a single second order, partial differential equation for the potential,

$$\frac{\partial^2 \mathrm{V}}{\partial x^2} = \rho j_0 \left[\exp \frac{q(V - V_{\mathrm{oc}})}{kT} - 1\right] + C\rho\frac{\partial V}{\partial t} + \frac{V}{R}\rho, \tag{3.17}$$

which describes the time-dependent spatial distribution of the electric potential in the resistive electrode. Introducing the dimensionless variable

$$u(x,t) = \frac{q}{kT}(V - V_{\mathrm{oc}}),$$

yields

$$\frac{\partial^2 u}{\partial x^2} = \frac{q\rho j_0}{kT}\left(e^u - 1\right) + C\rho\frac{\partial u}{\partial t} + \left(\frac{kT}{q}u + V_{\mathrm{oc}}\right)\frac{\rho}{R}. \tag{3.18}$$

In order to demonstrate the value and general practicality of the decay length concept, the remainder of this analytical development will be completed by replacing the typical parameters of Eq. (3.18) with the three partial decay lengths discussed above, which yields,

$$\frac{\partial^2 u}{\partial x^2} = \frac{1}{L_0^2}\left(e^u - 1\right) + \frac{1}{L_c^2\omega}\frac{\partial u}{\partial t} + \frac{1}{L_R^2}u + \frac{V_{\mathrm{oc}}q\rho}{RkT}. \tag{3.19}$$

To advance a solution of Eq. (3.19), the potential is separated into time-dependent and time-independent parts,

$$u(x,t) = u_1(x) + u_2(x,t)$$

with u_1 representing a dc bias and u_2 being a small ($|u_2| \ll 1$) alternating testing signal. Separating the time dependent and stationary parts and linearizing with respect to u_2 splits Eq. (3.19) into the following two equations,

$$\frac{d^2u_1}{dx^2} = \frac{1}{L_0^2}(e^{u_1}-1) + \frac{1}{L_R^2}u_1 + \frac{V_{\rm oc}q\rho}{RkT} \tag{3.20}$$

$$\frac{\partial^2 u_2}{\partial x^2} = \frac{1}{L_0^2}e^{u_1}u_2 + \frac{1}{L_c^2\omega}\frac{\partial u_2}{\partial t} + \frac{1}{L_R^2}u_2. \tag{3.21}$$

Eq. (3.20) can be integrated once to give the dc part of current-voltage characteristics,

$$\frac{du_1}{dx} = \sqrt{2}\sqrt{\frac{1}{L_0^2}e^{u_1} + \frac{1}{2L_R^2}u_1^2 + (\frac{V_{\rm oc}}{Rj_0}-1)\frac{u_1}{L_0^2}}. \tag{3.22}$$

Eq. (3.21), however, is handled by separation of variables, $u_2(x,t) = \theta(t)X(x)$, which provides two more equations,

$$\frac{d^2X}{dx^2} = \left[\frac{1}{L_0^2}(e^{u_1}-1) + \frac{1}{L_R^2} + \frac{1}{L_0^2} + \lambda\right]X \tag{3.23}$$

$$\frac{d\theta}{dt} = \lambda L_C^2\omega\theta \tag{3.24}$$

where λ is an unknown constant. Substituting the temporal variation law, $\theta \propto \exp i\omega t$, into Eq. (3.24) yields

$$\lambda = \frac{i}{L_C^2}.$$

As a result, spacial variation of the electric potential is described by the equation,

$$\frac{d^2X}{dx^2} - \left[\frac{1}{L_0^2}(e^{u_1}-1) + \frac{1}{L_R^2} + \frac{1}{L_0^2} + \frac{i}{L_C^2}\right]X = 0. \tag{3.25}$$

The latter result suffices to calculate the admittance measured at the system terminals, $x = 0$,

$$Y = \frac{J}{V} = -\frac{1}{\rho}\frac{1}{X}\frac{dX}{dx} \quad \text{at} \quad x = 0. \tag{3.26}$$

Next, we consider the three different cases of dc bias, namely, zero dc bias, forward dc bias, and reverse dc bias.

3.2.2 Zero dc Bias

In this case $u_1(x) = 0$, and Eq. (3.25) becomes

$$\frac{d^2X}{dx^2} - \left[\frac{1}{L_R^2} + \frac{1}{L_0^2} + \frac{i}{L_C^2}\right] X = 0, \tag{3.27}$$

leading to,

$$Y = \frac{1}{\rho}\sqrt{\frac{1}{L_0^2} + \frac{1}{L_R^2} + \frac{i}{L_C^2}}. \tag{3.28}$$

The measured capacitance and conductance are,

$$C = cL_C\frac{L_C}{L}\sin\left(\frac{\psi}{2}\right), \quad G = \frac{L_R}{R}\frac{L_R}{L}\cos\left(\frac{\psi}{2}\right) \tag{3.29}$$

where,

$$\frac{1}{L} = \left[\left(\frac{1}{L_0^2} + \frac{1}{L_R^2}\right)^2 + \frac{1}{L_C^4}\right]^{\frac{1}{4}}, \tag{3.30}$$

$$\psi = \arctan\left[\frac{L_0^2 L_R^2}{L_C^2\left(L_0^2 + L_R^2\right)}\right]. \tag{3.31}$$

We note that both L and ψ are frequency dependent due to the frequency dependent decay length L_C defined in Eq. (3.7).

3.2.3 Reverse dc Bias

Even though the dc bias (u_1) is negative in this case, the term with e^{u_1} in Eq. (3.25) cannot be neglected in general, since L_0 can be smaller than the other decay lengths. A more 'tactful' approach is based on an approximation similar to the

standard "semi-classical" approximation in quantum mechanics. Note that in this connection Eq. (3.25) is formally similar to the Schrödinger equation with the first term in square brackets playing the role of potential energy. The approximation is motivated by the fact that, according to Eq. (3.9), the dc decay length, L_-, is relatively large, meaning that the electric potential varies slowly over the region of the system affected by the dc bias. In the context of the semi-classical approach, this is similar to a rapidly varying wave function subject to a slowly varying potential. In the spirit of the semi-classical approach, we attempt a trial solution,

$$X(x) = \exp[S(x)], \quad Y = -\frac{1}{\rho}\frac{dS}{dx}\Big|_{x=0}$$

where the second relation follows from Eq. (3.26). Substituting the trial solution into Eq. (3.25) and neglecting the $|d^2S/dx^2|$ term compared to the $(dS/dx)^2$ term, a solution for dS/dx is immediately obtained. The validity of the solution can be verified with respect to the assumed semi-classical condition.

As a result, one obtains,

$$Y = \frac{1}{\rho}\sqrt{\frac{\exp[u_1(0)]}{L_0^2} + \frac{1}{L_R^2} + \frac{i}{L_C^2}}, \tag{3.32}$$

where $u_1(0)$ is related to the the applied dc bias by

$$u_1(0) = \frac{q\,(V_{dc} - V_{oc})}{kT} \quad (< 0).$$

We observe that the only difference between this and the previous case of Eq. (3.28) for zero dc bias is that L_0 is replaced with $L_0 \exp[-u_1(0)/2]$, which is fully consistent with the previous qualitative understanding in Eq. (3.11). It is then straightforward to see that the expressions for the capacitance and conductance in the reverse dc bias case are given by Eqs. (3.29) with $L_0 \to L_0 \exp[-u_1(0)/2]$.

3.2.4 Forward dc Bias

For the forward bias case, the exponential term in Eq. (3.25) is dominant, however, it is only effective over a very short range of length L_+, defined in Eq. (3.10). In the terms of the quantum mechanics analogy discussed in the previous section, this is similar to the 'ultra-quantum' condition (the reverse of 'semi-classical' condition), corresponding to a narrow, deep potential well. The adequate mathematical technique for this kind of problem is well known (see e.g. Ref. [55]). Due to the short range nature of the exponential term, the value of $X(x)$ is expected to remain almost constant in the region from $x = 0$ to $x = x_0$, where x_0 is just slightly greater than L_+. The validity of this assumption can be tested by the condition,

$$\delta X = \frac{dX}{dx} L_+ \ll X(0). \tag{3.33}$$

Since $X(x)$ remains nearly constant for $0 \leq x \leq x_0$, the forward bias case is solved by considering the following two regions for the potential: 1) $x < x_0$; and 2) $x > x_0$. In the first region, Eqn. (3.25) can be integrated once from $x = 0$ to $x = x_0$ to give,

$$\frac{1}{X(0)} \left(\frac{dX}{dx}\Big|_{x=x_0} - \frac{dX}{dx}\Big|_{x=0} \right) = \int_0^{x_0} \left[\frac{1}{L_0^2}(e^{u_1} - 1) + \frac{1}{L^2} e^{i\psi} \right] dx. \tag{3.34}$$

In the second region, just beyond L_+, the dc bias is almost completely diminished and the solution to Eq. (3.25) is simply,

$$X(x) = X(0) \exp\left(-x \sqrt{\frac{1}{L_0^2} + \frac{1}{L_R^2} + \frac{i}{L_C^2}} \right). \tag{3.35}$$

The connection between the two regions is obtained by taking the first derivative of Eq. (3.35) evaluated at $x = x_0$ and substituting this into Eq. (3.34). Finally, using

the explicit form of the potential [53],

$$u_1(x) = \frac{q(V - V_{oc})}{kT} + 2\ln\left(1 - x/L_+\right), \tag{3.36}$$

in the region $0 \leq x \leq L_+$, the integral on the right-hand-side of Eq. (3.34) is readily evaluated. The second term in the integrand contributes terms of the order $L_+/L_0 \ll 1$, which are considered small as defined by the 'ultra-quantum' condition of Eq. (3.33) and are therefore neglected. However the first term gives a generally large, real contribution $(3L_0)^{-1}\exp[q(V - V_{oc})/2kT]$ with a corresponding term in the admittance,

$$G_+ = \frac{1}{3\rho L_0}\exp\left[\frac{q(V - V_{oc})}{2kT}\right], \tag{3.37}$$

that should be added to the zero-field conductance of Eq. (3.29). Meanwhile, the capacitance remains the same as for the case of zero dc bias in Eq. (3.29). The physical meaning of the latter coincidence was explained above in Sec. 3.1.

3.2.5 Summary

Here we give more explicit results for the zero dc bias capacitance and conductance expressing the trigonometric functions introduced in Eq. (3.29),

$$C = \frac{cL_C^2}{\sqrt{2}}\sqrt{\frac{1}{L^2(\omega)} - \frac{1}{L^2(0)}} \tag{3.38}$$

$$G = \frac{L_R^2}{\sqrt{2}R}\sqrt{\frac{1}{L^2(\omega)} + \frac{1}{L^2(0)}} \tag{3.39}$$

where $L(\omega)$ from Eq. (3.30) is frequency dependent through L_C, defined in Eq. (3.7), and $L(0)$ is given by Eq. (3.30) with the L_C term excluded.

As discussed above in Sec. 3.1, the active region of the system is predominantly defined by the minimum decay length. Therefore, frequency-dependent effects are

dominant when the minimum decay length is L_C. Thus, there is a characteristic frequency,

$$\omega_0 = \frac{1}{c\rho}\left(\frac{1}{L_0^2} + \frac{1}{L_R^2}\right), \tag{3.40}$$

which discriminates between the regimes of low and high frequencies, such that

$$C = \frac{cL_RL_0}{\sqrt{L_0^2 + L_R^2}}, \quad G = \frac{L_RL_0}{\rho\sqrt{L_0^2 + L_R^2}} \quad \text{when} \quad \omega \ll \omega_0 \tag{3.41}$$

and

$$C = \sqrt{\frac{c}{2\omega\rho}}, \quad G = \sqrt{\frac{c\omega}{\rho}} \quad \text{when} \quad \omega \gg \omega_0. \tag{3.42}$$

These equations represent the core of our results, are fully consistent with the qualitative analysis in Sec. 3.1 above, and allow for simple modifications describing the cases of reverse and forward dc bias. Namely, the reverse bias case is described by the same equations after the replacement $L_0 \to L_0 \exp[u_1(0)/2]$. The results for forward bias are only different from those of zero bias by the addition of G_+ from Eq. (3.37) to the conductance in Eq. (3.39).

3.2.6 Small 1D Superstrate Cell

A small cell is defined as a cell with spatial dimension $l \ll L$ [Ref. Fig. 3-4(d)]. This definition can be deceiving because although the size of the sample is fixed, the screening length is a strong function of the applied bias, and saturation current. For example, a sample which is considered small under a relatively low applied bias may be considered a large sample if it is subject to strong forward bias. We find it instructive to show that when the cell is small, $l \ll L$, the above developed formalism reduces to the results used in the standard practice of admittance characterization.

Consider a 1D small cell with applied voltage similar to that of the large cell case discussed above. One of the boundary conditions is that there is no current produced

at the end of the device, *i.e.* $\partial X/\partial x = 0$ at $x = l$. Given this boundary condition and the fact that the ac component of the potential remains nearly constant over the length of the cell, Eq. (3.25) can be integrated once from $x = 0$ to $x = l$ yielding,

$$-\frac{dX}{dx}\Big|_{x=0} = X(0)\left[\frac{1}{L_0^2}(e^{u_1}-1)+\frac{1}{L^2}e^{i\psi}\right]l \tag{3.43}$$

Therefore, the admittance for a 1D small superstrate cell is given by,

$$Y = -\frac{1}{\rho}\left[\frac{1}{L_0^2}(e^{u_1}-1)+\frac{1}{L^2}e^{i\psi}\right]l. \tag{3.44}$$

The capacitance then becomes $C = cl$.

3.3 Two-Dimensional Systems

Having redefined the dimensionality of the system parameters as described in Sec. 3.1, all the equations describing the 2D case become similar to their 1D counterparts, except that the second derivative changes to the Laplacian, so that Eq. (3.25) transforms to

$$\frac{1}{r}\frac{\partial X}{\partial r}+\frac{\partial^2 X}{\partial r^2} = \left[\frac{e^{u_1}-1}{L_0^2}+\frac{1}{L^2}e^{i\psi}\right]X = 0. \tag{3.45}$$

The expression for admittance will depend on the particular electrode geometry. For the sake of definiteness, we concentrate on substrate configuration photovoltaics (such as, *e.g.* CuIn(Ga)Se or a-Si:H) where the conductive electrode is buried under the semiconductor layers and the resistive electrode remains accessible [56]. As shown in Fig. (3-6), we will assume a roundish contact of radius a made to the resistive electrode; both the cases of $a \ll L$ and $a \gg L$ are possible.

Because the current collected by the contact is given by the current density times

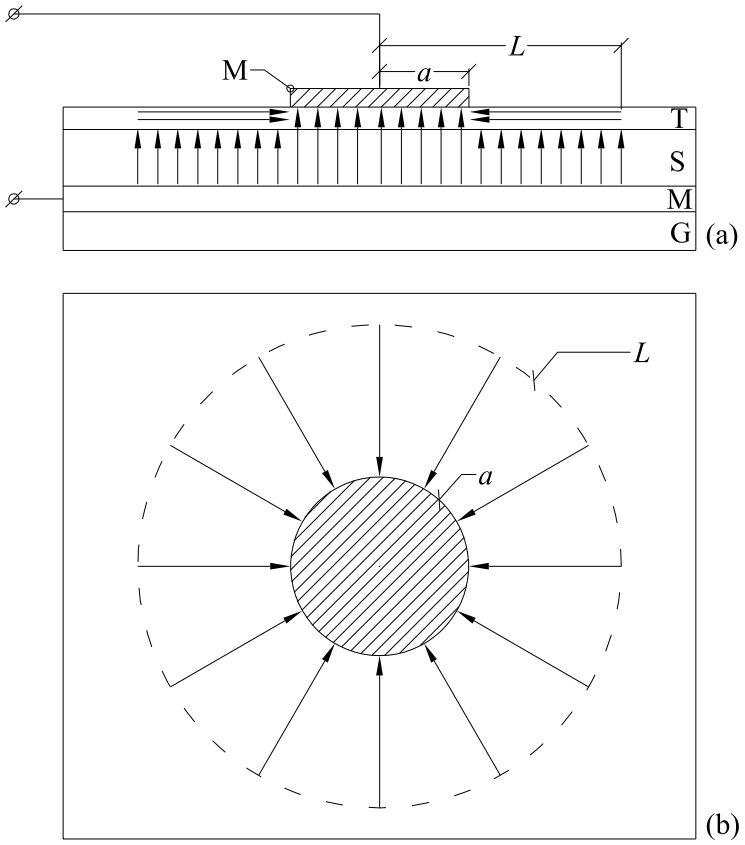

Figure 3-6: A small ($a \ll L$) 2D substrate cell with the cross-sectional view shown in (a) and the top view in (b). The device components are labeled as M, T, S, and G for metal, TCO, semiconductor, and glass, respectively. The active region of current collection is delineated by the decay length L which is large relative the cell radius a. Therefore, the admittance is dependent upon the region beyond the electrode area.

the contact perimeter, the expression for the admittance becomes

$$Y = -\frac{2\pi a}{\rho}\frac{1}{X(a)}\frac{dX}{dr}\Big|_{r=a}, \tag{3.46}$$

where ρ is the sheet resistance defined in Sec. 3.1.

We do not consider the trivial case of a large substrate contact, $a \gg L$, which reduces to the 1D case since the first term on the left-hand-side of Eq. (3.45) is immaterial. In particular, the results for capacitance and conductance coincide with

those of Sec. 3.2.5 to the accuracy of the multiplier $2\pi a$ introduced in Eq. (3.46).

However, the case of a small substrate contact ($a \ll L$) has some new features which are described next. We note here that such a case does not fall into either the small or large device categories analyzed above (cf. Sec. 3.1). The geometry here is such that the device remains infinitely large, while the current collecting part of it has a small linear size.

3.3.1 Small 2D Substrate Cell Under Zero dc Bias

Following the analysis in Sec. 3.2, consider first the case of zero dc bias. The 2D counterpart of Eq. (3.27) takes the form

$$\frac{1}{r}\frac{\partial X}{\partial r} + \frac{\partial^2 X}{\partial r^2} - \frac{X}{L^2}\exp(i\psi) = 0. \tag{3.47}$$

The solution of Eq. (3.47) is $X \propto K_0[(r/L)\exp(i\psi/2)]$ where K_0 is the zero-order Hankel function of the first kind, whose small argument behavior is described by [55, 57] $X \propto \ln[(r/L)\exp(i\psi/2)]$. Substituting the latter into Eq. (3.46) yields

$$Y = \frac{2\pi}{\rho}\frac{1}{\ln(L/a) - i\psi/2}. \tag{3.48}$$

Taking into account $L \gg a$ the corresponding conductance and capacitance become

$$G = \frac{2\pi}{\rho}\frac{1}{\ln(L/a)}, \tag{3.49}$$

$$C = \frac{\pi}{\rho\omega}\frac{1}{[\ln(L/a)]^2}\arctan\left[\frac{L_0^2 L_R^2}{L_C^2\,(L_0^2 + L_R^2)}\right]. \tag{3.50}$$

The high and low frequency regions defined by the same characteristic frequency in Eq. (3.40) correspond to the capacitance

$$C = \frac{c\pi L_R^2 L_0^2}{[\ln(L/a)]^2(L_0^2+L_R^2)} \quad \text{when} \quad \omega \ll \omega_0, \tag{3.51}$$

$$C = \frac{\pi^2}{2\rho\omega}\frac{1}{[\ln(L/a)]^2} \quad \text{when} \quad \omega \gg \omega_0. \tag{3.52}$$

We observe, in particular, that the low frequency capacitance is larger than the geometrical area capacitance, $c\pi a^2$, by a factor of $\sim L^2/a^2 \gg 1$. This increased capacitance is due to the fact that the lateral current is collected from a region, L, greater than the size of the metal contact, a, as illustrated in Fig. 3-6.

3.3.2 Small 2D Substrate Cell Under Reverse dc Bias

For the case of reverse bias, it is difficult to extend the 'semi-classical' approach used in Sec. 3.2.3 to the 2D case. However, a sufficient approximation here is that the inequality $L_- \gg L_0$ enables one to simply treat $\exp[u_1(r)]$ as a constant whose value is determined by the applied bias. This leads to the same conclusion as the 1D case reverse bias regime; the only modification to the zero-bias results is a replacement $L_0 \to L_0 \exp[u_1(0)/2]$ in Eqs. (3.48) - (3.51).

3.3.3 Small 2D Substrate Cell Under Forward dc Bias

The case of a considerable forward bias can be treated with the same 'ultra-quantum' approximation applied above in Sec. 3.2.4; in fact, the extension of that approximation to the 2D case is well known [55, 57]. In place of Eq. (3.34) one obtains,

$$\frac{r}{X}\frac{dX}{dr}\Big|_a^{a+L_+} = \int_a^{a+L_+}\left[\frac{e^{u_1}-1}{L_0^2}+\frac{e^{i\psi}}{L^2}\right] r dr. \tag{3.53}$$

Along the same lines as in Sec. 3.2.4, the upper limit of logarithmic derivative on the left-hand-side is calculated with the function X in the zero bias case, and Eq. (3.36) is used to evaluate the integral. The result for capacitance remains the same as for zero bias case, while conductance is larger than in Eq. (3.49) by the voltage-dependent contribution,

$$G_+ = \frac{\pi}{6\rho} \exp\left[\frac{q(V - V_{oc})}{2kT}\right]. \tag{3.54}$$

3.3.4 Small 2D Superstrate Cells

For the case of a 2D small superstrate cell we integrate the two-dimensional Eq. (3.45) over the area A and apply the two-dimensional form of the divergence theorem, $\int \nabla^2 X dA = \oint \nabla X dl = -(1/\rho) \oint j_{2D} dl = -J/\rho$, where j_{2D} is the surface current density and dl is the vector element of the cell perimeter. The right hand side integrand is considered constant in the small cell case and, therefore, the solution is simply the integrand times the total area, A. As a result, the admittance is given by Eq. (3.44) where l is replaced with A, in particular, the capacitance is given by $C = cA$.

3.4 Practical Implications

We believe that our work introduces a diagnostic technique applicable to practically any semiconductor junction. Here we discuss in more detail the case of thin-film photovoltaics to provide examples of device parameter evaluation.

For definiteness, we focus on the substrate type of photovoltaics, particularly CuIn(Ga)Se_2 with the typical structure (glass/metal/CuIn(Ga)Se_2/CdS/buffer) and the following parameters: [56] buffer (TCO) layer sheet resistance of $\rho \sim 10\ \Omega/\square$; current density $j_0 \sim 0.03$ A/cm^2 (for 1 sun light intensity); shunt resistance $R \sim 10^4$ Ω·cm^2; and capacitance $c \sim 1$ nF/cm^2. Corresponding to these parameters are the decay lengths $L_0 \sim 0.3$ cm and $L_R \sim 30$ cm, and the characteristic frequency $\omega_0 \sim 10^9$

rad/s. Note, however, that the current j_0 can be decreased and the length L_0 increased by, respectively, four and two orders of magnitude by decreasing the light intensity from 1 sun to the typical ambient room light. In addition, we assume a testing frequency range of $\omega \sim 1$ to 10^7 rad/s, corresponding to the capacitive decay length $L_C \sim 10 - 10^4$ cm.

Consider as our first example a small cell of radius $a = 0.1$ cm deposited as a current collection terminal on the buffer layer; the other terminal is connected to the metal electrode buried under the semiconductor. The inequalities $a \ll L_0$ and $\omega \ll \omega_0$ correspond to the low frequency regime of a 2D small cell with the conductance and capacitance given by Eqs. (3.49) and (3.51) for zero dc bias. Measuring G and C under these conditions, will give information about ρ and j_0. The capacitance as a function of frequency is presented in Fig. 3-7.

Also, in the low frequency regime the measured frequency-dependent capacitance will have to be attributed to the intrinsic $c(\omega)$, if any, which was considered constant in the above formulation, thus giving the standard admittance spectroscopy information about the material related to space charge density and defect energy spectra. We note that the typical frequency dependence for $c(\omega)$ is logarithmically weak (see Refs. [18, 19, 20]) and can hardly be mistaken for the above predicted $C \propto 1/\omega$ in the high frequency region.

Under the same conditions, decreasing the light intensity will eventually put the system into the regime where $L_R \ll L_0$ and L_R becomes the predominant decay length. This crossover, after which C and G become independent of light intensity, will determine the shunt resistance R. One conceivable outcome of such experimenting is that the crossover will take place at a light intensity which is above the expected value *due to the presence of a shunt* at distance L_0 from the cell. Therefore, our proposed capacitance diagnostics have the potential of detecting shunts and their distribution in the system.

Another effect of low light intensity is that the characteristic frequency will change from $\omega_0 \sim 10^9$ to 10^5 rad/s, well into the testing frequency range, which makes it possible to observe the crossover between the high and low frequency regimes, thus determining ω_0 and related parameters.

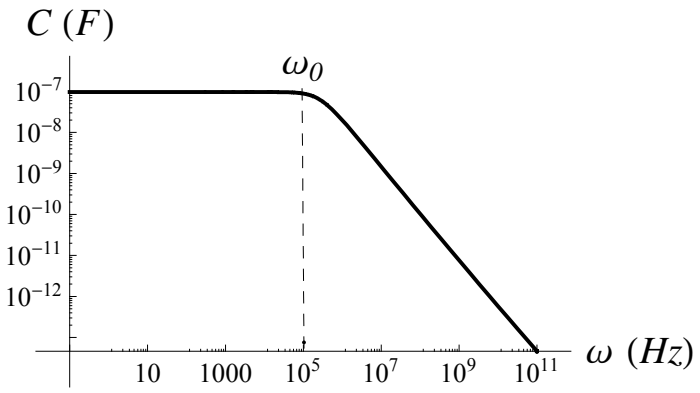

Figure 3-7: Prediction of capacitance as a function of frequency for a small 2D substrate cell under the conditions discussed in the running text. The measured capacitance is constant in the region $\omega \ll \omega_0$ and goes as $1/\omega$ in the region $\omega \gg \omega_0$, where $\omega_0 \sim 10^5$ rad/s.

Consider now effects of dc biasing. A forward dc bias changes the conductance by G_+ given in Eq. (3.54) and the measured bias dependence of G_+ will determine the open circuit voltage in the system. A reverse bias, on the other hand, will reduce the effective decay length, $L \approx L_0 \exp[u_1(0)/2]$, eventually switching the system into the large cell regime $L \ll a$. This will simultaneously provide an independent method to determine V_{oc} and the ideality factor.

As a second example, consider the case of the same system but without buffer (i. e. one step before the device is finished), having a small metal electrode deposited on CdS. A significant difference with the previous case is the higher sheet resistance $\rho \gtrsim 10^7$ $\Omega/\Box$, which makes the decay lengths much shorter: $L_0 \sim 3$ μm, $L_R \sim 0.03$ cm, $L_C \sim 0.01 - 10$ cm, but the characteristic frequency remains the same (note that ρ cancels out in the definition for ω_0, since $L_0^2 \propto 1/\rho$). These parameters correspond

to the large cell regime ($a \gg L$) described by the results for the 1D case given in Sec. 3.2.5, based on which one can extract the significant system parameters similar to the previous example. One beneficial feature here is that the information related to system leakage (R) can be determined prior to finishing the device.

Similar to the latter example, the above described techniques will facilitate testing for leakiness and other parameters of various Schottky diode type structures before finishing. Potentially, it can be used as the integrity and uniformity diagnostic tool for dielectric coating on metals.

3.5 Conclusions

In conclusion, we have developed a theory of ac response by systems of distributed diodes in parallel with resistors and capacitors connected through resistive electrodes that can represent many practical devices including photovoltaics and Schottky junctions. In particular, we have shown that:

1) There exist three lateral decay lengths related to the system diodes, shunt resistors, and capacitances respectively that determine the effective, frequency-dependent lateral decay length L and describe the physics of ac response in such distributed systems;

2) The response is frequency-independent below a certain characteristic frequency; above which it strongly depends on testing frequency;

3) The 1D and 2D systems behave similarly in the large device regime, $l \gg L$, where l is the device lateral dimension, while in the small device regime, $l \ll L$, 2D systems exhibit certain unique behavior;

4) Both the capacitance and conductance are described by closed form analytical expressions as functions of frequency and dc bias and are parametrically dependent on system material characteristics;

5) Our theoretical results establish a basis for a type of admittance characterization applicable to a wide variety of semiconductor structures including photovoltaics and Schottky junctions.

Chapter 4

$1/f$ Noise in Chalcogenide Glasses

The recent developments in phase change memory (PCM) [21] revived interest in the physics of chalcogenide glasses. We recall that PCM utilizes electrically initiated, reversible amorphous-to-crystalline phase changes in multi-component chalcogenide materials, such as $Ge_2Sb_2Te_5$ (GST); their markedly different phase resistances are used as the two logic states.

Not surprisingly, the new technology triggered a 'rediscovery' of the underlying materials: understanding chalcogenide glasses became vitally important for PCM device engineering. To some degree, that 'rediscovery' has overlooked a number of important concepts (see Sec. 4.1 below) concerning the physics of localized atomic and electronic states in glasses that had been previously established in the 1970s and 1980s. Instead, several concepts more relevant to classical crystalline materials (Si, Ge, and $A^{III}B^{IV}$) were postulated to hold true for chalcogenide glasses, including those of high hole mobility, donors and acceptors, hopping conduction, avalanche processes, etc. [11, 58] Employing the highly developed physics of crystalline materials, rather than the earlier acquired understanding of glasses, made it convenient to extensively apply commercial software, developed for the crystalline device industry, in which the many fitting parameters enable one to tweak crystalline-based models to match practically any of the dependencies measured in PCM glasses [59].

Here we analyze $1/f$ noise, which is a disorder related phenomenon whose features

are very sensitive to the details of underlying physics. The experimental observations [60, 61, 62, 63] show that in chalcogenides the $1/f$ noise power spectrum amplitude remains proportional to the square of dc current under low enough voltages, while it becomes superlinear in dc current when the dc voltage and current increase toward their switching values. Such nonlinear $1/f$ noise was observed in other systems, of which the most similar is a-Si:H [64].

Our approach here is based on considering all possible sources of $1/f$ noise consistent with the established properties of atomic and electronic localized states in chalcogenide glasses. It appears appropriate then to start with a brief survey of such properties, which we present in Sec. 4.1 below. In Sec. 4.2 we discuss specific atomic and electronic excitations capable of generating $1/f$ noise in chalcogenide glasses and show how $1/f$ noise results from an exponentially broad spectrum of random relaxation times. Sec. 4.3 gives semi-quantitative estimates of the Hooge parameter corresponding to conceivable sources of $1/f$ noise in chalcogenide glasses. As the corresponding rigorous derivations turned out to be rather long, we chose to present them in the Appendices to this dissertation. Conclusions are given in Sec. 4.4.

4.1 Survey of Atomic and Electronic Localized States in Chalcogenide Glasses

Most of the information about localized states (excitations) in glasses was acquired by 1980; the comprehensive review by Mott and Davis [22] covers most of the electronic component with more limited reviews given later in Refs. [65, 66]. The atomic component was described in the reviews of Refs. [67, 68, 69] and applied to PCM in Ref. [70]. Here, we briefly summarize the major concepts related to possible sources of noise.

4.1.1 Localized Atomic Excitations in Glasses

Localized atomic states in glasses attracted a great deal of attention in connection with anomalous properties observed at low temperature (T), such as the specific heat $C \propto T$, thermal conduction $\chi \propto T^2$, absorption, and many others. These properties are now commonly understood based on the concept [71, 72] of double well potentials (DWP), according to which some atoms or small groups of atoms retain their mobility, even at very low T, by moving between two energy minima separated by a potential barrier W_B, as illustrated in Fig. 4-1. The potential barriers and the differences between the energy minima (asymmetry) E are described as random quantities that are almost uniformly distributed within their respective energy intervals, in particular $W_{B,min} < W_B < W_{B,max}$.

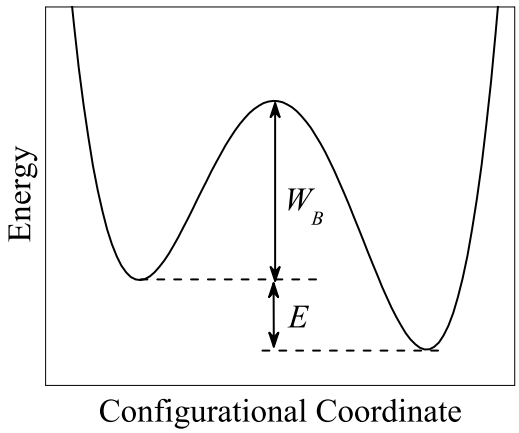

Figure 4-1: Double well atomic potential (DWP) with the barrier height W_B and difference between energy minima E. An atom can move between the minima causing fluctuations in atomic and electronic properties of the glass.

It is essential for our consideration that the DWP concept introduces the *exponentially broad distribution of relaxation times* $\tau(W_B) = \tau_0 \exp(W_B/kT)$. Because the barrier height W_B is a random quantity with almost uniform probabilistic dis-

tribution $g(W_B) \approx 1/\Delta W_B, \quad \Delta W_B = W_{B,max} - W_{B,min}$ between its boundary values, the maximum and minimum relaxation times in the system are estimated as $\tau_{max(min)} = \tau_0 \exp(W_{B,max(min)}/kT)$. The relaxation time distribution takes the form

$$\rho(\tau) = g(W_B) \left| \frac{dW_B}{d\tau} \right| = \frac{kT}{\tau \Delta W_B}, \quad \tau_{min} < \tau < \tau_{max}. \tag{4.1}$$

For relatively high temperatures, above tens of Kelvins, the atomic tunneling phenomena in DWP can be neglected, in which case the joint probabilistic distribution of DWP parameters E and W_B takes the form

$$\rho(E, \tau) = \frac{kTP_T}{\tau \Delta W_B} \equiv \frac{P}{\tau} \tag{4.2}$$

The parameters of the DWP distribution in glasses exhibit surprisingly modest variations between glasses of different chemical composition and are experimentally estimated as $P_T \sim 10^{20} - 10^{21}$ eV^{-1}cm^{-3} and $\Delta W_B \sim W_{B,max} \sim 1$ eV; correspondingly, $P \sim 10^{18} - 10^{19}$ eV^{-1}cm^{-3}. The DWP relaxation time interval $\tau_{min} < \tau < \tau_{max}$ is exponentially broad ranging from τ_{min} comparable to the characteristic atomic vibration times $\tau_0 \sim 10^{-13}$ s to extremely long times τ_{max} on the scale of months and years (at room T).

DWP interact with both the atomic and electronic systems of a glass. In particular, they can affect the scattering of charge carriers. Since the two different equilibrium configurations in a DWP have different scattering cross sections, random transitions in DWP will modulate the charge carrier mobility. In addition, atomic transitions in DWP can modulate the electron energies through the deformation potential or electric dipole interaction, causing fluctuations in the concentration of charge carriers above the mobility gap.

Later work [73, 69] extended the DWP model by assuming a continuous distribu-

tion (Fig. 4-2) of microscopic spring constants k in the anharmonic atomic potential

$$V(x) = kx^2/2 + Bx^3 + Cx^4,$$

where x is a generalized configuration coordinate of unspecified microscopic nature, and B and C are constant coefficients of expansion. The region of $k < 0$ represents DWP of relatively low concentration related to the decay of the distribution tail toward small and negative values. Furthermore, its rapid decay suggests that the majority of DWP are "soft" atomic potentials with $k \ll \langle k \rangle$ where $\langle k \rangle$ is the average spring constant close to the typical values in solids. Among the many verified phenomena related to soft atomic potentials [69, 74], here we emphasize their gigantic susceptibility $\propto 1/|k|$, implying an abnormally strong interaction with electrons [75].

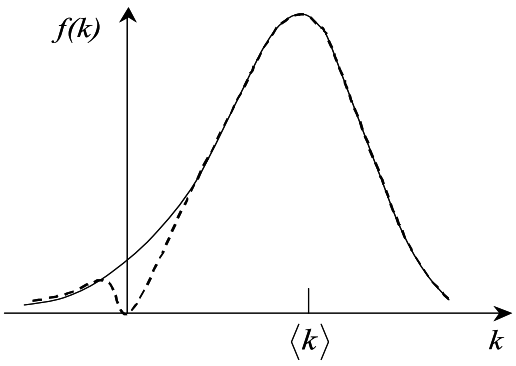

Figure 4-2: Probabilistic distribution of local spring constants in a glass. The solid line shows the original distribution suggested in Ref. [73] while the dashed line accounts for the later established [69] low-k singularity $f(k) \propto |k|$. Soft atomic potentials are characterized by $k \ll \langle k \rangle$.

4.1.2 Localized Electronic Excitations in Glasses

Experimental data on the various electronic properties of chalcogenide glasses can be broken into two groups, one of which testifies in favor of a high concentration of

localized states, while another states the opposite. The latter group includes: lack of electron spin resonance (ESR) signal, absence of hopping conduction, optical gap G_0 approximately equal to the mobility gap G, and lack of absorption of photons of energy much lower than G. The former group, on the other hand, includes observations of strong photoinduced ESR corresponding to the electron concentration $\lesssim 10^{20}$ cm^{-3}, photoluminescence with energy close to $G/2$, d.c. screening length revealing the defect concentration of $\lesssim 10^{19}$ cm^{-3}, strong pinning of the Fermi level close to the mid gap, photoinduced mid gap absorption, and photoinduced change in the mid-gap photoluminescence. The spectroscopic aspects of these facts are illustrated in Fig. 4-3.

A solution to the above controversy was proposed by Anderson [76] who put forward the concept of negative-U (negative Hubbard or negative correlation) energy implying that two identical charge carriers localized at the same center will attract in spite of the Coulomb repulsion. As a result, double occupancy of a localized state becomes energetically more favorable than single occupancy of two localized states, such that the equilibrium occupation is $n = 2$ (electrons or holes), while $n = 1$ can only exist as an excited state. This obviously explains the lack of ESR in spite of high concentration of localized (doubly occupied) states in the vicinity of the Fermi level. Also, the photoinduced effects become attributable to the non-equilibrium, single-occupancy states excited by higher energy photons.

The nature of negative-U energy is specified as being related to an abnormally strong electron-lattice interaction for localized charged carriers. The energy of $n = 0, 1, 2$ localized carriers is described as

$$E_n(x) = nE_0 + kx^2/2 - nQx + U_c\delta_{n,2}, \tag{4.3}$$

where E_0 is the bare energy of the center, x is the lattice deformation around the cen-

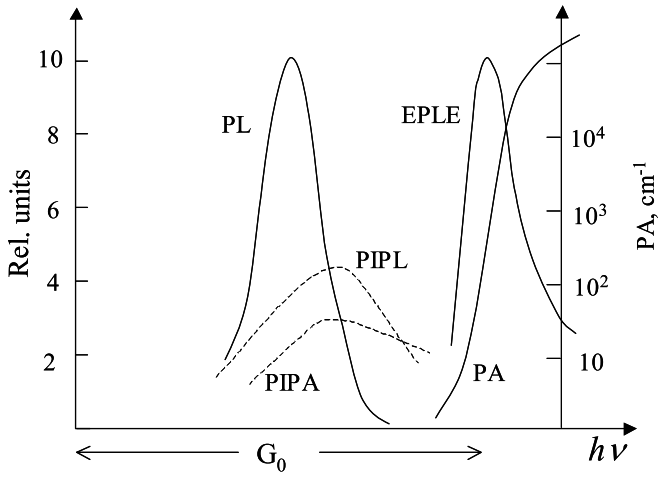

Figure 4-3: Sketch of the typical spectroscopic data in chalcogenide glasses: photoabsorption (PA), photoluminescence (PL), efficiency of photoluminescence excitation (EPLE), photoinduced PL enhancement (PIPL), and photoinduced photoabsorption (PIPA) vs. photon energy. All the curves except PA are plotted against the left vertical axis.

ter, Q is the deformation potential, and U_c is the Coulomb repulsion energy applicable when $n = 2$. The dependencies in Eq. (4.3) are illustrated in Fig. 4-4.

The equilibrium energies are given by the equation

$$E_n = nE_0 - n^2 w + U_c \delta_{n,2} \quad \text{with} \quad w \equiv \frac{Q^2}{2k}, \tag{4.4}$$

where w is called the polaron shift. The correlation energy is given by

$$U \equiv E_2 - 2E_1 = -2w + U_c. \tag{4.5}$$

The negative U corresponds to a strong polaron effect with $w > U_c/2$.

By the Franck-Condon principle, the characteristic energy of the absorbed light in Fig. 4-4 is $|E_2|$ while that of emission (PL) and photo-induced absorption is $2|E_1|$, and, assuming U_c relatively small, $|E_2| \approx 4|E_1|$, consistent with the data in Fig. 4-3.

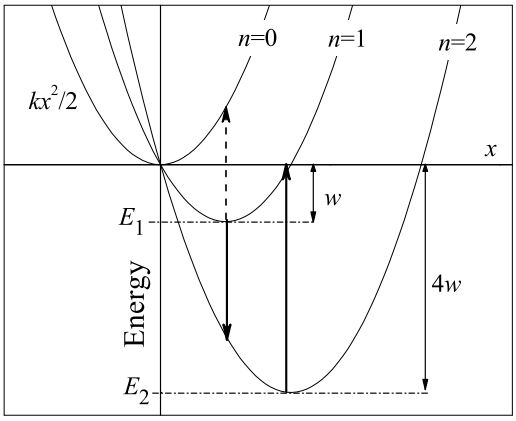

Figure 4-4: Energies of n localized charge carriers vs. the local lattice deformation x. The upward solid arrows represent absorption and the downward solid arrows represent photoluminescence processes. The dashed arrow indicates photoinduced photoabsorption from the nonequilibrium $n = 1$ state. E_1 and E_2 represent the equilibrium energies for $n = 1$ and $n = 2$ localized carriers. w is the polaron shift and U_c is assumed to be relatively small.

These transitions are shown in Fig. 4-5 with respect to the mobility gap. Comparing Figs. 4-3, 4-4, and 4-5 enables one to estimate $w \approx G/4$ (although w can be somewhat different for the cases of electrons and holes [22]).

Drawing similar energy levels for holes and allowing for some dispersion, leads to the right diagram in Fig. 4-5 that explains how the Fermi level is pinned by a high concentration of 2e and 2h states forming a gapless spectrum of two particle excitations. In addition to the pinning (2e,2h) states, shown in the same diagram are band tails possessing the characteristic decay scales on the order of several hundredths of eV. They can contribute to optical absorption and act as shallow traps underlying dispersive transport and other phenomena [65]. As shown in Fig. 4-5, the one-particle excited states 1e and 1h are obtained through the partial ionization of (2e,2h). Possessing energies of approximately $w = G/4$ from the corresponding mobility edges,

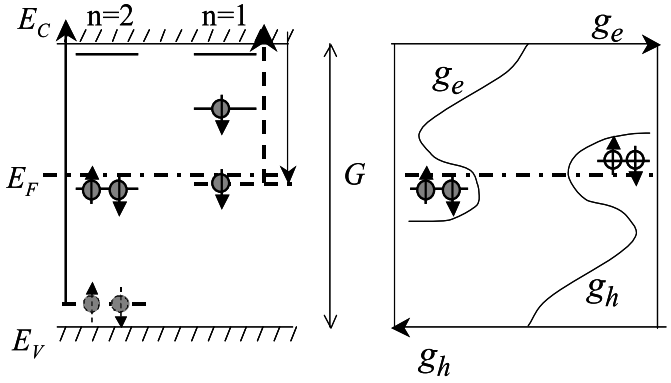

Figure 4-5: Left: one-particle energy levels (i.e. energy per particle) corresponding to $n = 2$ and $n = 1$ electrons in the mobility gap. The levels without electrons represent the bare energy. Solid and dashed lines indicate thermodynamic and optical energy levels, respectively. The dashed electron level close to the valence band edge represents the energy needed to optically ionize the 2e state (solid upward arrow); the solid level close to the midgap represents the energy needed to thermally ionize the same 2e state. The arrows have the same meaning as in Fig. 4-4. Right: density of the 2-electron (g_e) and 2-hole (g_h) states vs. their one-particle energies where negative-U centers near the Fermi level provide its pinning.

they can affect transport phenomena [66].

The microscopic nature of negative-U centers is not particularly important for the purposes of this work; here we limit ourselves to a brief comment on the subject. We note that the negative-U phenomenon can be simply illustrated in terms of a mechanical analogy with two electrically charged balls, each of weight Q, that can be attached to either two different elastic springs or one such spring, as depicted in Fig. 4-6.

Street and Mott [77] proposed a microscopic model where 2e and 2h states correspond to certain defect states (D^- and D^+), while 1e and 1h are the same dangling bond (D^0). Kastner *et. al* and Kastner and Fritzsche [78] introduced more specific consideration taking into account the chemical nature of chalcogenide forming atoms; in their popular notation D^- and D^+ are represented as C^{1-} and C^{3+} where the

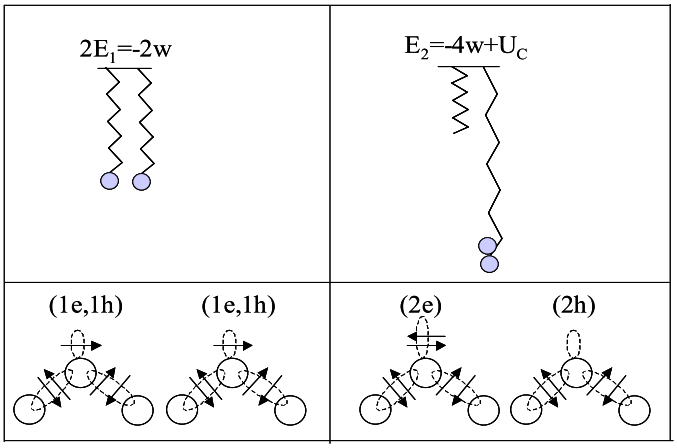

Figure 4-6: Mechanical analogy of the negative-U effect consisting of two elastic springs and two charged balls that can be attached to the springs either separately or together (top row) and its simple model based on the valence bonds representation (bottom row) where two electrons can occupy the states of two broken bonds or one dangling bond. The right column is energetically more favorable when $w > U_c/2$.

superscript indices refer to defect coordination numbers.

Later work [75] emphasized that a theoretical description of the negative-U must explain the observed significant polaron shift w. The required shift was attributed to centers with abnormally small spring constants k (soft atomic potentials) that exist in glasses due to their inherent structural disorder, as was discussed in connection with Fig. 4-2. In particular, the polaron shift $w \approx G/4$ implies the spring constant $k_G \approx \langle k \rangle (2\langle w \rangle / G) \ll \langle k \rangle$ where $\langle w \rangle \lesssim 0.1$ eV is the average polaron shift corresponding to the average spring constant $\langle k \rangle$ which describes the macroscopic properties of glasses.

It should be remembered that the 2e and 2h gapless excitations typically have extremely long relaxation times related to the necessity of carrying a heavy polaron cloud (i. e. atomic deformation) in the course of electron transitions. Here we will describe such slow transitions in terms of electronic DWP with a transition barrier W_B related to the polaron shift. The two minima of such a DWP will correspond to the charge states (0,0) and (2e,2h) of two centers with energies close to the Fermi

level.

The transition barrier $W_B \approx 8w \approx 2G$ (first estimated by Phillips [79]) is high enough to fully suppress dc hopping conduction that could occur through electron hopping between centers separated by distances of the order of the average inter-center distance [22]. Assuming, for specificity, $2G \approx 1.6eV$ for the case of GST glasses and implementing the standard estimates [22] yields the multiplier $\exp(-2G/kT) \sim 10^{-27}$ in the electron transition rate. This predicts hopping conduction many orders of magnitude below what is observed both in the non-glassy semiconductors (such as a-Si) and the band conduction in chalcogenide glasses [small by the factor $\exp(-G/kT)$ instead of $\exp(-2G/kT)$ for hopping].

In the latter estimate, we have neglected both the quantum contribution caused by the overlap of the wave functions of spatially close 2e and 2h centers and the Coulomb interaction of 2e and 2h pairs. It was shown [80] that both corrections are significant for the case of *spatially close* pairs, sometimes called intimate pairs, which can decrease the barrier height by several times. In particular, the intimate (2e,2h) pairs partially decrease their energy due to the strong Coulomb interaction, which relaxes the requirement of very soft atomic potentials with $k \approx k_G$. Because higher k values result in smaller w, the factor $\exp(-8w/kT)$ describing the suppressing effect of a polaron cloud on the electronic transition becomes less significant, allowing for much higher hopping probabilities.

Lacking more accurate information, one can resort to the data [81] on alternating current (ac) conduction in chalcogenide glasses that is comparable to that of other noncrystalline semiconductors at low frequencies and strongly decays at higher frequencies. Because ac conduction is attributed to electron hopping between close centers [81], these observations can be explained [80] by significant suppression of the transition barrier for intimate pairs.

The activation relaxation time for the electronic DWP can be estimated as

$$\tau = \tau_{min} \exp\left[\frac{2R}{a} + \frac{\Delta W_B(R)}{kT}\right], \tag{4.6}$$

with $\tau_{min} = \tau_0 \exp\left[W_B(R_{min})/(kT)\right]$ and $\Delta W_B = W_B(R) - W_B(R_{min})$, $(\Delta W_B)_{max} \approx 2G$ where R is the intercenter distance, a is the electron localization radius at the center, $\exp(2R/a)$ describes the electron tunneling, and $W_B(R_{min})$ is the activation barrier for intimate pairs separated by the distance $R_{min} \sim a$. Because R is a random quantity with the probabilistic distribution $4\pi R^2 N_U$ where N_U is the concentration of negative-U centers, the probabilistic distribution of relaxation times becomes qualitatively similar to that in Eq. (4.2),

$$\rho(E,\tau) = \frac{P}{\tau}, \quad P \approx \frac{\pi N_U^2 a^3}{4\Delta E_U} \frac{\left[\ln(\tau/\tau_{min})\right]^2}{1 + G/kT}, \tag{4.7}$$

where we have used a rough estimate $dW_B/dR \sim (\Delta W_B)_{max}/a$ and where ΔE_U is the total energy width of the negative-U center distributions that are approximately uniform in the proximity of the Fermi level. In what follows we neglect the logarithmicaly weak dependence of P vs. τ and treat it as a constant.

One outstanding feature of electronic DWP is the gigantic dipole moment $p = 2eR$ that for the typical $R = N_U^{-1/3}$ is many orders of magnitude higher than that of the atomic DWP discussed earlier. As a result, electronic DWP are expected to be a much stronger noise source.

For numerical estimates we use the values discussed in Section 9.4 of Ref. [22] that suggest $N_U \sim 10^{17} - 10^{18}$ cm^{-3} and $\Delta E_U \sim 0.025$ eV, yielding $P \sim 10^{15} - 10^{17}$ eV^{-1}cm^{-3}, which is lower than that of the atomic DWP. The transition time τ corresponding to the typical $a \sim 10$ Å, average $R \sim N_U^{-1/3}$, and $W_B \approx 2G \sim 2$ eV turns out to be long enough to fully suppress hopping conduction [79]. On the other hand, as mentioned above, spatially close (intimate) pairs can have much lower W_B

and exponentially shorter relaxation time than distant pairs, thus making noticeable contributions to the system noise in a broad range of relatively low frequencies.

We shall end this section with a conclusion of the existence of both atomic and electronic localized states described in terms of atomic and electronic DWP that have exponentially broad distributions of relaxation times covering the low frequency interval typical of $1/f$ noise measurements. These distributions are generally proportional to $1/\tau$, which is known [82, 83] to lead to the $1/f$ power spectrum of fluctuations (see below).

4.2 Possible Sources of $1/f$ Noise in Chalcogenide Glasses

$1/f$ noise in the electric current, also known as excess noise, is due to resistance fluctuations. Indeed, the measured mean-square-root current fluctuation δI related to $1/f$ noise, is proportional to the current I itself, in contrast to *e. g.* the equilibrium Nyquist noise. It is generally attributed to independent microscopic degrees of freedom ("fluctuators") possessing exponentially broad distributions of relaxation times that affect the material resistance. That general understanding originally suggested in Ref. [84] was later specified for a mechanism related to surface traps in semiconductors [85] (later supranationally generalized [86]). A possible contribution to the noise from structural two-level systems related to DWP [71, 72] was first discussed in Refs. [87] and [88].

As explained in Sec. 4.1 above, another class of "fluctuators" in glasses can be related to DWP of electronic nature formed by (2e,2h) pairs of charged carriers. We note that $1/f$ noise due to general intercenter hopping [89] was studied in Ref. [90]. However, it was pointed out [91] that in typical hopping insulators the characteristic relaxation times for such pairs have a relatively low upper limit due to the fact that

pairs separated by distances longer than the average are exponentially unlikely; hence, hopping conduction can hardly be a general source of $1/f$ noise [(2e,2h) pairs are an exception owing to their extremely long hopping times due to the strong polaron effect underlying the negative-U phenomenon].

The concept of "aggregates" formed by a set of pairs of centers (or "quasispins") was suggested [92] to explain the observed absence of the frequency cut-off of $1/f$ noise in hopping conductivity. These "aggregates" with strong Coulomb correlations were shown to have at least two metastable configurations that differed by the distribution of electron charges. The transitions between them are of multielectron nature with relaxation times that exponentially increase with the number of electron sites involved. We note however that the concept of "aggregates" is limited to the relatively low temperature regime, $kT \ll \Delta_C = [g(E_F)e^6/\kappa^3]^{1/2}$ where Δ_C is the Coulomb gap, [92] and κ is the dielectric permittivity. Given the typical $g(E_F) \lesssim 10^{18}$ cm^{-3} eV^{-1} and $\kappa \sim 10$, the opposite inequality holds for chalcogenide glasses at room temperature. As a result, the (2e,2h) pairs described in Sec. 4.1 remain the only candidate electronic two state systems in chalcogenide glasses.

Since the extensive work of 1960-1980, it has become common understanding [22] that dc conduction of chalcogenide glasses is due to the charge carriers excited above the mobility edge, at least for temperatures that are not too low ($T \gtrsim 100$ K), and in particular at room temperature. The noise in the corresponding conductivity $\sigma = ne\mu$ can be due to fluctuations in carrier concentration n and mobility μ which are attributable to fluctuations in some internal degrees of freedom.

Following the standard approach, we assume that each frequency component of the noise is related to the corresponding partial source of fluctuations characterized by its relaxation time $\tau = 1/f$ and that there exists a very broad distribution of τ. The shape of such a distribution $\rho(\tau)$ deduced from the noise spectrum $f(\omega) \propto 1/\omega$

becomes

$$\rho(\tau) = \left|\frac{d\omega}{d\tau}\right| f(\omega = 1/\tau) \propto \frac{1}{\tau}. \tag{4.8}$$

We observe that the distributions in Eqs. (4.1) and (4.7) fit the requirement of Eq. (4.8) quite nicely.

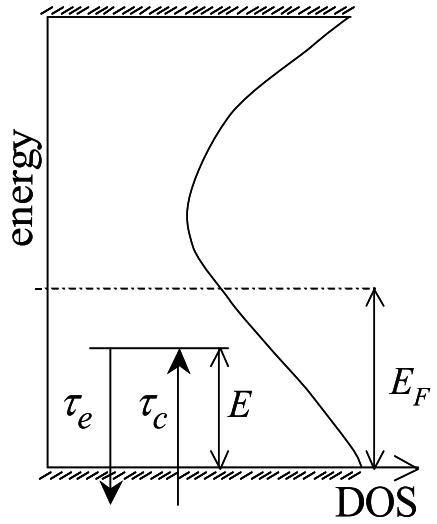

Figure 4-7: Sketch of the density of localized states in the mobility gap of a non-crystalline semiconductor and processes of the electron capture to and emission from the level of energy E. E_F is the Fermi energy.

The latter observation has a well known generalization: the relaxation time distribution $\rho \propto 1/\tau$ appears when τ is an exponential function of some uniformly distributed random parameter λ:

$$\rho(\tau) = \left|\frac{d\lambda}{d\tau}\right| \cdot const \propto \frac{1}{\tau} \tag{4.9}$$

where we have taken into account that $\lambda = \ln(\tau)$. In particular, λ is represented by the random quantities W_B/kT and $2R/a$ for the cases of atomic and electronic DWP in Eqs. (4.1) and (4.7), respectively.

One other conceivable representation of λ is related to generation-recombination

noise where $\lambda = E/kT$ with E being energy in a quasi-continuous spectrum of localized states in the mobility gap. [93, 94] In that case, the fluctuations in free carrier concentration are due to variations in the occupation numbers of localized states whose relaxation times $\tau \propto \exp(E/kT)$ are determined by trapping and detrapping of charge carriers. These relaxation times can be long enough to correspond to $\tau^{-1} = \omega$ in the low frequency region of the $1/f$ noise observations.

At the first glance, the relation $\rho(\tau) \propto 1/\tau$ takes place when the density of states (DOS) is uniform, $g(E) = const$, and it approximately holds true for a non-uniform $g(E)$ (of the kind depicted in Figs. 4-5 and 4-7) provided that its characteristic energy scale E_0 is considerably greater than kT. However, the partial contributions of states with different energies E are determined by their occupation numbers $n_E \propto \exp(E/kT)$ (in the region far from the Fermi level that is significant at frequencies that are not too low). As a result, one gets $g(E) \propto \exp(E/kT)$ for the density of *effective* (i. e. contributing) states. This entails

$$\rho(\tau) = g[E(\tau)] \left| \frac{dE}{d\tau} \right| = const \quad \text{and} \quad f(\omega) \propto \frac{1}{\omega^2}, \tag{4.10}$$

consistent with the result of the derivation in Ref. [94]. Furthermore, at very low frequencies, the noise is determined by the slowest active localized states that belong to the energy band of width $\sim kT$ around the Fermi level and behave effectively as a single energy level. Applying the known result for generation-recombination noise due to discrete levels [82, 83] predicts frequency-independent noise.

Assuming a strongly varying DOS, often modeled with an exponential shape [93, 94], $g(E) \propto \exp(-E/E_0)$ with $E_0 = const$, does not change the latter observation considerably: the generation-recombination mechanism in the bulk (also known as bulk trapping-detrapping) is generally inconsistent with the $1/f$ noise spectrum. (We note, however, that interface related trapping-detrapping can be significant

[85, 86], but that topic is beyond our present scope). The possibility of bulk trapping-detrapping related $1/f$ spectrum arises again [93, 94] if the charge carrier trapping time exponentially increases with E (i.e. $\tau_c \propto \exp(E/\varepsilon)$) due to the multiphonon nature of trapping processes where $\varepsilon \sim 0.01 - 0.03$ eV is of the order of the characteristic phonon energy [22, 95, 30]. It was shown indeed [96] that such multiphonon processes can be responsible for a variety of observed phenomena in non-crystalline semiconductors. In the case of strong energy dependence, $\varepsilon \ll kT$ and $\varepsilon \ll E_0$, the energy dependencies of occupation numbers and density of effective states become insignificant, which restores the $1/f$ noise spectrum.

We believe that the mechanisms discussed in this section cover all possible sources of bulk $1/f$ noise in chalcogenide glasses; they are: mobility and concentration fluctuations due to transitions in the atomic and electronic double well potentials; and fluctuations in carrier concentration due to generation-recombination multi-phonon processes in the quasi-continuous electronic spectrum.

In contrast to the latter statement, two papers [60, 61] studying $1/f$ noise in chalcogenide switches and PCM devices speculated that it could be due to avalanche-like multiplication processes. That hypothesis is inconsistent with the common knowledge that avalanche processes generate white noise (and even serve as white noise generators) [97], and that a concomitant $1/f$ component (if observed) is not directly related to the current flowing under avalanche breakdown conditions [98]. Ref. [61] attributed an observed $1/f$ component to avalanche processes simply based on the assumption that such processes are responsible for the observed switching. The authors of Ref. [60], while recognizing the contradiction with the established white spectrum, referred to the fact that a $1/f$ noise component had been observed in some avalanche based devices. We note that the simultaneous observation of two phenomena does not generally prove that they are in cause and effect relation with each other.

Finally, we note that our analysis is limited to the linear regime in which, "...the

current passing through the material is simply a probe of, and does not cause, the electronic noise" [64]. In spite of this limitation, we shall see in what follows (Table 4.1) that some of our analyzed noise mechanisms predict the noise amplitude to be a function of carrier concentration n_c, which is known to depend on voltage (or current) in chalcogenide glasses. As a result, even though the mechanisms are linear in nature some of our predictions will resemble nonlinear behavior, for example, $\Delta j^2 \propto n_c j^2 \propto j^3$, where j is the electric current density and Δj its dispersion. This kind of 'inexplicit' nonlinearity should be differentiated from models in which the current directly influences the noise, such as that of Ref. [64] or work regarding non-ohmic structures (devices) [97, 99, 100].

4.3 Quantitative Estimates of $1/f$ Noise in Chalcogenide Glasses

The standard quantitative metric of noise characterization is $(\Delta j)^2/j^2$ where the numerator represents the electric current density dispersion, and j is the average amplitude of the direct current density. In the frequency representation, $(\Delta j)^2$ is measured per unit frequency band making it independent of the measuring device frequency band $\Delta\omega$; hence, the ratio $(\Delta j)^2/j^2$ has the dimension of reciprocal frequency. The corresponding dimensionless metric, called the Hooge parameter [99], is defined as

$$\alpha = \frac{\Delta j^2}{j^2}\frac{\omega N_e}{2\pi}. \tag{4.11}$$

Physically, the Hooge parameter is the noise amplitude per charge carrier corresponding to the frequency band equal to the frequency per se, $f = \omega/2\pi$. It is understood that the direct current square is proportional to N_e^2, while the current dispersion is proportional to the total number $N_e \gg 1$ of charge carriers, whose contributions are

statistically independent. Experimentally estimated Hooge parameters for different systems range from 10^{-9} to 10.

The concept of the Hooge parameter has known limitations [101]. In particular, the original suggestion that it is independent of charge carrier concentration has been disproved many times (including in the results of the present work). However, we have chosen to keep it here because it is a commonly known dimensionless metric of $1/f$ noise that is often used in the representation of experimental results.

In this section we derive quantitative estimates of the Hooge parameter for all the conceivable cases of $1/f$ noise listed in Sec. 4.2 above. Here we employ certain approximations that make our consideration physically transparent and concise. The corresponding rigorous derivations leading to the same results are provided in the Appendices.

4.3.1 Double Well Potentials: Mobility Modulation Mechanism

We conjecture that some fraction of the scattering centers are DWP which can have two possible scattering cross-sections, different on average by $\Delta\sigma$, depending on the position of the atom at the time of scattering. This fluctuation in cross-sections results in a concomitant change in charge carrier mobility. As illustrated in Fig. 4-8, a cross-section change in just one scatterer will correspondingly change the number of scattering events ΔN_e, which results in the current density fluctuation

$$\Delta j_1 = j\frac{\Delta N_e}{N_e} = j\frac{l\Delta\sigma n_c}{N_e}$$

where we have employed the standard quasi-classical picture based on the mean-free-path concept with l representing the mean free path and n_c the charge carrier concentration. The corresponding dispersion is obtained through multiplication by

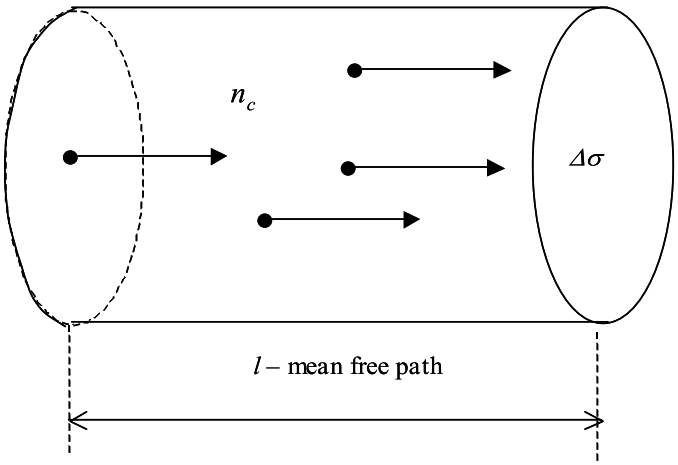

Figure 4-8: Sketch of the quasi-classical $1/f$ noise mechanism of electron (hole) mobility modulation by fluctuations of the electron (hole) scattering cross-section $\Delta\sigma$ due to DWP related scatters. Arrows represent the drift velocities of the charge carriers of concentration n_c.

the total number ΔN_{DWP} of DWP belonging to the frequency band $\Delta\omega$ of transition rates,

$$(\Delta j)^2 = j^2 \frac{(l\Delta\sigma)^2 n_c^2}{N_e^2} \Delta N_{DWP}.$$

Based on the distribution functions in Eqs. (4.2) and (4.7), and taking into account that $\Delta\omega/\omega = \Delta\tau/\tau$ the latter number becomes

$$\Delta N_{DWP} = PkTV \frac{\Delta\omega}{\omega}. \tag{4.12}$$

Substituting the above estimates into the definition of Eq. (4.11) finally yields

$$\alpha = \frac{(l\Delta\sigma)^2 n_c PkT}{2\pi} \tag{4.13}$$

where we have introduced the electron (hole) concentration $n_c = N_e/V$. This result differs from that of the rigorous consideration in Eq. (B.33) by a numerical multiplier

of order unity.

Consider first numerical estimates for the case of atomic DWP. Assuming the geometrical cross-section of the characteristic atomic dimension, we put $\sigma \sim 10^{-16}$ cm^2 and $\Delta\sigma \sim 10^{-17}$ cm^2 for its relatively small change. Also, we assume the typical $l \sim 100$ Å, room temperature $kT = 0.025$ eV, and the electron concentration $n_c \sim 10^{16}$ cm^{-3}. Using then $P \sim 10^{18} - 10^{19}$ eV^{-1}cm^{-3} [see the discussion after Eq. (4.2)] yields $\alpha \sim 10^{-14} - 10^{-13}$; significantly lower that the experimentally estimated Hooge parameter values [83].

On the other hand, the case of electron DWP, predicts a much greater Hooge parameter due to a considerably stronger scattering effect by the (2e,2h) pair dipole. In that case

$$\Delta\sigma = \sigma \sim \frac{\pi p}{kT\kappa},$$

where κ is the dielectric permittivity and we used the standard quasi-classical estimate for the dipole interaction radius: $pe/(\kappa r^2) = kT$. As a rough estimate let $p = (1-3) \times 2ae$ [implying intercenter distances of $(1-3)a$] and $\kappa \sim 10$ which yields $\sigma \sim 10^{-11} - 10^{-12}$ cm^2. Combining this with the above estimated $P \sim 10^{17} - 10^{18}$ eV^{-1}cm^{-3} yields $\alpha \sim 10^{-5} - 10^{-2}$, which is in the range of expected values.

A comment is in order regarding the above numerical estimate with $l \sim 100$ Å. That value was chosen to be a lower bound of the mean free path consistent with the Ioffe-Regel criterion of extended (non-localized) states: $l \gtrsim \lambda$ where the DeBroglie wavelength for the charge carriers is $\lambda \sim \hbar/\sqrt{m^* kT} \sim 100$ Å and m^* is the effective mass. If experimental data indicates that l falls below λ (as often happens), then the mechanism of conduction may be more complex than simple band transport. We note, however, that even if we assume $l = 10$ Å, our estimate for the electronic DWP ($\alpha \sim 10^{-7} - 10^{-4}$) still remains in the ballpark of experimentally observed values.

4.3.2 Double Well Potentials: Concentration Modulation Mechanism

Atomic transitions in the double well potentials of chalcogenide glasses can affect the electron energy levels causing changes in their occupation numbers, thereby modulating the charge carrier concentration. Referring to Appendix B.2 for a more rigorous treatment, here we give a semi-quantitative estimate of that effect for the cases of small and large electron energy modulation amplitudes.

4.3.2.1 Small Modulation Amplitude

Consider first the case of relatively small amplitude modulation of the electron energy levels, $\delta E \ll kT$. We start with noting that changes in occupation of localized states near the Fermi level $\delta f \approx (\delta E/kT)f$ dominate the free carrier concentration modulation. The number of such centers is estimated as $N_T = g(E_F)kTV$ where $g(E_F)$ is the density of states at the Fermi level. We assume that each of those states with $f \sim 1/2$ changes its occupation number by $\delta f = (D/kT)\delta n_{DWP}$ where D is the interaction energy of a DWP and a localized electron and δn_{DWP} (of order unity) is the change in the DWP occupation number. As a result the change in the number of free charge carriers per center can be estimated as

$$\delta N_{e1} = \frac{D}{kT}\delta n_{DWP} \exp\left(-\frac{E_F}{kT}\right)$$

where the exponential translates the effect at the Fermi energy states to the mobility edge. To estimate the corresponding dispersion in the frequency interval $\Delta\omega$ we multiply δN_{e1}^2 by the number of DWP ΔN_{DWP} in the volume a^3 of the localized state and the number N_T of such states where ΔN_{DWP} is given in Eq. (4.12), which yields

$$(\Delta N_e)^2 = D^2 P a^3 g(E_F) V \exp\left(-\frac{E_F}{kT}\right)\frac{\Delta\omega}{\omega}.$$

To obtain the relative current dispersion we divide the latter quantity by the square of the average carrier number $VN_{eff}\exp(-E_F/kT)$ where N_{eff} is the effective density of states at the mobility edge. As a result we get

$$\frac{(\Delta j)^2}{j^2} = D^2 P a^3 g(E_F)\frac{\Delta\omega}{\omega V N_{eff}^2}$$

and the corresponding Hooge parameter

$$\alpha = \frac{D^2 P a^3 g(E_F) n_c}{2\pi N_{eff}^2}. \tag{4.14}$$

This result coincides with that of Appendix B.2 to the accuracy of an insignificant numerical factor.

For numerical estimates we assume $D \sim 1$ eV corresponding to the electronic DWP, $a \sim 10$ Å, $n_c \sim 10^{16}$ cm^{-3}, $N_{eff} \sim 10^{18}$ cm^{-3}, $g(E_F) \sim 10^{17} - 10^{18}$ cm^{-3}eV^{-1}, and $P \sim 10^{17} - 10^{18}$ cm^{-3}eV^{-1}, which gives $\alpha \sim 10^{-7} - 10^{-6}$, in the range of known values yet considerably lower than the mobility modulated noise.

On the other hand, for atomic DWP, the estimate in Eq. (4.14) will contain an additional small multiplier reflecting the smallness of the atomic DWP dipole moment. This decreases α below the range of practical interest; hence, atomic DWP do not make any significant contribution in either the mobility or concentration modulation mechanisms of $1/f$ noise.

4.3.2.2 Large Modulation Amplitude

Consider next the opposite limiting case of very large modulation amplitude $\delta E \sim E_F \gg kT$, which may be possible when the electron trap is situated in the nearest proximity of the electronic DWP. The interaction energy $U = 2e^2/\kappa r$ between the trap and the 2e (or 2h) part of the electronic DWP is so large that the DWP and the trap cannot be considered separately, but rather as an "aggregate" in which DWP

transitions are strongly coupled with trapping-detrapping processes. The trap energy is supposed to fall in the nearest proximity of the Fermi level, so that the number of suitable traps is given by the same equation as the above, $N_T = g(E_F)kTV$.

To make the "aggregate" excitation energy low enough ($\lesssim kT$) we assume that the DWP asymmetry is within the interval of kT from the trap energy $E \approx E_F$. Two energy states of such an "aggregate" will then correspond to the following combinations: 1) filled trap + higher energy DWP state; and 2) empty trap + lower energy DWP state. The number of suitable DWP per trap is estimated as

$$\Delta N_{DWP} = PkT\frac{\Delta\omega}{\omega}\left(\frac{2e^2}{E_F\kappa}\right)^3.$$

Dividing the product $N_{DWP}N_T$ by the square of the number of free carriers Vn_c gives the relative dispersion of both the free carrier concentration and the current. The corresponding Hooge parameter becomes

$$\alpha = \frac{g(E_F)P(kT)^2}{n_c}\left(\frac{2e^2}{E_F\kappa}\right)^3. \tag{4.15}$$

Using the above numerical parameters, the preexponential in Eq. (4.15) can be estimated as $10^{-9} - 10^{-7}$. However, the exponential term can be quite substantial, $\exp(E_F/kT) \sim 10^4$ for $E_F = 0.4$ eV at room temperature. As a result, the "aggregate" related Hooge parameter can be comparable with the above estimated α due to the mobility modulated mechanism. A significant difference between the two results is that Eq. (4.15) predicts a decreasing Hooge parameter with increasing charge carrier concentration, while Eq. (4.13) states the opposite. Furthermore, the corresponding temperature dependencies are exponentially different and that may be used for experimental verifications. Also, the non-ohmic behavior turns out to be very different: $(\Delta j)^2/j^2$ is expected to increase or decrease with increasing current in the non-ohmic regime for the cases of Eqs. (4.13) or (4.15), respectively.

4.3.3 Generation-Recombination Noise

We start with the general equation derived in Appendix B.3 and describe generation-recombination noise for the case of a continuous energy spectrum of electronic states in the mobility gap,

$$\frac{\langle (\delta I)^2 \rangle}{I^2} = \frac{4}{n_c^2 V} \int_0^\infty \frac{\tau^2 g(E) dE}{(\tau_e + \tau_c)(1 + \omega^2 \tau^2)}. \tag{4.16}$$

where all the time parameters in the integrand are understood to be functions of energy and the parameters are defined in Appendix B.3. Here τ_e and τ_c stand for the times of escape and capture, and $\tau = (\tau_e^{-1} + \tau_c^{-1})^{-1}$. To the accuracy of model notation, the result in Eq. (4.16) was derived in Ref. [94] in connection with the noise attributed to band tails of doped crystalline semiconductors.

4.3.3.1 Field Effect

Because the data on $1/f$ noise in chalcogenide glasses extends to the region of non-ohmic conduction and correspondingly strong electric fields, our consideration below will be adjusted to account for the field induced effects. To describe the case of strong electric field $\mathcal{E}$ we phenomenologically introduce the enhancement factor $\phi(\mathcal{E})$ which acts to increase the emission rate $\gamma_e \rightarrow \gamma_e \phi(\mathcal{E})$. The underlying mechanism will remove charge carriers from discrete energy levels to the extended states thereby increasing the carrier concentration, $n_c \rightarrow n_c(\mathcal{E})$. Here we use a simple approximation

$$\frac{n_c(\mathcal{E})}{n_c(0)} = \phi(\mathcal{E}) \tag{4.17}$$

neglecting possible effects of the electric field on the capture coefficient γ_c and assuming a slowly varying density of states $g(E)$ in the proximity of the Fermi level. We note that the field function $\phi(\mathcal{E})$ can be exponentially strong. For example, the

hole emission from negatively charged centers is described by the Poole-Frenkel [102] expression with

$$\phi(\mathcal{E}) = \exp(\sqrt{\mathcal{E}/\mathcal{E}_{PF}}), \quad \mathcal{E}_{PF} = (kT)^2\kappa/e^3$$

where κ is the dielectric permittivity. According to other publications, the exponent in $\phi(\mathcal{E})$ is linear in $\mathcal{E}$ (see references in [22]). Here we maintain $\phi(\mathcal{E})$ as an experimentally known parameter related to the carrier concentration according to Eq. (4.17).

It follows from the above that in the presence of the electric field the emission and capture time parameters are related as

$$\frac{\tau_e}{\tau_c} = \frac{n_c\gamma_c}{N_{eff}\gamma_e\phi} = \exp\left(\frac{E - E_F^*}{kT}\right), \tag{4.18}$$

where the quasi-Fermi level is given by

$$E_F^* = E_F + kT\ln[\phi(\mathcal{E})]. \tag{4.19}$$

4.3.3.2 Multi-Phonon Transitions

A detailed discussion of multi-phonon electronic transitions is found in Refs. [22, 95], and [30]. Here we limit ourselves to noting that the dimensionless probability of simultaneously emitting N phonons in the process of capturing a charge carrier at a defect state with energy E in the mobility gap can be estimated as

$$\begin{aligned} p_N &= p_1^N = \exp[-N\ln(1/p_1)] \\ &= \exp[(-E/\hbar\omega_{ph})\ln(1/p_1)] \equiv \exp(E/\varepsilon) \end{aligned} \tag{4.20}$$

where $\hbar\omega_{ph}$ is the characteristic phonon energy (of the order of the Debye energy). The energy parameter ε is typically in the range of $0.01 - 0.03$ eV. Correspondingly,

the time constant for the capture by an empty level can be written in the form

$$\tau_c = \tau_{c0} \exp(E/\varepsilon) \tag{4.21}$$

where $\tau_{c0} = 1/n\sigma v$ and σ is a hypothetical cross-section of capture without the bottleneck of energy exchange. For the often assumed geometrical cross-section $\sigma \sim 10^{-16}$ cm^2 and $n \sim 10^{16}$ cm^{-3}, one can estimate $\tau_{c0} \sim 10^{-7}$ s. The reverse process of emission from a filled level can be strongly facilitated by the external electric field.

4.3.3.3 Density of States Model and Evaluation of Generation-Recombination Noise

Following Ref. [94], we assume a simple density of states model

$$g(E) = g_0 \exp(-E/E_0). \tag{4.22}$$

The characteristic values of E_0 (estimated *e. g.* from the Urbach slope) are typically in the range of 0.03 - 0.1 eV, varying between different amorphous semiconductors [103, 104].

Based on Eqs. (B.49), (4.16), and (4.18), the result in Eq. (4.16) can be presented in the form

$$\frac{\langle (\delta I)^2 \rangle}{I^2} \approx \frac{4}{\omega (n_c \phi)^2 V} \int_0^\infty \frac{(\omega\tau) f(1-f)}{1+(\omega\tau)^2} g dE \tag{4.23}$$

where f is the Fermi distribution. We then discriminate between two conceivable cases, which are different by the condition that the integral in Eq. (4.23) is determined by a narrow region close to the Fermi level where $f \approx 0.5$ or, alternatively, the region of $f \ll 1$ far from the Fermi level.

The former case occurs when kT is the smallest energy scale, $kT \ll E_0, \varepsilon$. For

that case, Eq. (4.23) yields the result

$$\frac{\langle(\delta I)^2\rangle}{I^2} \approx \frac{1}{(n_c\phi)^2 V} g(E_F) kT \frac{\tau_F}{1+(\omega\tau_F)^2} \tag{4.24}$$

with

$$\tau_F = (1/2)\tau_{c0} \exp(E_F^*/\varepsilon), \tag{4.25}$$

which never reduces to the $1/f$ noise.

For the latter case, one can approximate $f = \exp[-|E - E_F|/kT]$ and switch to integration over a new variable $z = \omega\tau$. Assuming $\omega\tau_{c0} \ll 1$ and $\omega\tau_F \gg 1$ evaluation of that integral yields

$$\frac{\langle(\delta I)^2\rangle}{I^2} \approx \frac{4 g_0 kT\varepsilon}{(n_c\phi)^2 V \tau_F^{\nu-1} E_0} \frac{1}{\omega^\nu} \tag{4.26}$$

where

$$\nu = 1 - \frac{\varepsilon}{E_0} - \frac{\varepsilon}{kT}.$$

The result in Eq. (4.26) coincides with that of Ref. [94] to the accuracy of trivial modification $E_F \to E_F^*$ and a multiplier ϕ describing possible effects of nonohmicity. It reduces to the $1/f$ type of spectrum when $\varepsilon \ll kT, E_0$, in which case the Hooge parameter becomes

$$\alpha \approx \frac{2N_{eff}}{\pi n_c \phi} \frac{\varepsilon}{kT} \exp\left(-\frac{E_F}{E_0}\right), \tag{4.27}$$

where we have taken into account that $N_{eff} \approx g_o kT$. Assuming realistic $N_{eff}/n_c \sim 100$, $\varepsilon/kT \sim 0.3$ and $\exp(E/E_0) \sim 10^{-6}$ gives $\alpha \sim 10^{-4}$, in the ballpark of the observed values.

We note, however, that the very possibility of $1/f$ noise here is contingent upon the rather strong assumptions of the inequalities $\omega\tau_{c0} \ll 1$, $\omega\tau_F \gg 1$ and $\varepsilon \ll kT, E_0$ that may not be quite general. For example, the parameters ε, kT, E_0 are comparable

to each other for typical semiconductors and, therefore, the noise spectrum is far from the $1/f$ dependence. Given such degree of uncertainty, it is important to verify the voltage and current dependencies in Eqs. (4.26) and (4.27). Their distinctive feature is that both the relative dispersion $\langle(\delta I)^2\rangle/I^2$ and the Hooge parameter are predicted to decrease with I in the non-ohmic region [as opposed to that due to DWP above]. Indeed, assuming standard transport at the mobility edge, the dc current $I \propto n_c\phi$ appears in the denominators of Eqs. (4.26) and (4.27). Not observing such a decrease in the noise amplitude with increasing current would rule out the generation-recombination mechanism as a possible source of $1/f$ noise.

4.4 Conclusions

We have presented and quantitatively described several conceivable mechanisms of bulk $1/f$ noise in chalcogenide glasses. All of them are related to the presence of random internal degrees of freedom (elemental fluctuators) with exponentially broad distributions of relaxation times, consistent with the existing general understanding of $1/f$ noise. We have related the physical origin of possible fluctuators to the established picture of localized atomic and electronic excitations in chalcogenide glasses. Such fluctuators were attributed to two-state microscopic systems of either atomic (double well potentials, DWP) or electronic nature (pairs of 2e and 2h negative U-centers called electronic DWP throughout this chapter), or strongly coupled aggregates of the latter with the deep electronic traps in the mobility gap. In addition, we have defined the conditions under which generation-recombination processes in the continuous electronic spectrum in the mobility gap can lead to $1/f$ noise. The analytical expressions and numerical estimates for the Hooge parameters for each mechanism are summarized in Table 4.1. Our more specific conclusions are as follows.

1. Atomic DWP that are responsible for low temperature properties of various glasses can generate $1/f$ noise by modulating either the charge carrier mobility or concentration. However, both effects have rather insignificant amplitudes that are well below typically measured values.

2. Electronic DWP can generate $1/f$ noise, most significantly through the mobility modulation leading to realistic Hooge parameters $\alpha \sim 10^{-5} - 10^{-2}$; the corresponding concentration modulating mechanism results in much lower α. In both cases α is proportional to the charge carrier concentration n_c, thus predicting positive non-ohmic and temperature effects.

3. The "aggregate" related Hooge parameter can be in the ballpark of measurable values and is inversely proportional to n_c, thus predicting negative non-ohmic and temperature effects.

4. The necessary condition for the generation-recombination mechanism to cause $1/f$ noise is the multi-phonon nature of the capture time parameter $\tau_c \propto \exp(E/\varepsilon)$ with ε considerably smaller than both kT and the energy scale of the density of state variations. If these conditions are satisfied, the Hooge parameter due to the generation-recombination mechanism of $1/f$ noise may be in the range of the measured values with $\alpha \propto 1/n_c$ leading to negative non-ohmic and temperature effects.

Comparing our results with relevant published data on PCM devices we note that the experimentally estimated Hooge parameter [60] $\alpha \sim 10^{-4}$ is within the domain of our estimates. The observed increase of $\langle(\delta I)^2\rangle/I^2$ with voltage in the non-ohmic region corresponds to our prediction of the electronic DWP modulated mobility and/or concentration. It was also observed that the relative noise in polycrystalline chalcogenides was orders of magnitude lower that that of their glassy counterparts [60]. We note in this connection, that DWP in a polycrystal are limited to the grain

boundary regions and their average density is expected to be much lower than in a glass. In addition, the decrease in the degree of disorder that accompanies the phase transition from glass to polycrystalline results in the suppression of $1/f$ noise.

The experimental results presented in Ref. [60] can be explained by the above theoretical results without invoking an avalanche-like multiplication process. An older publication [61] emphasized a rapid increase in $\langle(\delta I)^2\rangle/I^2$ as the voltage approached the threshold value. That observation is qualitatively consistent with the mechanism of electronic DWP modulated mobility and/or concentration assuming that the concentration strongly increases toward switching.

Overall, we conclude that experimentally studying $1/f$ noise can be a valuable source of information about the electronic and atomic properties of chalcogenide phase change memory as viewed against the background of the above developed theory. In particular, the temperature dependence of $1/f$ noise and its high-field non-ohmic regime can elucidate the underlying mechanisms. Also, we note that since the localized electronic excitations in this or other form seem to underly $1/f$ noise in chalcogenide glasses, crossbreed experiments using well absorbed light to vary the electron occupation of localized energy levels may be of significant interest [93].

Table 4.1: Analytical expressions and numerical estimates for the Hooge parameter corresponding to different conceivable mechanisms of $1/f$ noise in chalcogenide glasses. The expressions are given to within the accuracy of numerical multipliers (found in the text of this chapter). Experimentally estimated values of the Hooge parameter range [83] from 10^{-9} to 10. The meaning of the parameters are as follows: $l \sim 100$ Å is the electron mean free path, $\Delta\sigma \sim 10^{-17}$ cm^2 is the change in the electron scattering cross-section due to the atomic transition in DWP, $n_c \sim 10^{16}$ cm^{-3} is the charge carrier concentration, P is the density of states of DWP estimated as $P \sim 10^{18} - 10^{19}$ for the atomic and $10^{17} - 10^{18}$ eV^{-1}cm^{-3} for the electronic DWP, $D \sim 1$ eV is the interaction potential between the electronic DWP and the trap, $a \sim 10$ Å is the characteristic localization radius of the trap deep in the mobility edge, $N_{eff} \sim 10^{18}$ cm^{-3} is the effective density of states at the mobility edge, $a_0 \sim 1$ Å is the characteristic atomic displacement in DWP, $\kappa \sim 10$ is the dielectric permittivity, $\phi \sim 1 - 1000$ is carrier concentration enhancement factor due to the electric field, $\varepsilon \sim 0.01$ eV is the scale in the exponential energy dependence of the charge carrier trapping time, and E_0 is the energy scale of the band tail decay in the mobility gap.

Mechanism	Equation	Estimate
Atomic DWP, mobility	$(l\Delta\sigma)^2 n_c P k T$	$10^{-14} - 10^{-13}$
Atomic DWP, concentration	$\frac{D^2 P a^3 g(E_F) n_c}{N_{eff}^2} \left(\frac{a_0}{a}\right)^6$	$10^{-13} - 10^{-12}$
Electronic DWP, mobility	$\frac{(ael)^2 n_c P}{\kappa^2 k T}$	$10^{-5} - 10^{-2}$
Electronic DWP, concentration	$\frac{D^2 P a^3 g(E_F) n_c}{N_{eff}^2}$	$10^{-7} - 10^{-6}$
Aggregate, concentration	$\frac{g(E_F) P (kT)^2}{n_c} \left(\frac{e^2}{\kappa E_F}\right)^3$	$10^{-5} - 10^{-3}$
GR concentration	$\frac{N_{eff}}{n_c \phi} \frac{\varepsilon}{kT} \exp\left(-\frac{E_F}{E_0}\right)$	$10^{-6} - 10^{-2}$

Chapter 5

Unified Model of Nucleation Switching

As discussed previously, phase change memory (PCM) devices are based on the phenomenon of switching in chalcogenide glasses [105]; the reversible transition from a high resistance amorphous phase (reset state) to a low resistance crystalline phase (set state) when the device is subject to a threshold voltage (V_{th}) for a duration of time (τ) known as the delay time. Along with PCM, the above cited and subsequent work [5, 106] explored chalcogenide threshold switches (TS) which, in contrast to PCM, require a holding voltage (V_h) to maintain the set state (also known as the on state of TS).

5.1 The Field Induced Nucleation Model

It has long been mainstream understanding that switching is initiated by an electronic filament that can (in PCM) or cannot (in TS) trigger crystal nucleation. However, a recent model [15] described switching in terms of nucleation. Two important insights of the nucleation switching model were the electric polarization of the conductive nucleus and the extension of the free energy to include two degrees of freedom such that a nucleus could evolve in both the radial direction and the height. This extra

freedom allowed nucleation of needle-shaped embryos by surmounting lower energy barriers than spherical embryos. The model predicted several observations [15, 13, 14] including under-threshold switching, the statistics of τ and V_{th}, and relations between V_{th}, device thickness (l), temperature (T), and τ.

Ferroelectric memory also switches by nucleation [107], and it was recently shown that switching in resistive oxides [108] generates conductive filaments consistent with the nucleation mechanism. Driven by these observations, we propose a unified model describing field-induced nucleation switching for arbitrary material parameters including the case where the low resistance phase cannot exist under zero field (in TS). Our model gives closed form expressions for V_{th} and V_h. Also, we present data verifying our understanding.

Our consideration is based on accounting for the lowering of the free energy of the system due to the reduction of the electrostatic energy [109]

$$W_E = -\Omega E_0^2 \epsilon/(8\pi n), \tag{5.1}$$

in the vicinity of the conducting particle, where ϵ is the dielectric permittivity of the host insulating phase, Ω is the volume of the conducting particle, and E_0 is the electric field far from the particle. The depolarizing factor n accounts for the distortion of the electric field due to the geometry of the conducting particle, as illustrated in Fig. 5-1. In a simple approximation [15], the needle-shaped nucleus [Fig. 5-1(a)] of height $h \ll l$ and radius $R \ll h$ can be described as a cylinder with $n \approx (R/h)^2$; a more accurate treatment [13] introduces insignificant numerical factors. Physically, the energy reduction W_E is due to suppression of the electric field in the region of radius h around the nucleus, similar to the lightning rod effect. For a fully grown filament [Fig. 5-1(b)], the free energy reduction is even stronger due to a greater volume in which the filament effectively cancels the electric field.

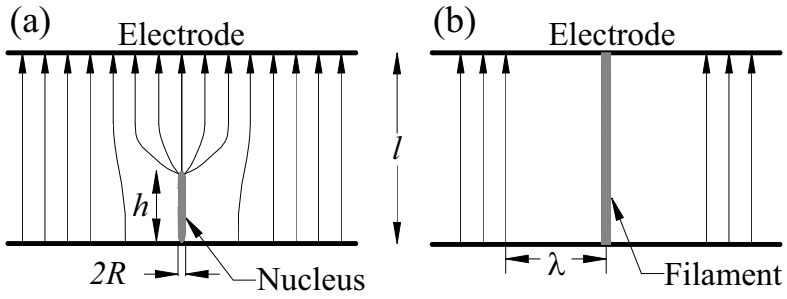

Figure 5-1: The field screening effect for (a) a nucleus of height h and radius R that concentrates the electric field at its tip and weakens it nearby, and (b) a crystalline filament that shorts the electrodes and weakens the field within the screening length λ.

The free energy describing both nucleation and filament stability is given by,

$$F = A\sigma \pm \mu\Omega + W_E \tag{5.2}$$

where A is the surface area of the conducting particle, σ is the surface tension, and μ is the absolute value of the chemical potential difference between the two phases. The positive sign in front of μ refers to TS while a negative sign implies PCM. We make this assertion because it has been observed that reduction of cross-linking elements results in transforming a chalcogenide material from TS to PCM type [105], suggesting that the chemical stability of the amorphous phase versus the crystalline phase determines the device type. Our sign convention accounts for this competition.

5.2 Similarity of PCM and TS

Field-induced nucleation becomes dominant when the third (electrostatic) term in Eq. (5.2) is significantly greater than the second one, making the sign of the second term insignificant. Hence, the nucleation barrier for TS is approximately the same as

for PCM, resulting in the common threshold field [15, 13]

$$E_{th} = \frac{1}{\ln(\tau/\tau_0)} \frac{W_0}{kT} \sqrt{\frac{3\pi^3\alpha^3 W_0}{32\epsilon R_0^3}}, \tag{5.3}$$

where $\tau_0 \sim 10^{-13}$ s is the characteristic vibrational time, and $\alpha \sim 0.1$ is a phenomenological dimensionless parameter that determines the minimum radius $R_{min} = \alpha R_0$ of a mechanically stable conducting cylinder. Here we have expressed E_{th} in terms of the nucleation radius $R_0 = 2\sigma/\mu$ and barrier $W_0 = 16\pi\sigma^3/(3\mu^2)$ for a spherical nucleus under zero field. The similarity of nucleation in TS and PCM is illustrated in Fig. 5-2.

The threshold voltage $V_{th}(l)$ is estimated as a product of E_{th} and the length through which it extends given by the minimum of the amorphous layer thickness l and the bulk electrostatic screening length l_s, i. e.

$$V_{th} = lE_{th} \quad \text{for} \quad l < l_s;\ V_{th} = l_s E_{th} \quad \text{for} \quad l > l_s. \tag{5.4}$$

If we assume the typical charge concentration $N \sim 10^{14} - 10^{16}$ cm^{-3}, dielectric permittivity $\varepsilon \sim 10$, and $V \sim 1$ V, the the screening length [27] $l_s = \sqrt{V\epsilon/2\pi Ne} \sim 0.3 - 3$ μm, and Eq. (5.4) correctly predicts the observed values of V_{th} for not only thin PCM [13, 12], but also for thin [105, 110, 111, 113, 112] and thick [111, 113] TS.

The difference between PCM and TS is in how the free energy changes when the electric field is removed thereby making important the sign of the second term in Eq. (5.2). As Fig. 5-3 indicates, in PCM a nucleus can grow to a size $X > X_0$ that is stable even after the field is removed, while in TS there is no critical size that will allow for a stable crystalline phase without an applied field. This implies the existence of a holding field E_h required to maintain negative free energy.

The holding voltage V_h in TS is related to the minimum electric field $E_h = V_h/l$ required to maintain a non-positive difference between the free energies of the system

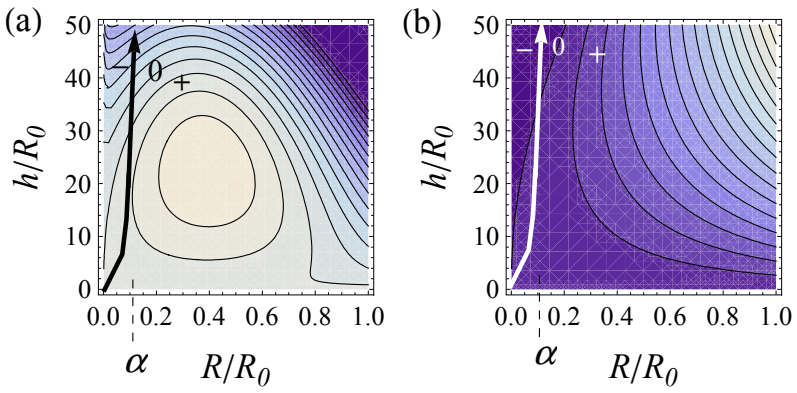

Figure 5-2: Contour maps of the free energy with electric field for (a) PCM and (b) TS. The arrows indicate nucleation paths with the minimum stable radius αR_0. Regions of positive and negative free energy are indicated by + and − separated by the zero contour.

with and without conductive filament, $\Delta F = A\sigma + \mu\Omega + \Delta W_E \leq 0$ where ΔW_E is the difference in the electrostatic energies between the two states. To estimate ΔW_E we note that the electrode resistance is relatively low and the filament accommodates almost the entire voltage drop V_h, most of which occurs through relatively short domains near the electrodes; hence, the electric field $E \ll E_h$ in most of the filament. Such a nonuniform voltage distribution can be attributed to the blocking contacts between the semiconductor filament and the electrodes. Lower dimensionality electrodes [114] (limited to the plane of Fig. 5-1; planar PCM design) can be another cause of field reduction. The assumption of blocking contacts and $E \ll E_h$ was made earlier [5, 106], however the electrostatic consequences of it were not analyzed.

As imposed by the condition of continuity for the tangential (to the filament) component of the field, the low field region $E \ll E_h$ will extend in the lateral directions through certain length λ, over which the field non-uniformity is electrostatically screened; beyond λ the field approaches its saturated value E_h. Because the latter defines the field strength in the system without the filament, one can estimate $\Delta W_E = \epsilon E_h^2 \Omega_E / 8\pi$ where $\Omega_E = \pi l \lambda^2$ is the distorted field volume. For thick ($l \gg l_s$)

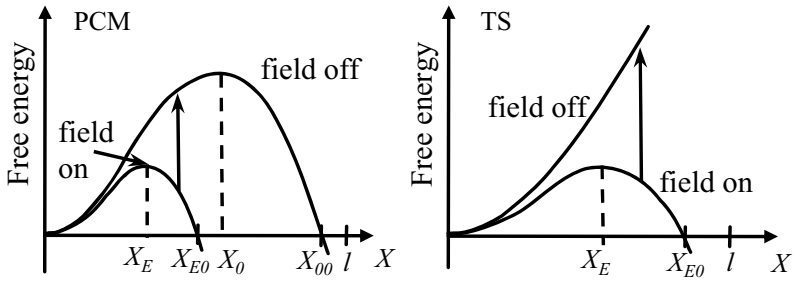

Figure 5-3: Plots of the free energy with and without the electric field where l is the thickness of the amorphous layer; X_E and X_{E0} are the coordinates of maximum and zero free energy with electric field; X_0 and X_{00} are the same without electric field (absent in the case of TS). Both $X_{E0} < X_0$ and $X_{E0} > X_0$ are possible.

devices, we use the earlier mentioned bulk screening length, $\lambda = l_s$. However, for thin devices ($l \ll l_s$), the lateral screening is due to charge redistribution in the metal electrodes [115] and $\lambda \approx l$. Finally, assuming a conductive filament of radius $R = \alpha R_0$ and height $h = l$, the free energy difference for the system with and without filament is given by

$$\Delta F = 2\pi\alpha R_0 l\sigma + \pi\alpha^2 R_0^2 l\mu - \frac{\epsilon E_h^2}{8\pi}\Omega_E, \tag{5.5}$$

where $E_h = V_h/l$. Setting $\Delta F = 0$ yields

$$V_h = \sqrt{\frac{12\alpha W_0}{\epsilon R_0}} \times \{1 \quad \text{for} \quad l < l_s; \frac{l}{l_s} \quad \text{for} \quad l > l_s\}, \tag{5.6}$$

where terms second order in α have been neglected. For a numerical estimate we assume $\alpha \sim 0.1$ and use the typical [116, 117, 118] $W_0 \approx 2$ V, $R_0 \approx 3$ nm, and $\epsilon = 16$, which yields $V_h \sim 1$ V for thin devices. This is on the order of typical measurements of the holding voltage for devices less than 10 μm thick (see Table III in Ref. [119]). Furthermore, Eq. (5.6) indicates thickness dependence that is in accordance with experimental observations [105, 119, 120].

Fig. 5-3 explains how the thickness dependencies $V_{th}(l)$ and $V_h(l)$ are significantly

different. The threshold field E_{th} is related to the barrier height at $X = X_E$ independent of device thickness, leading e.g. to $V_{th} \propto l$. On the other hand, E_h is related to the coordinate X_{E0} where the field bends the free energy curve such that $X_{E0} \leq l$. Therefore, E_h decreases with increasing l [c.f. Eq. (5.6)].

We also note that the condition $X_{E0} = l$ determines the minimum device thickness l for a given field. In both PCM and TS, for switching to occur the electric field must be strong enough to induce negative free energy at a nucleus height that is less than the device thickness, $X_{E0} < l$. Otherwise, if $X_{E0} > l$, a metastable nucleus of height l will disappear causing the system to revert to the lower energy state without the filament. The latter observation implies that, while the concept of holding voltage V_h applies to TS, it also sets a minimum value cut off, $V_{th} \geq V_h$ in PCM.

Another consequence of the field-induced nucleation model is that PCM operates as TS when the field removal (vertical arrows in Fig. 5-3) falls into the region $X_E < X < X_0$, in which case the holding voltage concept applies to PCM as well. Field reduction occurs spontaneously if a just formed filament ($X > X_E$) shorts the device prior to overgrowing the zero-field stability point X_0. This unstable filament rapidly decays thereby restoring the field which then causes regrowth of the filament. This cyclic process leads to oscillations in the device voltage that we identify with the relaxation oscillations in TS [121] and PCM [122].

5.3 Experimental Verification

Our experimental verification utilizes relaxation oscillations in $Ge_2Sb_2Te_5$ (GST) based PCM in lance configuration [12, 123] programmed to the reset state. Devices with GST layers of thicknesses $l = 30$, 70, and 100 nm were studied with trapezoidal read voltages (4 ns/10 μs/4 ns) and various load resistances. Fig. 5-4 shows a domain of typical oscillation data demonstrating V_{th} (maximum voltages) approximately lin-

ear in l. V_h (minimum voltages) was found to be practically independent of l after accounting for the differences in bottom electrode resistances (estimated from device dynamic resistances [124]). These unique observations are consistent with predictions in Eqs. (5.4) and (5.6). Furthermore, using the above numerical parameters Eqs. (5.4) and (5.6) correctly predict $V_{th} \approx 0.2(l/R_0)V_h$ and $V_h \approx 1$ V, consistent with the observed voltages in Fig. 5-4, in particular, $V_h \approx 0.7$ V.

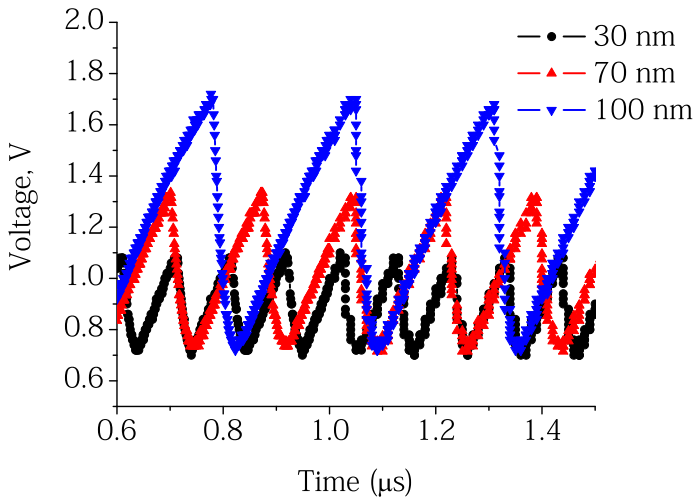

Figure 5-4: Relaxation oscillations in PCM with different thicknesses.

5.4 Conclusion

In conclusion, we have shown that the field-induced nucleation model can provide a common mechanism for switching in arbitrarily thick memory and threshold switches, and possibly some other device types. The model facilitates calculation of the threshold voltage and holding voltage as functions of material parameters and device thickness. The derived equations yield numerical estimates of the appropriate magnitude and include the correct device thickness dependencies as previously reported and as measured in our experiments.

Chapter 6

Relaxation Oscillations in Chalcogenide Phase Change Memory

Relaxation oscillations (RO) are typically observed as oscillations in the device voltage even when the applied bias is constant. The oscillations resemble the charging and relatively fast discharging of a capacitor. The phenomenon occurs when devices that exhibit a negative differential resistance [e.g. threshold switches (TS)] are put under appropriate circuit conditions.

The first systematic experimental measurements of RO in chalcogenide TS were reported by Schmidt and Callarotti [121] for 1 μm-thick films of $Te_{40}As_{35}Ge_7Si_{18}$ subjected to various applied d.c. bias voltages with a range of series load resistances. They found that the period of RO increased linearly with load resistance (R_L) up to a certain point after which the period increased more rapidly than linear until the oscillations ceased at some maximum resistance. Statistical variations in the amplitudes were also observed.

The proposed mechanism of switching in TS implied that, above the threshold voltage V_{th}, a conductive filament formed in the highly resistive amorphous phase. By assuming the amorphous state resistance to be much higher than R_L, a simple

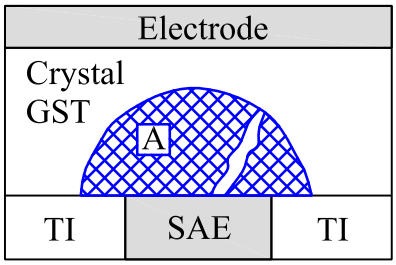

Figure 6-1: Sketch of the switching effect in PCM where the amorphous 'dome', denoted as "A", is created by quenching a portion of the GST that was melted by the heating action of a small area electrode (SAE), surrounded by a thermal insulator (TI), submitted to a strong electric (RESET) pulse. The white strip shows a highly conductive crystalline region that appears as a result of switching.

circuit analysis gave the oscillation period as,

$$T = R_L C \ln \frac{V_a - V_h}{V_a - V_{th}} \tag{6.1}$$

where C is the circuit capacitance, V_a is the applied d.c. voltage, and V_h is the holding voltage. Eq. (6.1) was in good agreement with the R_L-linear portion of their data. Later work [125] showed that consideration of the non-linear amorphous state resistance accounted for the non-linear period. The nature of the conductive filament was beyond the scope of that work; hence, V_{th}, V_h, and the holding current (I_h) remained phenomenological model parameters and were not related to the underlying material properties.

Recently, RO were observed [16, 126, 122] in $Ge_2Sb_2Te_5$ (GST) based PCM devices. At first glance, that observation appears contrary to the common understanding that PCM devices do not have a minimum holding voltage. Nonetheless, it was reported in Ref. [122] that circuit-controlled RO were measured for GST PCM devices under various applied d.c. voltage pulses. The oscillation frequency was found to increase with V_a, however, no connection with quantitative theory was discussed. It was

also observed that V_{th} decayed with time, which was attributed to a decrease in the amorphous dome volume from one cycle to the next (see Fig. 6-1). It was proposed that the degree of amorphization, due to rapid melting and quenching, diminished with each cycle. One problem with that interpretation is that the measured current appears to be insufficient to cause melting.

From a general perspective, the observation of RO in PCM suggests a regime wherein memory devices behave as threshold switches. This region of overlap between PCM and threshold devices formed the basis of a recently proposed [16] unified model for switching in chalcogenide glasses based on electric field-induced crystal nucleation [13, 14, 15], as discussed in Chapter 5. On a practical level, the study of relaxation oscillations can provide insight into the PCM switching mechanism, serve as a diagnostic tool, and instigate an alternative method for measuring material properties.

In this chapter a comprehensive experimental study of RO in GST based PCM is presented. We have extended the previous work by measuring oscillations over much longer periods of time for a broad range of applied voltages and load resistances. Our investigation also included different device thicknesses, the effects of various reset voltage magnitudes, and, briefly, two other types of PCM material. By measuring the oscillation periods, voltage maxima and minima, and calculating current flow with respect to time, we were able distinguish between circuit-dependent and material-dependent parameters, as well as gain some insight into the switching mechanism. In addition, we observed the drift effect during oscillations which lead to an efficient method for measuring the drift coefficient of different materials. A theoretical basis for oscillations is provided in the framework of field-induced crystal nucleation, while the observed decay of oscillation amplitudes is described in terms of concomitant thermally-induced nucleation.

An important general result of this work is that we have obtained additional ev-

idence that switching in PCM is electric field driven. The hypothesis of field driven switching, which was put forward in the original work by Ovshinsky [105], was overshadowed by alternative explanations referring to non-field driven electronic instabilities, as reviewed in Ref. [11]. However, the mechanism of field driven switching was then revived based on both theoretical and experimental evidence [12, 13, 14, 15, 16]. Field-induced switching was experimentally confirmed in recent work [127] (without any reference to the preceding work [12, 13, 14, 15, 16]) with a suggestion that switching can still be explained in the framework of non-field driven mechanisms.

6.1 Experimental Results

Our experiments were designed to investigate how oscillations in PCM are related to circuit and material parameters. Specifically, we sought to understand how the periods, amplitudes, durations, and statistics of the oscillations are related to the applied voltage, the time constants of the circuit, device thickness, and material type.

RO were measured in GST based PCM in lance configuration [12, 123] using the experimental set-up shown schematically in Fig. 6-2(a). Voltage pulses were delivered to the device in series with a load resistor R_L by an HP8110 pulse generator. Input and device voltages were measured with a Tektronix TDS 754 oscilloscope. RO were observed when an appropriate load resistance was placed in the circuit; for our experiments we used R_L = 47, 100, 200, 300, and 600 kΩ. Prior to measurement, samples were reset by first applying a trapezoidal SET pulse followed by a square RESET pulse, as shown in Fig. 6-2(b). Temporal oscillations in voltage across the device V_d were measured during the application of long read pulses, V_a, from 3 to 8 V with leading and trailing edges of 4 ns, and a duration of 10 μs. The time between the reset and read pulses was typically around 10 s. Devices with GST layers of

thicknesses $l = 15$, 30, 70, and 100 nm were studied along with other PCM material types.

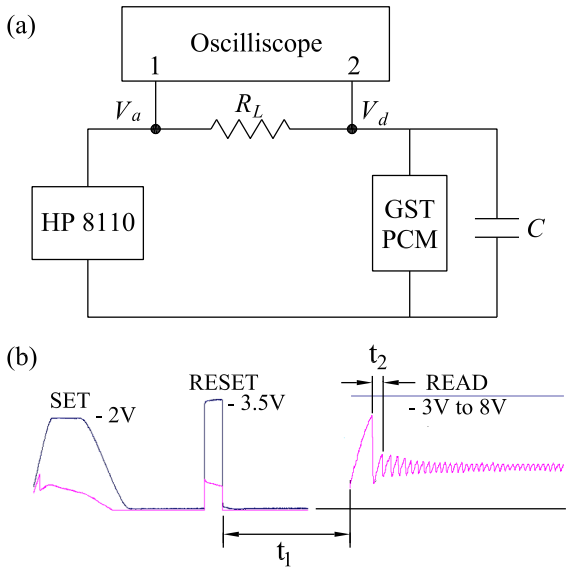

Figure 6-2: (a) schematic of our experimental set-up. (b) the sequence of set, reset, and read voltages along with a sample of the observed oscillations. The time between the reset and read pulses was $t_1 \approx 10$ s and the time between the first and second threshold voltages (V_{th1} and V_{th2}, respectively) was on the order of $t_2 \sim 0.1$ μs. The duration of the read voltage was 10 μs.

We have observed various signal patterns which can be generally described as RO where the number of oscillations was either large ($N \gg 1$) or not very large ($N < 10$), or minimal ($N = 2$), and in some cases no oscillations were observed ($N = 1$), where N is the number of maxima in the device voltage vs. time. In all cases, the second oscillation amplitude (if any) was substantially lower than the first one, while the third and subsequent oscillation amplitudes remained practically equal to each other for a number of periods, after which they decreased (see Fig. 6-3). In what follows we focus on the continuous $N \gg 1$ oscillations, but we will briefly mention the connection between the other RO patterns and our physical model.

The sample of our typical data presented in Fig. 6-3 suggests that the oscillations resemble the periodic charging and relatively rapid discharging of a capacitor. The

charging portion of the cycle followed the typical charging of a capacitor with time constant $\tau_c = R_L C$. At the voltage peak V_{th}, the device switched to a low resistance state ($R_d \ll R_L$) resulting in rapid discharge with time constant $\tau_d = R_d C$ to a point of minimum voltage V_h. At that point, the device snapped back to the high resistance state and the cycle started over. By fitting the rising edge of the first oscillation for various cases we obtained $C \approx 2$ - 10 pF, which yielded an estimate of $R_d \approx 1$ kΩ for the falling edge; consistent with the measured device dynamic resistance value of 1 kΩ [128].

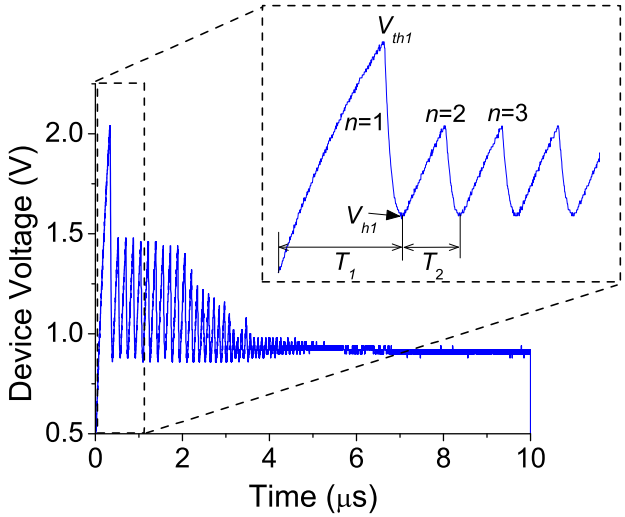

Figure 6-3: A sample of relaxation oscillation measurements for a 70 nm thick device with the voltage across the device V_d recorded at 1 GS/s. The maxima and minima are denoted as V_{th} and V_h, respectively, the first and second periods are T_1 and T_2, respectively. The oscillations are enumerated by n = 1, 2, 3...The inset shows the first four oscillations.

The current through the device as a function of time was calculated using,

$$I_d = \frac{V_a - V_d}{R_L} - C\frac{dV_d}{dt}. \tag{6.2}$$

Our results revealed that the holding current (I_h), corresponding to the time of V_h,

was not the minimum current during a cycle, as shown in Fig. 6-4(a). Furthermore, I_h decreased with increasing R_L while V_h remained almost constant, as shown in Fig. 6-4(b). These results strongly suggest that the low resistance state was sustained not by a characteristic holding current but rather by a sufficient electric field, implying that I_h is a circuit-controlled parameter while V_h is a material property.

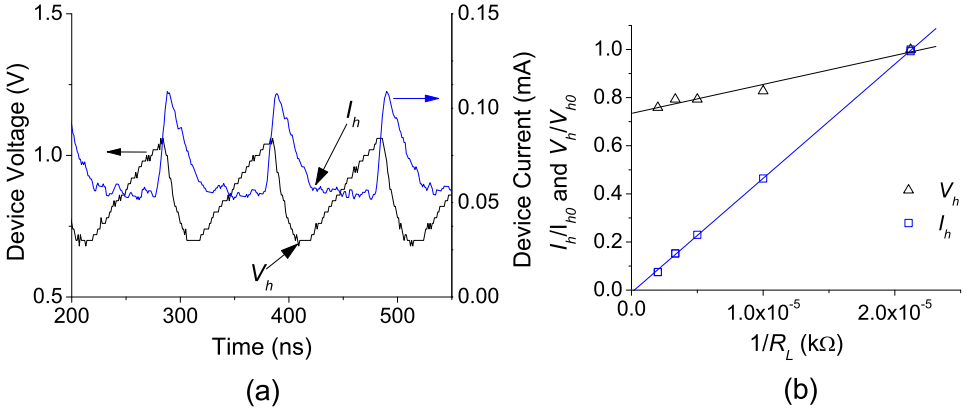

Figure 6-4: (a) device voltage and current showing the holding current I_h, which coincides with the holding voltage V_h; the device current does not significantly change when the device switches to the reset state. (b) holding current I_h and holding voltage V_h, normalized to $I_{h0} = 1.3 \times 10^{-4}$ A and $V_{h0} = 0.58$ V, versus inverse load resistance R_L.

A sample of our measurements for the first period T_1 of oscillation with respect to R_L is in Fig. 6-5. The first period exhibited a linear relationship with R_L, in accordance with Eq. (6.1). Within our range of $R_L < 600$ kΩ, we were unable to reproduce the non-linear dependence and the large statistical spread in periods at high R_L that were reported in Refs. [121] and [125].

We observed that the first maximum threshold voltage V_{th1} did not depend on R_L while the second maximum V_{th2} increased with R_L and the applied bias V_a in such a way that it was linear in $\ln(T)$, where the period $T(R_L, V_a)$ is given by Eq. (6.1). These observations are illustrated collectively in Fig. 6-6 where it is shown that V_{th2} increased with R_L and V_a while scaling logarithmically with the oscillation period

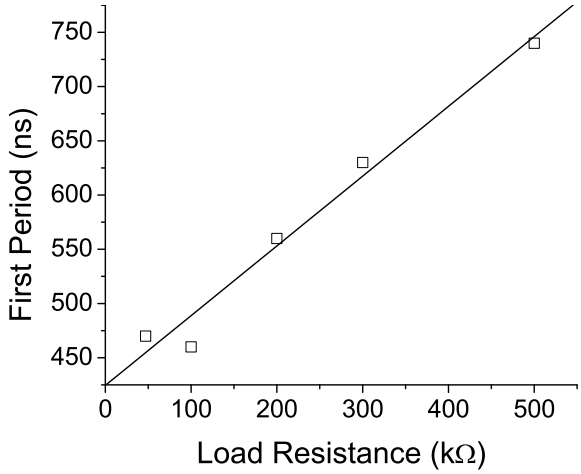

Figure 6-5: First period T_1 of oscillation plotted with respect to load resistance R_L. The applied voltage was $V_a = 3$ V for each case. The linear fit is in agreement with Eq. (6.1).

for one order in time. Our results indicate that the circuitry-dependent oscillation period T depends on R_L and V_a in accordance with Eq. (6.1) while the logarithmic dependence of V_{th} on T is not explained by circuitry analysis and is therefore related to material properties.

Another significant feature of our data was the decay in oscillation amplitudes with time, which displayed a consistent dependence on device thickness. A sample of our data for four different device thicknesses with $V_a = 4$ V is presented in Fig. 6-7 which shows that the oscillations started with a domain of stable amplitudes followed by a domain of diminishing amplitudes. The stable amplitude domain lasted longer for thicker devices, however, the number of stable oscillations decreased with increasing thickness, as illustrated in Fig. 6-8(a). Also, the time for oscillations to completely decay (second time domain) increased with increasing thickness. The length of both time domains were roughly proportional to device thickness.

An important observation related to the data in Fig. 6-7 is the difference in thickness dependencies of the holding (minimum) voltage V_h and the threshold (maximum)

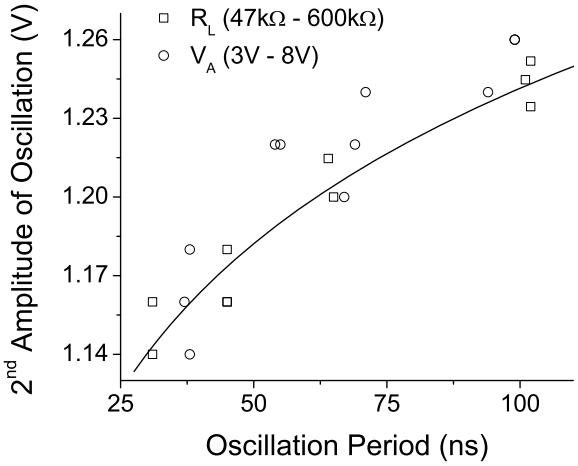

Figure 6-6: The second threshold voltage V_{th2} plotted as a function of oscillation period for various load resistances R_L and applied voltages V_a. The threshold voltage increases with time as shown by the logarithmic fit; an attribute of the drift effect.

voltage V_{th}. Specifically, V_h is thickness independent, while V_{th} is approximately linear in thickness. At this point we use the term 'holding' as an analogy with the case of threshold switches; however, as was pointed out in Ref. [16] and will be explained later in this chapter, the concept of holding voltage can be extended to the case of PCM, making our terminology quite accurate.

We also studied the stability of the oscillations with respect to different reset voltages, which correspond to different amorphous dome volumes [see Fig. 6-1 (b)]. As shown in Fig. 6-8(b), both the duration of stable oscillations and V_{th} increased with increasing reset voltage. A physical basis for the observed stability and decay of the oscillations is described in Sec. 6.3.

6.2 The Drift Effect and Numerical Simulation

The observed logarithmic dependence between threshold voltage and time is indicative of the drift effect [123]. The observation of drift during our experiments is further supported by a consistent feature in all of our measurements which was the

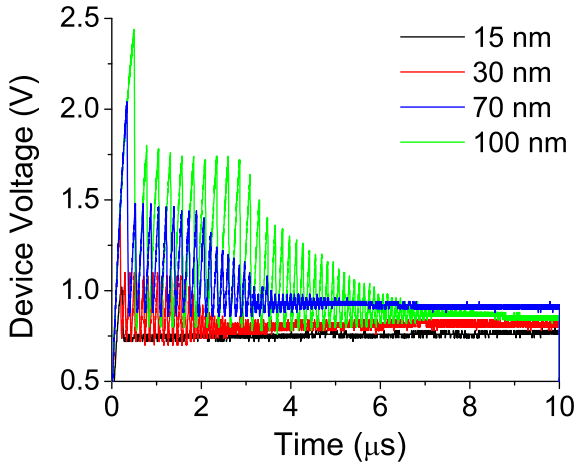

Figure 6-7: Oscillation measurements for four device thicknesses with applied voltage $V_a = 4$ V.

relatively large decrease in V_{th2} relative to V_{th1}; we typically observed $V_{th1} - V_{th2} \sim 0.8$ V. The drift effect asserts that the threshold voltage of a PCM device in the reset state increases with time according to [123],

$$\Delta V_{th} = V_{th}(t_0)\nu \ln\left(\frac{t}{t_0}\right) \tag{6.3}$$

where t_0 is the initial time and ν is the drift coefficient which depends on material properties and temperature. Given that the device remained in the reset state for several seconds ($t_1 \approx 10$ s) prior to application of the read pulse, we expect that V_{th1} should be much greater than V_{th2} since the time between V_{th1} and V_{th2} was on the order of only $t_2 = 100$ ns (refer to Fig. 6-2). With typical numerical values $\nu = 0.025$, $V_{th}(t_0) = V_{th2} = 1.75$ V, $t_1 = 10$ s, and $t_0 = t_2 = 100$ ns, the drift effect predicts $V_{th1} - V_{th2} = 0.8$ V; in good agreement with our experimentally observed 0.75 V for 100 nm thick GST.

We note that a connection between oscillation measurements and drift suggests a method for quantifying the difference in drift coefficients between various materials. To observe this effect we measured oscillations for three different types of PCM mate-

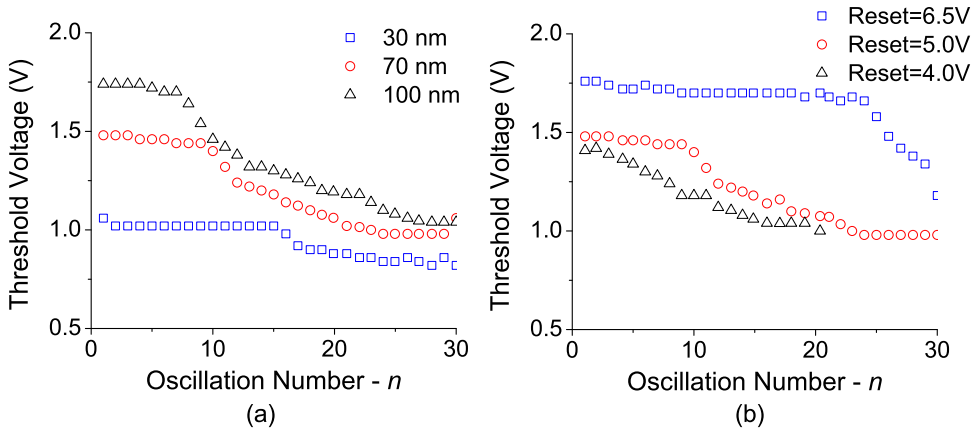

Figure 6-8: The stability of oscillations represented by the threshold voltage V_{th} as a function of oscillation number n for various (a) device thicknesses and (b) reset voltages for a device thickness of 100 nm. There are two regimes; one of stable and one of decaying oscillations.

rials; material (a) was GST, and the other two types are labeled here as (b) and (c). A comparison of the first two peaks yielded the results presented in Table 6.1. The decreasing ratio of V_{th1}/V_{th2} from (a) to (c) clearly indicates that the drift coefficient is greatest in material (a) and smallest in material (c).

Material	$V_{th1} - V_{th2}$	V_{th1}/V_{th2}
(a) - GST	0.85	1.75
(b)	0.50	1.20
(c)	0.15	1.06

Table 6.1: Comparisons of the first and second voltage amplitudes for three different types of PCM material. The results indicate that the drift coefficient decreases from material (a) to (c).

Our numerical calculations incorporate the drift effect in the standard circuitry analysis to simulate RO. By replacing the time parameter in Eq. (6.3) with the oscillation period given by Eq. (6.1), we obtain a means of determining the peak

voltage during the stable portion of the oscillations which is given by,

$$V_{th} = V_{th}(T_0)\left\{1 + \nu \ln\left[\frac{R_L C}{T_0}\ln\left(\frac{V_a - V_h}{V_a - V_{th}}\right)\right]\right\}. \tag{6.4}$$

A numerical parameter set relevant for our experiments is, $V_h = 0.6$ V, $T_0 = 0.1$ ns, and $\nu = 0.05$. One advantage of this numerical scheme is due to the generality of the parameter V_h because it is a material property, rather than a circuit-controlled property, and it is independent of device thickness for the thin devices under consideration.

The rising and falling edge voltages across the device for the stable regime of RO are given, respectively, by

$$V_r = V_a\left(1 - e^{-t/R_L C}\right) \quad \text{and} \quad V_f = V_{th}e^{-t/R_d C}. \tag{6.5}$$

The time at which the rising edge stops and the falling edge begins is determined from Eq. (6.5) by setting $V_r = V_{th}$, where V_{th} is obtained by numerically solving Eq. (6.4). The rising edge proceeds for a time period given by Eq. (6.1) and the falling edge, given by the right expression in Eq. (6.5), decays until the holding voltage is reached. Thus, a complete cycle of oscillations can be simulated. As illustrated in Fig. 6-9, the simulation is in good correspondence with our measurements.

The numerical model allows us to simulate oscillations for low values of circuit time constants that are not typically studied experimentally. We conducted numerous simulations for time constants as low as $\tau = 10$ ns and applied voltages of $V_a = 3$, 5, and 7 V. The results are compiled in Fig. 6-10 which shows that the oscillation periods decreased rapidly with decreasing τ, while the amplitude also decreased but at a slower rate.

We note that our analysis in this section neglected the potential effects of displacement currents related to the localized states in glasses that are often observed

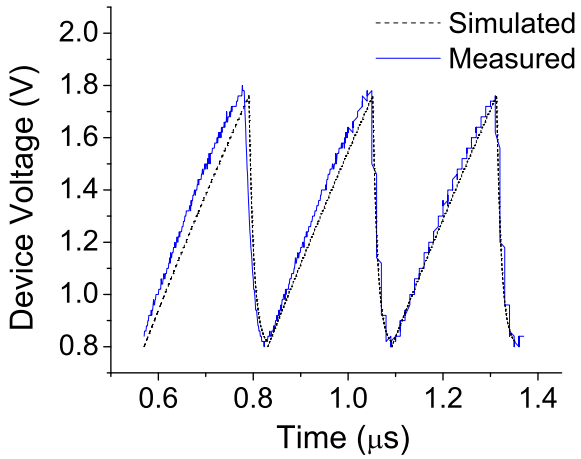

Figure 6-9: A comparison of our numerical simulations and experimental results for relaxation oscillations.

in the mega-hertz frequency region, which corresponds to the oscillation frequency in our work. At this time we have only rough estimates of the neglected effects, which show that they do not qualitatively change our analysis.

6.3 Theory: Crystal Nucleation and Phase Instability

6.3.1 PCM vs. TS: The Nature of RO

The observation of RO in PCM suggests some similarity with TS, where RO was discovered first. We start this section with a brief discussion of conceivable physics behind such similarity. RO are generally attributed to the periodic appearance and disappearance of a conductive filament.

In TS, the existing understanding [5, 119, 120] treats the filament as a purely electronic entity where a high concentration of charge carriers is triggered and maintained by forcing strong enough current. Since the electronic switching is much faster than the circuit *RC* times, the latter determine the period of RO. To the contrary, RO in

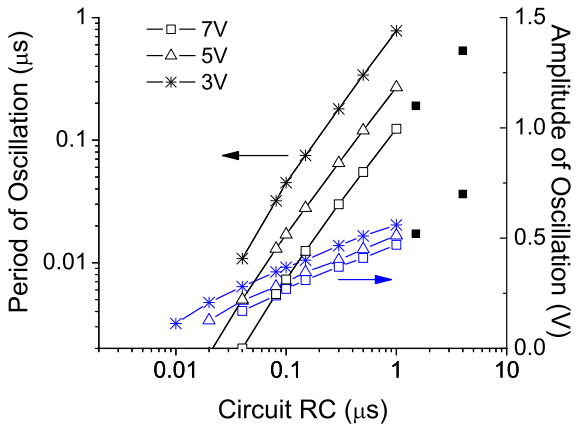

Figure 6-10: A compilation of numerical simulation results showing the calculated periods and amplitudes with respect to the circuit time constant for applied voltages of $V_a = 3$, 5, and 7 V. Experimental data points are represented by solid squares.

PCM were interpreted [122] as a sequence of fast melting and amorphization events during each cycle. The characteristic voltages V_{th} and V_h remained phenomenological parameters, and the collapse in V_{th} was attributed to the decrease in amorphous volume in the course of cycling.

Our interpretation below makes RO in TS and PCM completely identical, attributing the low and high resistance states of these systems to the crystalline and amorphous phases, respectively, without any reference to an electronic filament. According to our model, both TS and PCM systems oscillate between the states with and without a crystalline filament shorting through the structure, as illustrated in Fig. 6-11.

Our physical model is based on the recently developed concept of field-induced nucleation [13, 14, 15], according to which a crystalline filament nucleates and grows in response to a high electric field, as described in Chapter 5. Crystalline filament formation is driven by the reduction of the electrostatic energy that is caused by the shunting action of the filament itself. The distinction between the cases of TS and PCM is that, under zero field, the crystalline filament is thermodynamically unstable

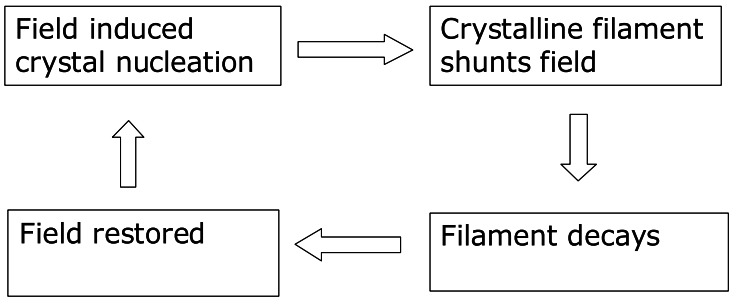

Figure 6-11: Cycle of RO events: the electric field induced nucleation of a crystalline filament shunts the system, which causes field decay. In the absence of the field, the crystalline filament becomes unstable and decays thereby removing the shunt. As a result, the electric field is restored and a new cycle begins.

in TS materials, while it can be stable in PCM materials, as illustrated in Fig. 5-3 which shows the nucleation barriers with an applied electric field (their analytical form [16, 15, 13, 14] is omitted here). In addition, those diagrams represent the free energy in zero field that exhibits the nucleation barrier in the case of PCM, but does not permit nucleation in TS systems.

It is illustrated in Fig. 5-3 how a conducting particle in PCM, once formed ($X > X_E$), will grow until it has achieved a dimension ($X > X_0$) that is stable even after the electric field is removed; however, if the field is removed (vertical arrow in Fig. 5-3) prior to that (i. e. $X_E < X < X_0$) the conductive filament will decay. To the contrary, removal of the field reverts TS to a state wherein the minimum free energy is realized by eliminating the filament at any size X. Therefore, in TS there is no critical size that will allow the device to remain in the set state after the electric field is removed.

For both TS and PCM the electric field must be strong enough to bend the free energy curve such that negative free energy ($X > X_{E0}$) is achieved at a nucleus height less than the device thickness, $X_{E0} < l$. The condition $X_{E0} = l$ determines

the minimum thickness device that can exist in the set state. On the other hand, given l, the same condition determines the minimum voltage V_h, under which the set state can be maintained. While, as such, the concept of holding voltage V_h applies to TS, it also sets a minimum value cut off for V_{th} in PCM. Indeed, if switching to the set state were to occur with $V_{th} < V_h$ (i.e. $X_{E0} > l$), the system would inevitably switch back to the reset state because that would yield the lowest free energy. On a more qualitative level, we point out that the left most parts of the PCM and TS energy diagrams in Fig. 5-3 are similar, which exemplifies the common underlying mechanism of RO in both systems.

We shall end this section with a comment regarding the peculiar relationship between the energies of the crystalline and amorphous phases in TS. In the right (TS) diagram of Fig. 5-3 the ascending dependence of the free energy on the crystal size (correlated with the reaction coordinate) implies that transforming a part of the amorphous material into the crystalline phase *increases* the free energy. At first glance, the latter observation appears contradictory, since it is generally believed that the crystalline structure delivers a minimum to the free energy, decreasing it relative to that of the amorphous phase (as such, crystallization occurs over time under ambient conditions).

We note, however, that the latter inequality between the free energies of crystalline and amorphous phases holds true as long as the crystalline phase can exist for the given chemical composition of a system. In particular, it is well known that not all of the glass forming chemical compositions have their crystalline counterparts (see examples in Ref. [129]). "Crystallizing" such glasses will result in crystals of somewhat different chemical compositions (allowed to have their crystalline counterparts). In the course of such crystallization, the 'excessive' species will be either pushed away beyond the crystal volume (as it takes place in the well known case of ice formation pushing away impurities and rupturing living tissues) or accommodated in the form

of multiple defects, which will significantly increase the system free energy.

Our understanding of the difference between PCM and TS systems does suggest that, unlike PCM, TS structures are formed by chemical compositions that do not have their crystalline counterparts; hence, the free energy increases in the course of crystallization. This understanding is consistent with the observation that reduction in cross-linking elements results in transforming a chalcogenide material from TS to PCM [105], suggesting that the chemical stability of the amorphous phase versus the crystalline phase determines the device type.

6.3.2 Characteristic Voltages: V_h and V_{th}

Using the definition of the holding electric field V_h/l as the minimum electric field required to induce a negative free energy for the system, it was shown in Chapter 5 that

$$V_h = \sqrt{\frac{12\alpha W_0}{\epsilon R_0}} \times \{1 \quad \text{for} \quad l < l_s; \frac{l}{l_s} \quad \text{for} \quad l > l_s\}, \tag{6.6}$$

where $\alpha \sim 0.1$ is the ratio of the filament embryo radius to the classical nucleation radius R_0, W_0 is the classical nucleation barrier, $\epsilon \sim 16$ is the dielectric permittivity, and the electrostatic screening length [27] is

$$l_s = \sqrt{V\epsilon/2\pi Ne} \sim 0.3 - 3\ \mu\text{m}$$

for the typical charge carrier concentrations $N \sim 10^{14} - 10^{16}\text{cm}^{-3}$, $V \sim 1$ V, and where e is the elementary charge.

A comment is in order explaining how our estimate for l_s is by a factor of 10-100 greater than that known from field effect measurements [22]. The discrepancy is due to the fact that here we use the free carrier concentration N while for the case of typical electrostatic screening $N \sim 10^{17} - 10^{18}\text{cm}^{-3}$ represents the total concentration of screening charges, most of which are localized in the vicinity of the Fermi level and

are practically immobile on the time scales ($\lesssim$ 1 ns) of nucleation events [22]; these localized charge carriers simply do not have time to respond to nucleation. Based on the latter estimate, our devices belong to the domain of thin structures ($l < l_s$) where the holding voltage is predicted to be thickness independent, in agreement with the experimental observations above. For a numerical estimate we use the typical [116, 117, 118] $W_0 \approx 2$ V, $R_0 \approx 3$ nm, and $\epsilon = 16$, which yields $V_h \sim 1$V for thin devices; consistent with the observed $V_h \approx 0.5 - 0.7$ V.

Furthermore, as discussed in Chapter 5, the field-induced nucleation model predicts [13, 14, 15, 16] the threshold voltage

$$V_{th} = lE_{th} \quad \text{for} \quad l < l_s; \quad V_{th} = l_s E_{th} \quad \text{for} \quad l > l_s, \tag{6.7}$$

and the threshold field,

$$E_{th} = \frac{1}{\ln(\tau/\tau_0)} \frac{W_0}{kT} \sqrt{\frac{3\pi^3 \alpha^3 W_0}{32\epsilon R_0^3}}, \tag{6.8}$$

where $\tau_0 \sim 10^{-13}$ s is the characteristic vibrational time. Using the above numerical parameters and Eqs. (6.6) - (6.8) yields,

$$V_{th} = 0.2 \frac{l}{R_0} V_h. \tag{6.9}$$

This again is in good agreement with our data.

We conclude that the characteristic voltages V_{th} and V_h are no longer phenomenological parameters and are correctly predicted by our theory. In addition, our approach describes 'thick' ($l > l_s$) devices of older generation, typically $l \gtrsim 1$ μm, where the threshold voltage becomes thickness independent and the holding voltage linearly increases with thickness [105, 110, 111, 112, 113].

6.3.3 Other Features of RO: Long Time Behavior

We now concentrate on the case of PCM and consider a regime of phase change instability, as illustrated in Fig. 6-12. The upper curve in Fig. 6-12 represents the free energy of the GST system with no applied electric field as a function of the crystalline filament radius. The basis of those curves is that given the filament length l, its free energy consists of two terms, one of which is linear in R and accounts for the positive surface energy contribution, while the second term is negative and proportional to R^2, which describes the filament volume and has the proportionality coefficient $\mu + E^2/8\pi\varepsilon$, where E is the electric field strength and μ is the chemical potential. These curves should not be confused with the similar curves in Fig. 5-3. Upon application of a field, the free energy decreases to the lower curve in the figure and a needle-shaped crystalline filament grows along arrow 1. If the filament extends through the thickness l of the GST layer it will shunt the electric field causing the free energy to return to the upper curve along arrow 2. At that point, the crystal phase becomes unstable, likely resulting in the collapse of the filament along arrow 3. Without the filament, the electric field is restored and the free energy decreases again along arrow 4.

We note that when the electric field is shunted along arrow 2 in Fig. 6-12, there is also a possibility [$\propto \exp(-w/kT)$] that the filament will overcome the energy barrier w and evolve into a stable crystal state along arrow 5, leading to termination of the cyclic process. That can account for the occasionally observed small number of oscillations discussed in Sec. 6.1; the average number of such oscillations is given by $\langle N \rangle = \exp(w/kT)$ where k is Boltzmann's constant, T is temperature, and N is supposed to obey the Poisson distribution.

There are two more conditions for oscillation stability: (1) the time $R_{ON}C$ for the nucleus to shunt the field along arrow 2 in Fig. 6-12 must be less than the time t_{ab} for nucleus growth from line (a) to (b), otherwise the filament would become permanent;

and (2) the decay along arrow 3 must cross line (a) before the time $R_{RESET}C$ when the field is restored, where R_{ON} and $R_{RESET} \gg R_{ON}$ are the device resistances corresponding to its high and low resistive states, respectively. Condition (1) suggests that the current through the device must remain low enough to avoid excessive heating that would cause fast filament growth and would violate the inequality $t_{ab} > R_{ON}C$, which is consistent with our observations: forcing too much current through the device resulted in switching without oscillations.

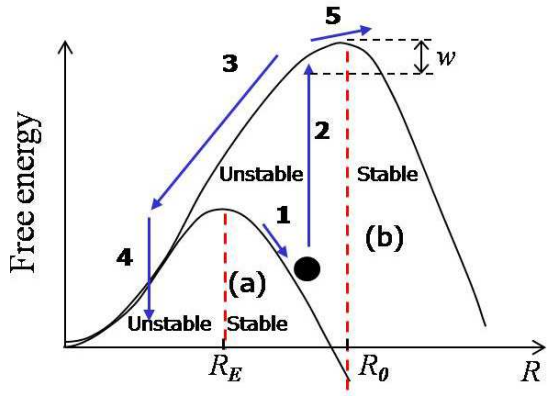

Figure 6-12: The process of and conditions for oscillations in terms of the free energy with respect to the nucleus size R. The lower and upper curves represent the free energy with and without an applied electric field, respectively. The numbered arrows indicate: (1) growth of field-induced crystal nucleus; (2) field shunting; (3) unstable nucleus decay; (4) field restoration; and (5) cycle termination due to activation to a stable nucleus over barrier w.

The discussion thus far has described how the field-induced nucleation model can account for stable oscillation and the stochastic occurrence of oscillations patterns that abruptly terminate. However, our experimental results also exhibited a regime of decaying oscillations (see Fig. 6-8). We propose a physical model of concomitant thermally-induced crystal nucleation which occurs during the course of the oscillations leading to the observed decay of V_{th}.

As illustrated in Fig. 6-13, the oscillations proceed for n_d cycles of the stable regime, all the while heating the amorphous GST region. After n_d cycles, a thermally-

induced spherical crystal nucleus appears, resulting in a lower V_{th}. The spherical nucleus grows and V_{th} continues to decay throughout the decay regime as the oscillation process continues. Oscillations cease when the nucleus is about the size of the GST layer thickness l. It is important to note that the amplitude decay characterizes the material/device rather than the circuit.

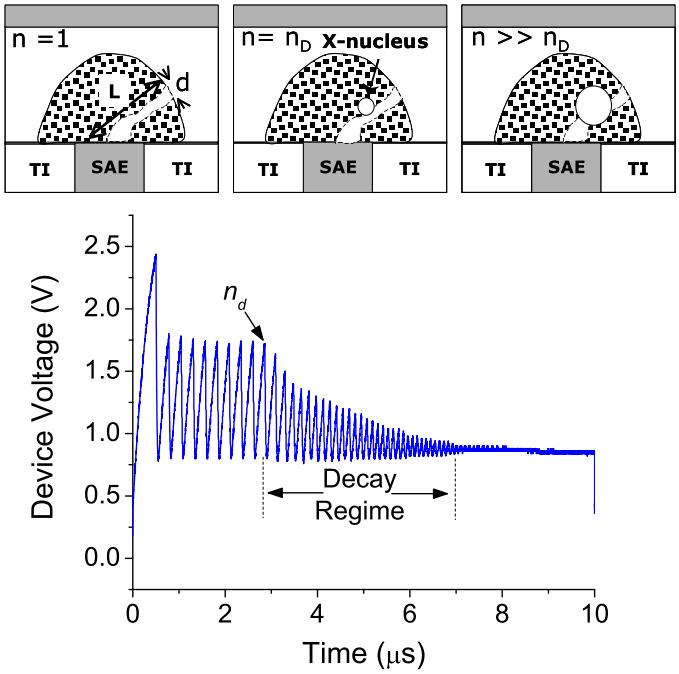

Figure 6-13: The upper figure illustrates the formation of a thermally-induced spherical crystal nucleus at oscillation cycle number n_d. As the oscillations continue, the nucleus continues to grow leading to the decaying amplitudes V_{th} shown in the bottom figure for a device of thickness $l = 100$ nm.

We employ a simplified thermal analysis and standard nuclear growth dynamics to explain the decaying oscillation amplitudes. Our thermal model sketched in Fig. 6-14 has a thin cylindrical heat source, which affects the temperature across a distance $\lambda \propto \sqrt{LL_1}$ dependent on both the poor and good heat conductor thicknesses [130], and corresponds to the heat capacity through $c \propto L\lambda^2 \propto L^2$. The physical origin of temperature increase is related here to the latent heat due to filament crystallization and the Joule heat liberated via the capacitor disharge. Following the approximations

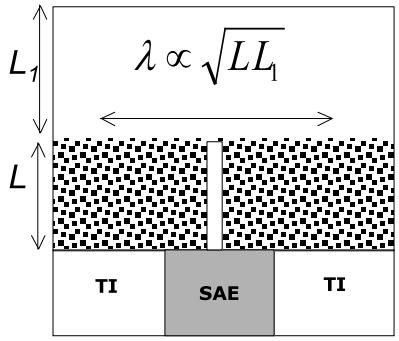

Figure 6-14: Thermal model of amorphous dome of radius L replaced with an amorphous sheet of thickness L in contact with a thermal conductor of thickness L_1 mimicking the polycrystalline GST film.

in Ref. [131], the former can be estimated as $g \sim 300$ Jcm^{-3}. The corresponding effective power $p \sim gLd^2/\Delta t$ where Δt is the oscillation period, is on the order of hundredths of microwatt and is linear in L. The Joule heat is estimated as $QV_h = CV_{th}V_h \propto V_{th} \propto L$, where Q is the electric charge. It scales similarly and can dominate when the discharge is significant. As a result, the time it takes to heat up to a given T scales as $t_s \propto c/p \propto L$. This prediction is consistent with our observed thickness dependence of the time before RO start to collapse.

The above thermal analysis implies that Δt is shorter than the temperature equilibration time t_e so that the temperature does not oscillate with the cycling but, rather, increases over time. t_e is determined by the highest thermal resistance which in the system under consideration is set by the boundary with ambient [132].

To estimate the total decay time t_d, we note that the radius r of a spherical crystal nucleus grows in accordance with,

$$r = a\frac{t}{\tau_0}\exp\left(\frac{-W_{gr}}{kT}\right), \tag{6.10}$$

where a/τ_0 is the material-dependent maximum growth rate and W_{gr} is the barrier to nucleus growth. Given that V_{th} will decay to zero when $2r \approx L$, Eq. (6.10) implies

that $t_d \propto L$. That linear relationship between time of decay and device thickness was observed in our experiments, as shown in Fig. 6-15.

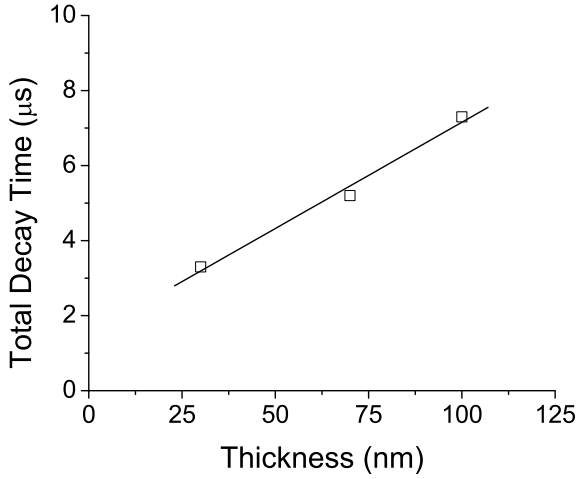

Figure 6-15: Measurements of total oscillation decay time t_d for device thicknesses of 30, 70, and 100 nm. The data exhibits direct proportionality between t_d and thickness, as suggested by the thermally-induced nuclear growth model.

As the threshold voltage decreases, the rate of nucleus growth also decreases with time. Therefore, we set equal the relative rate of amplitude loss per oscillation δV_{th} and the nucleus growth velocity, yielding,

$$\delta V_{th} = \frac{1}{V_{th}} \frac{dV_{th}}{dt} = \frac{1}{L} \frac{dr}{dt} = \frac{a}{L\tau_0} \exp\left(\frac{-W_{gr}}{kT}\right). \tag{6.11}$$

Using $\delta V_{th} \sim 10^5$ s^{-1} from our measurements and $\ln(a/\tau_0) \sim 72$ from the literature [133] we obtain from Eq. (6.11) an estimate of $W_{gr} \sim 2.1$ eV; consistent with other estimates of the activation energy for thermally-induced nucleation in GST [133].

6.4 Conclusions

We have reported the results of our experimental study of relaxation oscillations in GST based PCM, and two other types of PCM material. Measurements were

conducted over long read pulses for a range of applied voltages and load resistances. Several of our key results are listed below.

1. Relaxation oscillations in PCM were observed. While most were continuous, exhibiting 20 to 30 oscillations during the 10 μs read pulse, some displayed only a few cycles and abruptly terminated in a stochastic manner.

2. The holding current decreased with increasing load resistance while the holding voltage remained practically constant indicating that the holding current is a circuit-controlled parameter while the holding voltage is a material characteristic.

3. The holding voltage was found to be independent of device thickness, while the threshold voltage increased linearly with thickness.

4. The period of oscillation was found to be a function of circuit and device parameters with a linear dependence on load resistance.

5. A large difference between the first and second threshold voltages was consistently observed. It was also observed that the second and subsequent threshold voltages depended on load resistance and applied bias while the first threshold voltage did not. These observations were ascribed to the temporal drift effect.

6. Two oscillation regimes were observed; stable amplitudes followed by decaying amplitudes. The duration of stable amplitudes and the time for complete decay were directly proportional to device thickness. The duration of stable amplitudes increased with increasing reset voltage. The rate of amplitude decay characterizes the material rather than the circuit.

7. Our theory, based on the field-induced nucleation concept, explains the absolute values and the thickness dependencies of V_h and V_{th}, the stochastic nature of RO patterns, their decay over time, and the conditions under which RO can exist.

Chapter 7

Summary and Conclusions

A number of theories have been developed and experimental data presented related to non-crystalline semiconductor systems, with thin-film photovoltaics (PV), and chalcogenide glass threshold switches (TS) and phase change memory (PCM) devices as case study systems. In all cases, the underlying mechanisms were based on the disordered nature of these systems with particular attention given to the consequences of localized states and the transition from a disordered to an ordered phase in the presence of a strong electric field. The main conclusions of this work are summarized below. In addition, a comprehensive list of observations and typical parameter values related to TS and PCM has been compiled and included in Appendix A.

A theory of electronic transport in noncrystalline junctions has been developed and compared to the experimental data. Transport is represented as hopping in both real space and energy space, dominated by rare yet exponentially effective optimum channels representing favorable configurations of localized states. The theory correlates current-voltage (IV) characteristics of noncrystalline, thin-film devices with material parameters and predicts large ideality factors that increase under light and depend on applied bias. Also, the frequently observed variations in efficiency and degradation between nominally identical devices are a natural consequence of the theory. The theory was shown to be in good qualitative agreement with measurements extracted from a large set of experimental data on thin-film cadmium telluride/cadmium sul-

fide solar cells. The predictions of voltage-dependent ideality factor and temperature dependent open circuit voltage, V_{oc}, at low temperatures still require experimental verification. An important insight gained by the theory suggests that PV performance can be enhanced by blocking the optimal channels, possibly by using surface treatments.

Consideration of laterally nonuniform current flow allowed for the development of a phenomenological theory of admittance characterization of diode structures with resistive electrodes, including photovoltaic cells and Schottky junctions. The concept of decay length was introduced which describes how far an a.c. signal propagates through the resistive electrode in the lateral direction. According to the theory, the measured capacitance and conductance strongly depend on the decay length and the electrode configuration of the device. Properly arranged admittance circuitry and adequate characterization allow for the detection of shunts (i.e., optimum channels) and their distribution. The method also allows one to determine material parameters, such as, sheet resistance, V_{oc}, ideality factor, and saturation current, in addition to the standard information related to space charge density and defect energy spectra. An significant benefit of this approach is that the diagnostics can be conducted prior to finishing the device (i.e., prior to adding the final conductive layer).

With respect to $1/f$ noise in chalcogenide glasses, several conceivable mechanisms have been expressed in analytical form and quantified with respect to the standard measure of the Hooge parameter. Three possible mechanisms of $1/f$ noise were considered: (1) mobility fluctuations due to transitions in the double-well potentials of the glass; (2) concentration fluctuations due to the same; and (3) generation-recombination noise due to multiphonon electronic transitions in the quasicontinuous spectrum of electronic states in the mobility gap. Double-well potentials were found to be the most likely source of the observed $1/f$ noise. Furthermore, double-well potentials of atomic and electronic nature were discriminated. The latter are related to

the spatially close intimate pairs of oppositely charged negative-U centers and provide a much stronger effect on the $1/f$ noise. In all, six different experimentally testable expressions were developed with varying dependencies on carrier concentration, temperature, and other parameters. Further experimentation at various temperatures and in the non-ohmic bias regime would help to evaluate the derived expressions, as would noise measurements in the presence of well-absorbed light to vary the electron occupation of localized energy levels.

The field-induced nucleation model provides a common mechanism for switching in arbitrarily thick memory and threshold switches, and possibly some other device types. The model facilitates, for the first time, calculation of characteristic voltages as functions of material and circuit parameters. The derived equations yield numerical estimates of the appropriate magnitude and include the correct device thickness dependencies as previously reported and as measured in our own experiments.

A comprehensive experimental study of relaxation oscillations in chalcogenide PCM has been presented. Extending the previous work, voltage and current oscillations were measured over much longer periods of time and with a broad range of applied voltages, load resistances, and device thicknesses. The effects of various reset voltage levels and material types were also considered. Several types of oscillation patterns were observed; most were continuous through the measurement period while others exhibited few or no oscillations. Also observed were two distinct regimes of oscillations; one of stable amplitudes followed by one of decaying amplitudes. The duration of the stable regime and the total time for oscillation decay were found to be directly proportional to the device thickness. In addition, temporal drift of the threshold voltage was observed which provided a method for measuring the variation in the drift coefficient between different materials. A numerical model was developed to simulate oscillations and extrapolate the results to lower circuit time constants. The physical mechanism of oscillations and their stochastic nature were effectively de-

scribed in the framework of field-induced nucleation, while the transition from stable to decaying amplitudes was attributed to concomitant thermally induced nucleation.

References

[1] A. F. Fahrenbruch, *Fundamental of Solar Cells* (Academic Press, 1983).

[2] W. Shockley and W. T. Read, Phys. Rev. **87**, 835 (1952).

[3] C. T. Sah, R. N. Noyce, and W. Shockley, Proc. IRE **45**, 1288 (1957).

[4] M. Nardone, V. G. Karpov, D. Shvydka, and M. L. C. Attygalle, J. Appl. Phys. **106**, 074503 (2009).

[5] D. Adler, H. Henisch, and N. Mott, Rev. Modern Phys. **50**, 209 (1978).

[6] D. Adler, M. S. Shur, M. Silver, and S. R. Ovshinsky, J. Appl. Phys. **51**, 3289 (1980).

[7] H. K. Henisch, E. A. Fagen, and S. R. Ovshinsky, J. Non-Cryst. Solids **4**, 538 (1970).

[8] I. Lucas, J. Non-Cryst. Solids **6**, 136 (1971).

[9] N. Mott, Contemp. Phys. **10**, 125 (1969).

[10] K. E. Petersen and D. Adler, J. Appl. Phys. **50**, 925 (1979).

[11] A. Redaelli, A. Pirovano, A. Benvenuti, and A. L. Lacaita, J. Appl. Phys. **103**, 111101 (2008).

[12] V. G. Karpov, Y. A. Kryukov, S. D. Savransky, and I. V. Karpov, Appl. Phys. Lett. **90**, 123504 (2007).

[13] V. G. Karpov, Y. A. Kryukov, I. V. Karpov, and M. Mitra, Phys. Rev. B **78**, 052201 (2008).

[14] V. G. Karpov, Y. A. Kryukov, M. Mitra, and I. V. Karpov, J. Appl. Phys. **104**, 054507 (2008).

[15] I. V. Karpov, M. Mitra, D. Kau, G. Spadini, Y. A. Kryukov, and V. G. Karpov, Appl. Phys. Lett. **92**, 173501 (2008).

[16] M. Nardone, V. G. Karpov, D. C. S. Jackson, and I. V. Karpov, Appl. Phys. Lett. **94**, 103509 (2009).

[17] M. Nardone, V. G. Karpov, and I. V. Karpov, J. Appl. Phys. **107**, 054519 (2010).

[18] J. D. Cohen, *Semiconductors and Semimetals* **21**, Part C, edited by J. I. Pankove, 9 (1984).

[19] V. G. Karpov, D. Shvydka, U. Jayamaha and A. D. Compaan, J. Appl. Phys. **94**, 5809 (2003).

[20] T. Walter, R. Herberholz, C. Muller, and H. W. Schock, J. Appl. Phys. **80**, 4411 (1996).

[21] S. Lai, IEDM 2003 Technical Digest. IEEE International, p. 10.1.1 (2003); G. Atwood and R. Bez, Device Research Conference Digest **63**, 29 (2005); A. Pirovano, A.L. Lacaita, A. Benvenuti, F. Pellizzer, R. Bez, IEEE Trans. Electron. Devices **51**, 452 (2004); A.L. Lacaita, Solid State Electron. **50**, 24 (2006).

[22] N. F. Mott and E. A. Davis, *Electronic Processes in Non-crystalline Materials* (Clarendon Press, Oxford, 1979).

[23] M. Pollack and J. J. Hauser, Phys. Rev. Lett. **31**, 21 (1973).

[24] M. E. Raikh and I. M. Ruzin, in *Mesoscopic Phenomena in Solids*, edited by B. L. Altshuller, P. A. Lee, and R. A. Webb (Elsevier, 1991), p. 315.

[25] A. L. Efros and B. I. Shklovskii, *Electronic Properties of Doped Semiconductors* (Springer-Verlag, Berlin, 1992).

[26] B. I. Shklovskii, Pis'ma Zh. Eksp. Teor. Fiz. **44**, 95 (1986) [Sov. Phys. JETP Lett. **44**, 121 (1986)]; S.D. Baranovskii, V. G. Karpov, B. I. Shklovskii, Zh. Eksper. Teor. Fiz. **94**, 278 (1988) [Sov. Phys. JETP **67**, 588 (1988)].

[27] S. M. Sze, *Physics of Semiconductor Devices* (Willey & Sons, New York, 1981).

[28] U. Rau, Appl. Phys. Lett. **74**, 1 (1999); U. Rau, A. Jensek, H. W. Schock, F. Englehardt, and Th. Meyer, Thin Solid Films **361-362** (2000).

[29] F. A. Padovani and R. Stratton, Solid State Electron. **9**, 695 (1966).

[30] V. N. Abakumov, V. Perel, and I. Yassievich, *Nonradiative Recombination in Semiconductors* (North-Holland, Amsterdam, 1991), [Modern Problems in Condensed Matter Science, V. 33].

[31] E. I. Levin, I. M. Ruzin, and B. I. Shklovskii, Fiz. Tekh. Poluprovodn. **22**, 642 (1988) [Sov. Phys. Semicon. **22**, 4 (1988)].

[32] V. G. Karpov, D. Shvydka, and Y. Roussillon in *Proceedings of 31st IEEE Photovoltaic Specialists Conference*, Orlando (IEEE, New York, 2005), p. 437.

[33] V. G. Karpov, A. D. Compaan, and D. Shvydka, Phys. Rev. B **69**, 045325 (2004).

[34] M. Mitra, J. Drayton, M. L. C. Cooray, V. G. Karpov, and D. Shvydka, J. Appl. Phys. **102**, 034505 (2007).

[35] D. Shvydka, J. Drayton, A. D. Compaan, and V. G. Karpov, Appl. Phys. Lett. **87**, 123505(2005).

[36] Y. Roussillon, V. G. Karpov, D. Shvydka, J. Drayton, and A. D. Compaan, J. Appl. Phys. **96**, 7283 (2004).

[37] Y. Roussillon, D. Giolando, D. Shvydka, A. D. Compaan, and V. G. Karpov, Appl. Phys. Lett. **85**, 3617 (2004).

[38] Y. Roussillon, D. Giolando, D. Shvydka, A. D. Compaan, and V. G. Karpov, Appl. Phys. Lett. **84**, 616, (2004).

[39] D. Shvydka, C. Verzella, V. G. Karpov and A. D. Compaan, J. Appl. Phys. **94**, 3901 (2003).

[40] D. Shvydka, V. G. Karpov and A. D. Compaan, Appl. Phys. Lett. **82**, 2157 (2003).

[41] D. Shvydka, A. D. Compaan, and V. G. Karpov, J. Appl. Phys. **91**, 9059 (2002).

[42] V. G. Karpov, A. D. Compaan, and D. Shvydka, Appl. Phys. Lett. **80**, 4256 (2002).

[43] M. L. C. Cooray and V. G. Karpov, Appl. Phys. Lett. **88** 093508 (2005).

[44] V. G. Karpov and D. Shvydka, Phys. Status Solidi (Rapid Research Letters) **1**, 132 (2007).

[45] B. E. McCandless and J. R. Sites, in *Handbook of Photovoltaic Science and Engineering*, edited by A. Lique and S. Hegedus (Wiley, New Jersey, 2003), p. 617.

[46] D. Rose, R. Powell, U. Jayamaha, M. Maltby, in *Proceedings of the 29th IEEE Photovoltaic Specialists Conference*, New Orleans (IEEE, New York, 2002), p. 555.

[47] D. K. Schroder, *Semiconductor Material and Device Characterization*, John Wiley, 1998.

[48] P. Blood and J. W. Orton, *The electrical characterization of semiconductors: majority carriers and electron states*, Academic Press, NY 1992.

[49] I. G. Gibb and A. R. Long, Phil. Mag. B **49**, 565 (1984).

[50] F. H. Seymour , V. Kaydanov, T. R. Ohno J. Appl. Phys. **100**, 033710 (2006).

[51] Y. Y. Proskuryakov, J. D. Major, K. Durose, V. Barrioz, S. J. C. Irvine, E. W. Jones, D. Lamb, Appl. Phys. Lett **91**, 153505 (2007).

[52] D. Shvydka, A. D. Compaan and V. G. Karpov, J. Appl. Phys. **91**, 9059 (2002).

[53] V. G. Karpov, G. Rich, A. V. Subashiev, G. Dorer, J. Appl. Phys. **89**, 4975 (2001).

[54] C. Christopolous, *The transmission Line Modeling Methods*, IEEE, New York, (1995).

[55] L. D. Landau and E. M. Lifshitz, *Quantum Mechanics, Non-Relativistic Theory, Volume 3* (Elsevier, Oxford, 1977).

[56] *Handbook of Photovoltaic Science and Engineering*, Edited by A. Lique and S. Hegedus, Wiley, Chichester (2003).

[57] V. I. Yudson, M. G. Rozman, P. Reinker, Phys. Rev. B **55**, 5514 (1997).

[58] D. Ielmini, Phys. Rev. B **78**, 03538 (2008).

[59] A. L. Lacaita, D. Ielminia and D. Mantegazza, Solid State Electron. **52**, 1443 (2008); A. L. Lacaita, and D. Ielmini, in *Proceedings of the Solid State Device Research Conference. ESSDERC 2007. 37th European, Munich, 2007* (IEEE, 2007), p. 214.

[60] P. Fantini, A. Pirovano, D. Ventrice, and A. Redaelli, Appl. Phys. Lett. **88**, 263506 (2006).

[61] W. R. Smith, R. F. Shaw, H. K. Henicsh, Electrocomponent Science and Technology **1**, 137 (1973).

[62] C. Main and A. E. Owen, Phys. Stat. Sol. (a) **1**, 297 (1970).

[63] K. N. Scharnhorst, J. Non-Cryst. Solids **23**, 435 (1977).

[64] C. E. Parman, J. Kakalios, Phys. Rev. Lett. **67**, 2529 (1991); C. Parman, N. E. Israeloff, and J. Kakalios, Phys. Rev. B **47**, 12578 (1993); G. Snyder, M. B. Weissman, H. T. Hardner, and C. Parman, Phys. Rev. B **56**, 9205 (1997).

[65] S. D. Baranovskii and V. G. Karpov, Fiz. Tech. Poluprov. **21**, 3 (1987) [Sov. Phys. Semiconductors **21**, 1 (1987)].

[66] S. D. Baranovskii and V. G. Karpov, Fiz. Tech. Poluprov. **21**, 314 (1987) [Sov. Phys. Semiconductors **21**, 189 (1987)].

[67] S. Hunklinger and W. Arnold, in *Physical Acoustics*, edited by W. P. Mason and R. N. Thurston (New York, Academic Press, 1976), Vol. XII, p. 155.

[68] W. A. Phillips, Rep. Progr. Phys. **50**, (1987).

[69] Yu. M. Galperin, V. G. Karpov, and V. I. Kozub, Adv. Phys. **38**, 669 (1989).

[70] I. V. Karpov, M. Mitra, D. Kau, G. Spadini, Y. A. Kryukov,and V. G. Karpov. J. Appl. Phys. **102**, 124503 (2007).

[71] P. W. Anderson, B. I. Halperin, and C. M. Varma, Phil. Mag. **25**, 1 (1972).

[72] W. A. Phillips, J. Low Temp. Phys. **7**, 351 (1972).

[73] V. G. Karpov, M. I. Klinger, and F. N. Ignatiev, Zh. Eksp. Teor. Fiz. **84**, 761 (1983) [Sov. Phys. JETP **57**, 439 (1983)].

[74] D. A. Parshin, Sov. Phys. Solid. State **36**, 991 (1994); D. A. Parshin, Phys. Scr. **T49A**, 180 (1993); D. A. Parshin, H. R. Schober, and V. L. Gurevich, Phys. Rev. B **76**, 064206 (2007); B. Ruffle, D. A. Parshin, E. Courtens, and R. Vacher, Phys. Rev. Lett. **100**, 015501 (2008).

[75] M. I. Klinger and V. G. Karpov, Zh. Eksper. Teor. Fiz. **82**, 1687 (1982) [Sov. Phys. JETP **55**, 976 (1982)]; V. G. Karpov, Zh. Eksper. Teor. Fiz. **85**, 1017 (1983) [Sov. Phys. JETP **58**, 592 (1983)].

[76] P. W. Anderson, Phys. Rev. Lett. **34**, 952 (1975).

[77] R. A. Street and N. F. Mott. Phys. Rev. Lett. **35**, 1293 (1975).

[78] M. Kastner, D. Adler, and H. Fritzsche, Phys. Rev. Lett. **37**, 1504 (1976); M. Kastner and H. Fritzsche, Phil. Mag. **37**, 199 (1978).

[79] W. A. Phillips, Phil. Mag. **34**, 983 (1976).

[80] V. G. Karpov, Fiz. Tekh. Poluprovdn. **19**, 123 (1984) [Sov. Phys. Semiconductors **19**, 74 (1984)].

[81] A. R. Long. Adv. Phys. **31**, 553 (1982).

[82] Aldert van der Ziel. *Noise: Sources, Characterization, Measurement* (Prentice-Hall, 1970).

[83] S. M. Kogan, *Electronic noise and fluctuations in solids* (Cambridge University Press, 1996).

[84] J. Bernamont, Ann. Phys. (Leipzig) **7**, 71 (1937).

[85] A. L. McWhorter, *Semiconductor surface physics* (University of Pennsylvania Press, Philadelphia, 1957).

[86] K. K. Hong, P. K. Ko, C. Hu, Y. C, Cheng, IEEE Trans. Electron. Devices **37**, 654 (1990).

[87] S. M. Kogan and K. E. Nagaev, Sol. State Commun. **49**, 387 (1984); A. Ludviksson, R. Kree, and A. Schmid, Phys. Rev. Lett. **52**, 950 (1984).

[88] V. I. Kozub, Sov. Phys. JETP **59**, 1303 (1984); Sov. Phys. Solid State **26**, 1186 (1984); Y. M. Galperin, V. G. Karpov, and V. I. Kozub, Sov. Phys. JETP **68**, 648 - 653 (1989).

[89] A. L. Efros and B. I. Shklovskii, *Electronic Properties of Doped Semiconductors* (Elsevier, Amsterdam, 1985).

[90] V. I. Kozub, Solid State Commun. **97**, 843-846 (1996).

[91] B. I. Shklovskii, Phys. Rev. B **67**, 045201 (2003).

[92] A. L. Burin, B. I. Shklovskii, V. I. Kozub, Y. M. Galperin, and V. Vinokur, Phys. Rev. B **74**, 075205 (2006).

[93] M. E. Levinshtein, Physica Scripta. **T69**, 79-84, (1997).

[94] N. V. Dyakonova and M. E. Levinshtein, Sov. Phys. Semicond. **23**, 175 (1989).

[95] A. M. Stoneham, *Defects in Solids* (Oxford, University Press, London, 1975).

[96] S. D. Baranovskii and V. G. Karpov, Fiz. Tech. Poluprov. **19**, 541 (1985) [Sov. Phys. Semiconductors **19**, 336 (1985)]; *ibid.* **20**, 309 (1986) [Sov. Phys. Semiconductors **20**, 192 (1986)]; *ibid.* **18**, 1324 (1984) [Sov. Phys. Semiconductors **18**, 828, (1984)]; *ibid.* Fiz. Tech. Poluprov. **21**, 2109 (1987) [Sov. Phys. Semiconductors **21**, 1280 (1987)]; S. D. Baranovskii, V. G. Karpov, and B. I. Shklovskii,

Zh. Eksper. Teor. Fiz. **94**, 278 (1988) [Sov. Phys. JETP **67**,588 (1988)]; S. D. Baranovskii and V. G. Karpov, Fiz. Tech. Poluprov. **20**, 1811 (1986) [Sov. Phys. Semiconductors **20**, 1137 (1986)]; J. Fortner, V. G. Karpov, and M. L. Saboungi, Appl. Phys. Lett. **6**, 997 (1995).

[97] A. van der Ziel. *Noise in Measurements* (Wiley, New York, 1976).

[98] A. M. Zaklikiewicz, Solid State Electron. **43**, 11 (1999).

[99] F. N. Hooge, T. G. M. Kleinpenning, and L. K. J. Vandamme, Rep. Progr. Phys. **44**, 31 (1981).

[100] T. G. M. Kleinpenning and L. K. J. Vandamme, J. Appl. Phys. **52**, 1594 (1981).

[101] M. B. Weissman, Rev. Modern Phys. **60**, 537 (1988).

[102] J. Frenkel, Phys. Rev. **54**, 657 (1938); R. M. Hill, Phil. Mag. **23**, 59 (1971).

[103] T. Kato and K. Tanaka, Japan. J. Appl. Phys. **44**, 7340 (2005);

[104] B. S. Lee, J. R. Abelson, S. G. Bishop, D. H. Kang, B. K. Cheong, and K. B. Kim, J. Appl. Phys. **97**, 93509 (2005).

[105] S. R. Ovshinsky, Phys. Rev. Lett. **21**, 1450 (1968).

[106] H. Fritzsche, in *Amorphous and Liquid Semiconductors*, Ed. by J. Tauc, (Plenum Press, London-New York, 1974), p. 313.

[107] S. Jesse, B. Rodrigues, S. Choudury, A. P. Baddorf, I. Vrejoiu, D. Hesse, M. Lexe, E. A. Eliseev, A. N.Morozovska, J. Zhang, L.-Q. Chen, and S. V. Kalinin, Nature Materials **7**, 209 (2008).

[108] J. H. Son and W. -H. Shin, Appl. Phys. Lett. **92**, 22106 (2008).

[109] L. D. Landau and E. M. Lifshitz, *Electrodynamics of Continuous Media* (Pergamon, New York, 1984).

[110] P. J. Walsh, R. Vogel, and E. J. Evans, Phys. Rev. **178**, 1274 (1969).

[111] B. H. Kolomiets, E. A. Lebedev, and E. A. Taksami, Sov. Phys. Semiconductors **3**, 267 (1969).

[112] H. K. Henisch and W. R. Smith, Appl. Phys. Lett. **24**, 589 (1974).

[113] H. J. Stocker, C. A. Barlow Jr., and D. F. Weirauch, J. Non-Cryst. Solids **4**, 523 (1970).

[114] H. Ruda and A. Shik, J. Appl. Phys. **86**, 5103 (1999); Physica E **6**, 543 (2000).

[115] V. G. Karpov, M. L. C. Cooray, and D. Shvydka, Appl. Phys. Lett. **89**, 163518 (2006); M. L. C. Cooray and V. G. Karpov, Phys. Rev. B. **75**, 155303 (2007).

[116] M. C. Weinberg and G. F. Nelson, J. Non-Cryst. Solids **74**, 177 (1985).

[117] C. Barrett, W. Nix, and A. Tetelmam, *The Principles of Engineering Materials* (Prentice-Hall, Englewood Cliffs, NJ, 1973).

[118] X. S. Miao, L. P. Shi, H. K. Lee, J. M. Li, R. Zhao, P. K. Tan, K. G. Lim, H. X. Yang, and T. C. Chong, Jpn. J. Appl. Phys., Part 1 **45**, 3955 (2006).

[119] A. E. Owen and J. M. Robertson, IEEE Trans. Electron Devices **ED-20**, 105 (1973).

[120] A. C. Warren, IEEE Trans. Electron Devices **ED-20**, 123 (1973).

[121] P. E. Schmidt and R. C. Callarotti, Thin Solid Films **42**, 277 (1977).

[122] D. Ielmini, D. Mantegazza, and A. L. Lacaita, IEEE Electron. Device. Letters **29**, 568 (2007).

[123] I. V. Karpov, M. Mitra, D. Kau, G. Spadini, Y. A. Kryukov, and V. G. Karpov. J. Appl. Phys. **102**, 124503 (2007).

[124] I. V. Karpov and S. A. Kostylev, IEEE Electron Device Lett. **27**, 808 (2006).

[125] P. E. Schmidt and R. C. Callarotti, J. Appl. Phys. **55**, 8 (1984).

[126] P. Zhou, Y. C. Shin, B. J. Choi, S. Choi, C. S. Hwang, Y. Y. Lin, H. B. Lv, X. J. Yan, T. A. Tang, L. Y. Chen, and B. M. Chen, Electrochem. Solid-State Lett. **10**, H281 (2007).

[127] D. Krebs, S. Raoux, C. T. Rettner, G. W. Burr, M. Salinga, and M. Wuttig, Appl. Phys. Lett. **95**, 082101 (2009).

[128] I. V. Karpov and S. A. Kostylev, IEEE Electron Device Lett. **27**, 808 (2006).

[129] D. I. Bletskan, Chalcogenide Letters **3**, 81 (2006).

[130] D. Shvydka, C. Verzella, V. G. Karpov, and A. D. Compaan, J. Appl. Phys. **94**, 3901 (2003).

[131] S. Senkader and C. D. Wright, J. Appl. Phys. **95**, 504 (2004).

[132] K. Sonoda, A. Sakai, M. Moniwa, K. Ishikawa, O. Tsuchiya, and Y. Inoue, IEEE Trans. Electron Devices **55**, 1672 (2008).

[133] J. Kalb, F. Spaepen, and M. Wuttig, Appl. Phys. Lett. **84** 25, 5240 (2004).

[134] P. J. Walsh, J. E. Hall, R. Nicolaides, S. Defeo, P. Callela, J. Kuchmas, and W. Doremus, J. of Non-Cryst. Solids **2**, 107 (1970).

[135] N. Croitoru, L. Vescan, C. Popescu, and M. Lazarescu, J. Non-Cryst. Solids **4**, 493 (1970).

[136] L. Muller and M. Muller, J. Non-Cryst. Solids **4**, 504 (1970).

[137] E.A. Fagen and H. Fritzsche, J. Non-Cryst. Solids **2**, 170 (1970).

[138] H.J. de Wit and C. Crevecoeur, J. Non-Cryst. Solids **8-10**, 787 (1972).

[139] D. K. Reinhard, D. Adler, and F.O. Arntz, J. Appl. Phys. **47**, 1560 (1976).

[140] S. D. Savransky and I. V. Karpov, (Intel Corporation, 2008).

[141] W. D. Buckley and S. H. Holmberg, Solid State Electron. **18**, 127 (1975).

[142] M. P. Shaw, S. H. Holmberg, and S. A. Kostylev, Phys. Rev. Lett. **31**, 542 (1973).

[143] R. R. Shanks, J. Non-Cryst. Solids **2**, 504 (1970).

[144] I. Balberg, Appl. Phys. Lett. **16**, 491 (1970).

[145] K. E. Petersen and D. Adler, J. Appl. Phys. **47**, 256 (1976).

[146] R. W. Pryor and H. K. Henisch, J. Non-Cryst. Solids **7**, 181 (1972).

[147] T. Gotohoh, K. Sugawara, and K. Tanaka, Jpn. J. Appl. Phys. **43**, L818 (2004).

[148] F. Rao, Z. Song, Y. Gong, L. Wu, B. Liu, S. Feng, and B. Chen, Appl. Phys. Lett. **92**, 223507 (2008).

[149] A. V. Kolobov, Phys. Rev. Lett. **97**, 035701 (2006).

[150] K. E. Petersen and D. Adler, Appl. Phys. Lett. **25**, 211 (1974).

[151] H. K. Henisch and R. W. Pryor, Solid-State Electron. **14**, 765 (1971).

[152] D. R. Haberland and H. P. Kehrer, Solid-State Electron. **13**, 451 (1970).

[153] A. Pirovano, A. L. Lacaita, F. Pellizzer, S. A. Kostylev, A. Benvenuti, and R. Bez, IEEE Trans. Electron Devices **51**, 714 (2004).

[154] U. Russo, D. Ielmini, and A. L. Lacaita, in *Proceedings of the 45th Annual International Reliability Physics Symposium* (IEEE, Pheonix, 2007).

[155] D. L. Thomas and J. C. Male, J. Non-Cryst. Solids **8-10**, 522 (1972).

[156] A. C. Warren, Electron. Lett. **5**, 461 (1969).

[157] A. V. Kolobov, P. Fons, Anatoly I. Frenkel, A. L. Ankudinov, J. Tominaga, and T. Uruga, Nature **3**, 703 (2004).

[158] D. A. Baker, M. A. Paesler, G. Lucovsky, S. C. Agarwal, and P. C. Taylor, Phys. Rev. Lett. **96**, 255501 (2006).

[159] 1. N. Yamada and T. Matsunaga, J. Appl. Phys. **88**, 7020 (2000).

[160] W. K. Njoroge, J. Vac. Sci. Technol. **A20**, 230 (2002).

[161] K. Shportko, S. Kremers, M. Woda, D. Lencer, John M. Robertson, and M. Wuttig, Nature Materials Advance Online Publication (2008).

[162] T. C. Chong, L. P. Shi, X. Q. Wei, R. Zhao, H. K. Lee, P. Yang, and A. Y. Du, Phys. Rev. Lett. **100**, 136101 (2008).

[163] M. H. Cohen, R. G. Neale, and A. Paskin, J. Non-Cryst. Solids **8-10**, 885 (1972).

[164] T. Matsunaga and N. Yamada, Jpn. J. Appl. Phys. **43**, 4704 (2003).

[165] X. Wei, S. Luping, T. C. Chong, Z. Rong, and L. H. Koon, Jpn. J. Appl. Phys. **46**, 2211 (2007).

[166] A. Pirovano, A. L. Lacaita, A. Benvenuti, F. Pellizzer, S. J. Hudgens, and R. Bez, IEEE IEDM Tech. Dig., 2003, p. 29.6.1-29.6.4.

[167] H. Fritzsche and S. R. Ovshinsky, J. Non-Cryst. Solids **2**, 148 (1970).

[168] D. H. Kang, D. H. Ahn, K.B. Kim, J. F. Webb, and K. W. Yi, J. Appl. Phys. **94**, 3536 (2003).

[169] J. A. Copeland, IEEE Trans. Electron. Devices **ED18**, 50 (1971).

Appendix A

Survey of Experimental Results and Parameter Values for Threshold Switches and Phase Change Memory

The following appendix provides a broad range of experimental results and properties related to chalcogenide threshold switches and phase change memory devices. The first part is a list of experimental observations with references to the associated publications. The device thickness is less than 10 μm unless noted otherwise. In many cases, conflicting results are shown that are representative of some uncertainty in the properties of these materials. Each observation should be considered in the context of the published work that is cited. A table of typical parameter values is also provided in Table A.1.

OFF STATE:

1. OFF state current I_{off} is exponentially dependent on voltage above some critical field and is ohmic below that field, $I_{off} \propto \exp(V)$ or $\exp(\sqrt{V})$. [105, 110, 119, 134, 135, 136]

2. There are two distinct regions of exponential voltage dependence when $T < 200$ K and for As_2Se_3 at $T < 400$ K. [137, 138]

3. OFF state current depends exponentially on the square of voltage for As_2Te_3, indicative of space charge limited currents, $I_{off} \propto \exp(V^2)$. [135]

4. OFF state current is thermally activated, $I_{off} \propto \exp(-E_a/kT)$. [5]

5. OFF state current is proportional to device area, $I_{off} \propto A$. [5]

6. Hole dominated current in the off state. [139]

7. Resistivity obeys the Meyer-Neldel rule. [140]

8. Current leakage is via grain boundaries. [108]

SWITCHING:

9. Threshold voltage V_{th} is linearly dependent on device thickness d and the threshold field E_{th} does not depend on d, $V_{th} \propto d$. [12, 105, 110, 111, 112, 113]

10. Threshold field E_{th} decreases and becomes dependent on device thickness d for long voltage pulse times ($t > 1$ μs). [141, 142]

11. Threshold voltage V_{th} depends on the square root of device thickness d for $d > 100$ μm, $V_{th} \propto \sqrt{d}$. [113]

12. Threshold voltage V_{th} decreases slowly with increasing temperature, for $T > 200$ K. [110, 111]

13. Threshold voltage V_{th} decreases linearly with temperature, $V_{th} \propto -\beta T$. [134]

14. Threshold voltage V_{th} decreases by 0.7% per °C. [110, 111]

15. Threshold voltage V_{th} depends on the inverse square root of temperature for thicker devices, $V_{th} \propto T^{-1/2}$. [120]

16. Threshold voltage V_{th} depends on the inverse cube root of temperature for modern devices, $V_{th} \propto T^{-3/2}$. [12]

17. Threshold voltage V_{th} does not depend on illumination even though conductivity changes by an order of magnitude (qualitatively, all models assume that the transition starts at an electrode where light related effects are minimal). [112]

18. Threshold voltage V_{th} decays exponentially as applied pressure P increases, $V_{th} \propto \exp(-P)$. [134]

19. Threshold voltage V_{th} is statistically distributed under ac [105, 125] and dc bias. [15]

20. Switching occurs at applied voltage V less than the threshold voltage after a sufficient delay time t_d (referred to as "under-threshold"switching). [15]

21. Threshold voltage V_{th} does not depend on electrode material. [105]

22. Delay time t_d exponentially decreases as applied voltage increases when the applied voltage is below V_{th} or at low over-voltage, $t_d \propto \exp(1/V)$. [13]

23. Delay time t_d exponentially decays as voltage increases for high over-voltage in thin films, $t_d \propto \exp(-V)$. [113]

24. Delay time t_d depends on the inverse square of voltage for low over-voltage in thin films and for any over-voltage in bulk samples ($d > 100$ μm). [113]

25. Delay time t_d depends on the inverse square root of the voltage at low over-voltage for thick films ($d > 100$ μm), $t_d \propto (V - V_{th})^{-1/2}$. [120, 134]

26. Delay time t_d fluctuates statistically [15, 105] for applied voltage $V < 1.2V_{th}$ and is constant for higher voltages. [141, 142]

27. Delay time t_d depends on the square of device thickness for low over-voltage in thin and thick films, $t_d \propto d^2$. [113]

28. Delay time t_d decays exponentially as temperature increases, $t_d \propto \exp(1/T)$. [13]

29. Delay time t_d depends on applied electric field and temperature according to $t_d \propto \exp[W(E)/kT]$ for applied voltage $V < V_{th}$, where $W(E)$ is the field-dependent minimum nucleation barrier. [15]

30. Delay time t_d does not depend on polarity of applied bias. [143, 144]

31. Delay time t_d is reduced by a pre-bias that is less than V_{th} and the effect is independent of the polarity of the pre-bias. [143]

32. There is a maximum benign interruption time $t_{sm} \sim 0.2 - 1.2$ μs during which only the holding voltage V_h is required to restore the ON state. [10, 104, 145, 146]

33. Maximum benign interruption time t_{sm} is proportional to the ON state current I_{on} and it increases with device thickness d, $t_{sm} \propto I_{on}$. [10, 146]

34. Effective capacitance becomes negative just before threshold. [134]

35. Crystalline embryos disappear with field removal unless they exceed a certain minimum size. [147]

36. Main cause of phase transition is power dissipated in the bulk and interface rather than Joule heating from the bottom electrode. [128]

37. Intermediate resistance states can be produced by applying short duration voltage pulses. [13]

38. Switching occurs at $T \approx 460$ K without any applied bias. [148]

39. Cubic GST starts to amorphize at pressures above 10 GPa and amorphization occurs at around 20 GPa at room temperature. [149]

ON STATE:

40. ON state current density is constant, $J_{on} = const(V)$, hence the ON state current I_{on} is proportional to the filament area A_f, $I_{on} \propto A_f$. [105, 145, 143, 150]

41. ON state current I_{on} is not disturbed when the polarity of the applied voltage is reversed. [151]

42. ON state current I_{on} is exponentially dependent on the applied pressure P, $I_{on} \propto \exp(P)$. [134]

43. Diameter of the current-carrying filament/channel is greater than device thickness $d \sim 1$ μm (for earlier devices), $2r_f > d$. [145, 150]

44. Current-carrying filaments are narrow and form homogeneous clusters (for modern PCM devices), $r_f \sim 10$ nm. [108]

45. Conductive filament constricts near the electrodes (for $d > 100$ μm). [120, 152]

46. Holding voltage V_h is about the same magnitude as the optical band gap E_g; approx. 10% of E_g variation is in the bulk and most of the voltage drop is at the electrodes, $V_h \approx E_g$. [145, 150]

47. Holding voltage V_h is weakly dependent on device thickness d. [119, 105]

48. Holding voltage V_h is directly proportional to the device thickness d for $d > 100$ μm, $V_h \propto d$. [120]

49. Holding voltage V_h depends on electrode material and is asymmetric with asymmetric electrode configurations. [146]

50. Holding voltage V_h is practically independent of temperature T [119], but diminishes with increasing T. [146]

51. Holding current I_h decreases slightly as temperature T increases. [119]

52. Holding current I_h depends on the frequency of applied voltage, while the holding voltage V_h does not. [7]

53. Both electrons and holes contribute to ON state current but slightly electron dominated. [145, 150]

54. Optical band gap E_g is not substantially reduced in the ON state. [6, 104, 139]

55. ON state resistivity ρ_c obeys the Meyer-Neldel rule. [140]

NOISE:

56. $1/f$ noise in the OFF state is 2 orders of magnitude greater than in the ON state. [60]

57. Low-frequency noise increases exponentially with the applied voltage in both amorphous and crystalline GST. [60]

RELAXATION OSCILLATIONS:

58. Period of oscillation T_{osc} has a power dependence on the series resistance R_s in the circuit, $T_{osc} \propto R_s^a$, $a > 1$. [125]

59. Period of oscillation T_{osc} has a nonuniform statistical distribution. [125]

60. Period of oscillation T_{osc} becomes infinite at an upper limiting value of R_s. [125]

61. Minimum amplitude of the oscillating current increases with time. [126]

62. Period of oscillation T_{osc} decreases with increasing applied voltage. [122]

63. Period of oscillation T_{osc} is independent of T_{off}, time between RESET and SET pulses. [122]

DRIFT:

64. Threshold voltage V_{th} increases with time, $V_{th}(t) = V_{th}(t_0)[1+\nu \ln(t/t_0)]$, where ν is the drift coeffecient and t is the time after the RESET pulse. V_{th} eventually saturates for samples that are annealed at $T > 300$ K. [123]

65. OFF state resistance increases with time $R_{off}(t) = R_0(t/t_0)^{\alpha}$, $0.03 < \alpha < 0.01$, where t is the time after RESET pulse. R_{off} eventually saturates for samples that are annealed at $T > 300$ K. [123], $\alpha = 0.06$ in Ref. [153]

66. Threshold voltage V_{th} and OFF state resistance R_{off} saturate at $t \sim 10^4$ s for $T \sim 75$ °C, and $t \sim 10^7$ s at room temp. [123]

67. Data retention fails after a time t_{fail} - time to failure exponentially decreases as temperature increases, $t_{fail} \propto \exp(E_a/kT)$, with $E_a \sim 2.5$ eV. [154]

68. Statistical variation of t_{fail} increases with temperature. [154]

69. Current creep observed over times greater than the delay time ($t \gg t_d$) at low T negative current creep near the threshold voltage V_{th}, positive creep far below V_{th}. [7]

STRUCTURAL/MISCELLANEOUS:

70. I/V curve is symmetric in reversal of applied voltage. [105]

71. $Te_{48}As_{30}Si_{12}Ge_{10}$ exhibits threshold switching only, reducing As to 5% results in memory switching. [105]

72. Channel is not hot enough for thermal effects to dominate. [155, 156]

73. Crystal to amorphous phase change process does not require the rupture of strong covalent bonds and the transition is diffusionless. [157]

74. Entropy effects in non-crystalline and enthalpy effects the crystalline phase combine to make amorphous-crystalline phase change favorable [158]

75. Crystalline phase has the structure of rock salt (NaCl). [159]

76. Amorphous phase is locally more ordered than the crystalline phase and the germanium atoms switch from octahedral (crystalline) to tetrahedral (amorphous) coordination. [157]

77. Density of amorphous state is 5% to 10% lower than crystalline state. [160]

78. Activation energy for crystal growth increases with increasing germanium content. [133]

79. Several PCMs showed a reduced glass transition temperature T_R between 0.5 and 0.55, where $T_R = T_G/T_M$ with T_G the glass transition temperature and T_M the melting temperature. [133]

80. Dielectric constant is $70-200\%$ greater in crystalline phase may be due to resonant bonding which results in a higher concentration of delocalized electrons. [161]

81. Intermediate states (between ON and OFF) observed in amorphous/crystalline superlattices (layered materials) with thickness dependent properties. [162]

82. Crystalline growth appears to be dendritic. [163]

83. Crystal phase contains up to 25 atomic % vacancies. [164]

84. Crystallization temperature increases exponentially with decrease in device thickness for device thickness less than 20nm. Crystallization speed decreases with decreasing film thickness. [165]

Table A.1: Typical parameter values for phase change memory and threshold switches. a-GST and c-GST denote amorphous and crystalline GST, respectively and '*' denotes results specific to modern PCM devices.

Parameter		**Value**	**References**
C_{sa}	specific heat of a-GST	10^6 J m^{-3} K^{-1}	[120]
C_{sc}	specific heat of c-GST	10^6 J m^{-3} K^{-1}	[120]
E_{gopt}	opt. band gap	0.5 - 1.1 eV	[139, 104]
	of amorphous phase	0.7 eV	[104]
	of cubic and hexagonal	0.5 eV	[104]
E_{th}	threshold electric field	3×10^5 V/cm	[105]
I_h	holding current	0.06 - 2.0 mA	[119]
I_{set}	SET program current	1 - 1.7 mA	[128]*
J_{on}	ON current density	10^3 - 10^4 A/cm^2	[145]
		7×10^4 A/m^2	[108]
J_{off}	OFF current density	1.2×10^7 A/m^2	[108]
N_t	trap concentration	$> 10^{19}$ cm^{-3} eV^{-1}	[105]
r_f	filament radius	2 - 25 μm	[145]
		50 μm	[105]
R_{off}	OFF resistance	0.3 - 3 kΩ	[119]
R_{on}	ON resistance	< 10 kΩ	[119, 122]

Continued...

Table A.1: (continued)

Parameter		**Value**	**References**
R_{set}	SET resistance	10^3 - 10^4 Ω	[21]*
R_{reset}	RESET resistance	10^5 - 10^6 Ω	[21]*
t_0	switching time	1.5×10^{-10} s	[105]
t_d	delay time	< 10 μs	[105, 142]
			[145, 146]
t_{sm}	max benign interrupt time	0.2-1.2 μs	[145, 104]
V_h	holding voltage	1 - 20 V	[119]
		0.3 V	[21]*
V_{th}	threshold voltage	10 - 100 V	[105]
		1 V	[21]*
ε_{th}	threshold electric field	$0.8 - 8 \times 10^5$ V/cm	[119, 145]
κ_a	thermal cond. a-GST	0.002 W cm^{-1} K^{-1}	[166]
κ_c	thermal cond. c-GST	0.005 W cm^{-1} K^{-1}	[166]
μ_b	band mobility	10 cm^{-2} V^{-1} s^{-1}	[6]
μ_p	hole drift mobility (OFF)	2×10^{-5}cm^{-2}V^{-1}s^{-1}	[104]
$\mu\tau$	mobility-lifetime	3×10^{-9} cm^2/V	[104]
ρ_a	resistivity a-GST	$10^5 - 10^8$ Ω cm	[7, 167]
		10^3 Ω cm	[140]*
ρ_c	resistivity c-GST	< 10 Ω cm	[167]
		0.08 Ω cm	[145]
		0.02 Ω cm	[140]*
		$0.4 - 1$ Ω cm	[148]

Continued...

Table A.1: (continued)

Parameter		**Value**	**References**
E_{aa}	activation energy a-GST	0.37 eV	[140]*
E_{ac}	activation energy c-GST	0.09 eV	[140]*
T_M	GST melting point	900 K	[168]
T_G	GST glass transition temp.	460 K	[148]

Appendix B

Derivations Related to $1/f$ Noise

B.1 Double Well Potentials: Mobility Modulation

The spectral properties of the noise for a system of charged particles can be described by the correlation function

$$S_j(\omega) = \langle (\delta j)^2 \rangle_\omega = \langle j \rangle^2 \frac{2\pi\alpha}{N\omega}, \tag{B.1}$$

where δj is the fluctuating part of the current density, the subscript ω indicates the Fourier transform, $\langle j \rangle$ is the average current density, N is the number of charge carriers, and ω is the radial frequency.

Our starting point is the Boltzmann equation for non-equilibrium transport

$$\frac{\partial F_{\mathbf{p}}}{\partial t} + \dot{\mathbf{q}} \cdot \frac{\partial F_{\mathbf{p}}}{\partial q} + \dot{\mathbf{p}} \cdot \frac{\partial F_{\mathbf{p}}}{\partial p} = \left. \frac{\partial F_{\mathbf{p}}}{\partial t} \right|_{\text{coll}}, \tag{B.2}$$

where $F_{\mathbf{p}}$ is the distribution function for the electrons of momentum $\mathbf{p}$, position $\mathbf{q}$, velocity $\dot{\mathbf{q}}$ and force $\dot{\mathbf{p}}$; t is time. The collision term on the right hand side contains most of the physics specific to a given system. Here we will consider only the current carrying part of the Boltzmann equation and denote the collision term

by I. Therefore, Eq. (B.2) reduces to

$$e\mathbf{E}\cdot\frac{\partial F_{\mathbf{p}}}{\partial \mathbf{p}} = I. \tag{B.3}$$

The collision term takes the standard form

$$I = \sum_{\mathbf{p}'i}\left[W^i_{\mathbf{p}\mathbf{p}'}F_{\mathbf{p}}(1-F_{\mathbf{p}'}) - W^i_{\mathbf{p}'\mathbf{p}}F_{\mathbf{p}'}(1-F_{\mathbf{p}})\right], \tag{B.4}$$

where the sum is over all final momenta and each scattering center i.

We conjecture that some fraction of the scattering centers are DWP which can cause two possible scattering scenarios depending on the atomic configuration at the time of scattering. The transition rate at a DWP site is therefore split into two possibilities given by

$$W^i_{\mathbf{p}\mathbf{p}'} = n^i_1 W^{i1}_{\mathbf{p}\mathbf{p}'} + \left(1-n^i_1\right)W^{i2}_{\mathbf{p}\mathbf{p}'}, \tag{B.5}$$

where $W^{i1}_{\mathbf{p}\mathbf{p}'}$ is the transition rate due to the atom being in state 1, and the probability that the atom is in state 1 or 2 is given by n_1 and $n_2 = 1-n_1$, respectively. The occupancy probabilities, n_1 and n_2, of each DWP site varies with time and can be characterized by $n^i_1 = \bar{n}^i_1 + \delta n^i_1$ where $\bar{n}^i_1$ is the mean occupation probability of state 1 and δn^i_1 is the variation of that probability. With this in mind, and by applying Eq. (B.5) as well as the fact that for elastic scattering $W^i_{\mathbf{p}\mathbf{p}'} = W^i_{\mathbf{p}'\mathbf{p}}$, Eq. (B.4) becomes

$$I = \sum_{\mathbf{p}'i}\widetilde{W}^i_{\mathbf{p}\mathbf{p}'}(F_{\mathbf{p}} - F_{\mathbf{p}'}) + (W^{i1}_{\mathbf{p}\mathbf{p}'} - W^{i2}_{\mathbf{p}\mathbf{p}'})(F_{\mathbf{p}} - F_{\mathbf{p}'})\delta n^i_1, \tag{B.6}$$

where $\widetilde{W}^i_{\mathbf{p}\mathbf{p}'} = \bar{n}^i_1 W^{i1}_{\mathbf{p}\mathbf{p}'} + \bar{n}^i_2 W^{i2}_{\mathbf{p}\mathbf{p}'} + W^i_{\mathbf{p}\mathbf{p}'} \approx W^i_{\mathbf{p}\mathbf{p}'}$. The first term in the summation of Eq. (B.6) represents the constant part of the collision term I_0 and the second term represents the fluctuating part δI.

In the relaxation time approximation, the collision term in Eq. (B.2) is replaced

by $-(F_{\mathbf{p}} - F_{\mathbf{p}0})/\tau$, where τ is an average relaxation time. This implies that, if left unperturbed, the distribution function will relax to the equilibrium distribution function after a time τ. Inserting the relaxation time approximation to Eq. (B.3) yields

$$F_{\mathbf{p}} = -\tau e\mathbf{E}\cdot\mathbf{v}\frac{\partial F_{\mathbf{p}}}{\partial \epsilon}, \tag{B.7}$$

where $\mathbf{v}$ is the velocity of the electron and ϵ its energy. Given Eq. (B.6) and the fact that,

$$\sum \mathbf{p}' = \frac{V}{(2\pi\hbar)^3}\int d\mathbf{p}', \tag{B.8}$$

where $[V/(2\pi\hbar)^3]^{-1}$ is a volume of momentum space (we neglect the factor of 2 associated with 2 spin states), the constant part of the collision term becomes

$$I_0 = \frac{V}{(2\pi\hbar)^3}\int d\mathbf{p}' W_{\mathbf{p}\mathbf{p}'}\tau e(\mathbf{E}\cdot\mathbf{v} - \mathbf{E}\cdot\mathbf{v}')\frac{\partial F_{\mathbf{p}}}{\partial \epsilon}. \tag{B.9}$$

By introducing the angle variables $\angle(\mathbf{v},\mathbf{E}) = \phi, \angle(\mathbf{v}',\mathbf{E}) = \alpha$, and $\angle(\mathbf{v},\mathbf{v}') = \vartheta$ we see that the transition probability becomes a function of the scattering angle, $W_{\mathbf{p}\mathbf{p}'} = W_{\mathbf{p}\mathbf{p}'}(\vartheta)$ and that $\cos\alpha = \cos\vartheta\cos\phi + \sin\vartheta\sin\phi\cos\varphi$, where φ is the angle between the planes $(\mathbf{v},\mathbf{E})$ and $(\mathbf{v},\mathbf{v}')$. Integrating over the direction of $\mathbf{p}'$ with the angle φ measured from the plane $(\mathbf{v},\mathbf{E})$ we obtain

$$\int d\mathbf{p}(\mathbf{E}\cdot\mathbf{v}') = \int d\mathbf{p} Ev\cos\vartheta\cos\phi = \int d\mathbf{p}\mathbf{E}\cdot\mathbf{v}\cos\vartheta. \tag{B.10}$$

Inserting Eqs. (B.7) and (B.10) into (B.9) yields

$$I_0 = \sum_{p'} W_{\mathbf{p}\mathbf{p}'}(\vartheta)(1-\cos\vartheta)F_{\mathbf{p}} \equiv \frac{F_{\mathbf{p}}}{\tau}, \tag{B.11}$$

where

$$\frac{1}{\tau} \equiv \sum_{\mathbf{p}'} W_{\mathbf{p}\mathbf{p}'}(1-\cos\vartheta), \tag{B.12}$$

represents the transport relaxation time.

DWP change the distribution function by a small amount $F_{DWP} \ll F_{\mathbf{p}}$. Using F_{DWP} as a perturbation in the constant part of the collision term and recalling Eq. (B.6) gives the following form of the Boltzmann equation:

$$e\mathbf{E} \cdot \frac{\partial F_{\mathbf{p}}}{\partial \mathbf{p}} = -\frac{F_{\mathbf{p}} + F_{DWP}}{\tau} + \sum_{\mathbf{p}',i} (W^{i1}_{\mathbf{p}\mathbf{p}'} - W^{i2}_{\mathbf{p}\mathbf{p}'})(F_{\mathbf{p}} - F_{\mathbf{p}'})\delta n^i_1. \tag{B.13}$$

For the relaxation time approximation to hold the second term and the summation on the right hand side of Eq. (B.13) must cancel each other, which implies that

$$F_{DWP} = \tau \sum_{\mathbf{p}',i} (W^{i1}_{\mathbf{p}\mathbf{p}'} - W^{i2}_{\mathbf{p}\mathbf{p}'})(F_{\mathbf{p}} - F_{\mathbf{p}'})\delta n^i_1. \tag{B.14}$$

Given the distribution functions one can calculate the constant part j_0 and fluctuating part δj of the current density j using

$$j_0 = \sum_{\mathbf{p}} ev F_{\mathbf{p}} \quad \text{and} \quad \delta j = \sum_{\mathbf{p}} ev F_{DWP}, \tag{B.15}$$

where v is the electron mean velocity. Inserting Eq. (B.14) into δj of Eq. (B.15) and replacing $W_{\mathbf{p}\mathbf{p}'}$ with the standard transition rate for an energy conserving transition yields

$$\begin{aligned} &\sum_{\mathbf{p},\mathbf{p}',i} e\tau v \frac{2\pi}{\hbar} \left[|\langle p|H^{i1}|p'\rangle|^2 - \langle p|H^{i2}|p'\rangle|^2 \right] \times \\ &\delta\left(\epsilon_{\mathbf{p}} - \epsilon_{\mathbf{p}'}\right)\left(F_{\mathbf{p}} - F_{\mathbf{p}'}\right)\delta n^i_1. \end{aligned} \tag{B.16}$$

In these matrix elements, the wave functions are normalized to the volume. However, we require a normalization where $W_{\mathbf{p}\mathbf{p}'}$ has the dimension of area, which is given by

the wave functions [55]

$$\widetilde{\psi}_{\mathbf{p}'} = \exp \frac{i}{\hbar}\mathbf{p}' \cdot \mathbf{r} \quad \text{and} \quad \widetilde{\psi}_{\mathbf{p}} = \frac{1}{\sqrt{v}} \exp \frac{i}{\hbar}\mathbf{p} \cdot \mathbf{r}, \tag{B.17}$$

where v is the velocity. So the former is normalized by the delta function of $\mathbf{p}/(2\pi\hbar)$, while the latter is normalized to the current density for the impeding wave. Therefore, Eq. (B.16) becomes

$$\sum_{\mathbf{p},\mathbf{p}',i} e\tau \frac{v^2}{V^2} \frac{2\pi}{\hbar} \left[|\langle p|H^{i1}|p'\rangle|^2 - \langle p|H^{i2}|p'\rangle|^2 \right] \times \delta\left(\epsilon_{\mathbf{p}} - \epsilon_{\mathbf{p}'}\right) (1 - \cos\varphi) F_{\mathbf{p}} \delta n_1^i, \tag{B.18}$$

where the term $(1 - \cos\varphi) F_{\mathbf{p}}$ was derived in Eq. (B.11). Next, we take into account that $\delta\left(\epsilon_{\mathbf{p}} - \epsilon_{\mathbf{p}'}\right) = \delta(p^2 - p'^2)2m$ and replace

$$\sum_{\mathbf{p}'} \rightarrow \frac{V}{(2\pi\hbar)^3} 2m \int \frac{1}{2} p' d\left(p'^2\right) d\Omega' \delta(p^2 - p'^2), \tag{B.19}$$

where $d\Omega'$ is the elemental solid angle. The integration over p'^2 then amounts to replacing p' by p in the integrand and we obtain

$$\sum_{\mathbf{p},i} \frac{e\tau v^2}{V} \int \frac{mp}{4\pi^2\hbar^4} \left[|\langle p|H^{i1}|p'\rangle|^2 - \langle p|H^{i2}|p'\rangle|^2 \right] (1 - \cos\varphi)\, d\Omega' F_{\mathbf{p}} \delta n_1^i. \tag{B.20}$$

We now take into account the expression for the differential cross section

$$d\sigma = \frac{mp}{4\pi^2\hbar^4} \left| \int \widetilde{\psi}^*_{\mathbf{p}'} H \widetilde{\psi}_{\mathbf{p}} d\mathbf{r} \right|^2 d\Omega', \tag{B.21}$$

in the Born approximation and the definition of the transport cross section [55]

$$\sigma_{tr} = \int (1 - \cos\vartheta)\, d\sigma. \tag{B.22}$$

Combining Eqs. (B.21) and (B.22) with the expression for the constant part of the current density in Eq. (B.15) reduces Eq.(B.20) to

$$\delta j = j_0 \frac{l}{V} \sum_i \left(\sigma_{tr}^{i1} - \sigma_{tr}^{i2}\right) \delta n_1^i, \tag{B.23}$$

where we have used $\tau v = l$, where l is the mean free path. The only time dependent factor in Eq. (B.20) is the variation of the occupancy probability δn_1^i of the DWP. Consequently, the correlation function of Eq. (B.1) is given by

$$S_j(\omega) = \langle (\delta j)^2 \rangle_\omega = j_0^2 \left(\frac{l}{V}\right)^2 \sum_i \left(\sigma_{tr}^{i1} - \sigma_{tr}^{i2}\right)^2 \langle \left(\delta n_1^i\right)^2 \rangle_\omega. \tag{B.24}$$

Next we consider the kinetics of the occupation probability of a single well in a DWP. If P_{12} represents the transition rate from well 1 to well 2 and P_{21} represents the opposite transition rate, then in the thermal equilibrium, the time dependence of the variation in the occupation probability can be expressed

$$\delta n_1^i(t) = \delta n_1^i(0) \exp\left(\frac{-t}{\tau_i}\right), \tag{B.25}$$

where τ_i is the characteristic transition time given by $\tau_i = (P_{12}^i + P_{21}^i)^{-1}$. According to the binomial distribution, the dispersion of the first factor in Eq. (B.25) is given by the product of the means, $\bar{n}_1^i \bar{n}_2^i$. Combining this with the Fourier transform of the second factor yields the correlation function

$$\langle \left(\delta n_1^i\right)^2 \rangle_\omega = \frac{\bar{n}_1^i \left(1 - \bar{n}_1^i\right)}{\omega^2 + \tau_i^{-2}} \frac{1}{\tau_i}. \tag{B.26}$$

Inserting Eq. (B.26) into Eq. (B.24) finally results in

$$S_j(\omega) = j_0^2 \frac{l^2}{V^{2/3}} \sum_i G_i \frac{\tau_i}{1 + (\omega\tau_i)^2}, \tag{B.27}$$

where

$$G_i = \left(\sigma_1^i - \sigma_2^i\right)^2 \bar{n}_1^i \left(1 - \bar{n}_1^i\right) V^{-4/3} \tag{B.28}$$

is the "strength" of the i^{th} fluctuator.

In order to complete the summation over i we specify the results for the DWP model in the high temperature regime of activation over, rather than tunneling through, the barrier which separates the two wells. If the two local minima of the potential vary by an asymmetry energy E, then the occupation probability for one well is given by

$$\bar{n}_1 = \frac{\exp\left(-E/2kT\right)}{\exp\left(-E/2kT\right) + \exp\left(E/2kT\right)}, \tag{B.29}$$

where T is the temperature and k is Boltzmann's constant. A DWP is further characterized by the height of the barrier W_B between the wells. The characteristic transition time τ is a function of the barrier height, $\tau = \tau_0 \exp\left(W_B/kT\right)$. To complete the analysis of Eq. (B.27) the discrete sum is converted to an integral by defining a probability density of the DWP as a function of asymmetry energy E and time τ.

The probability distribution has the form given in Eqs. (4.2) and (4.7),

$$\rho(E, \tau) = \frac{P}{\tau}, \tag{B.30}$$

We also assume that $\sigma_1^i - \sigma_2^i = \Delta\sigma = const.$ With this in mind, inserting Eqs. (B.28),

(B.29) and (B.30) into Eq. (B.27) yields

$$S_j(\omega) = j_0^2 \frac{l^2}{V} \frac{P}{4} (\Delta\sigma)^2 \times \int_0^{E_{max}} \int_{\tau_{min}}^{\tau_{max}} dE d\tau \frac{1}{(1+\omega^2\tau^2)\left(\cosh\frac{E}{2kT}\right)^2}. \tag{B.31}$$

Evaluating the integral of Eq. (B.31) with the standard DWP model assumptions of $E_{max} \gg kT$, $\omega\tau_{min} \ll 1$, and $\omega\tau_{max} \gg 1$ results in

$$S_j(\omega) = j_0^2 \frac{\pi}{4} (l\Delta\sigma)^2 \frac{PkTn_c}{N_e} \frac{1}{\omega}, \tag{B.32}$$

where the volume has been replaced by $V = n_c/N_e$ with n_c and N_e the concentration and number of electrons, respectively. Comparing Eq. (B.32) to Eq. (B.1) provides the following expression for the Hooge parameter,

$$\alpha = \frac{PkTn_c (l\Delta\sigma)^2}{8}. \tag{B.33}$$

B.2 Double Well Potentials: Modulation of Carrier Concentration

Here we consider in more detail the effect of DWP on modulating electron energy levels in the mobility gap. The modulation of these energy levels causes fluctuations in their occupation number and in the free carrier concentration. We start with the kinetic equation for a group of energy levels in a narrow energy interval ΔE,

$$\frac{d\Delta N_f}{dt} = -\Delta N_f N_{eff} \gamma_e + (\Delta N - \Delta N_f) n \gamma_c \tag{B.34}$$

where ΔN_f is the concentration of filled levels and N_{eff} is the effective density of states in the valence (conduction) band. The transition coefficients γ_c and γ_e exhibit temporal fluctuations $\delta\gamma_c$ and $\delta\gamma_e$ caused by the energy level modulation $E \to E+\delta E$. We express the latter modulation as

$$\delta E = \sum_i D_i \delta n_1^{(i)} \tag{B.35}$$

where D_i and $\delta n_1^{(i)}$ are the coupling parameter and the occupation numbers of ith DWP, and summation over all DWP is implied.

Taking into account that

$$\gamma_c = \gamma_0 \exp(-E/\varepsilon), \quad \gamma_e = \gamma_0 \exp[-E(1/\varepsilon + 1/kT)]$$

the corresponding fluctuations become

$$\delta\gamma_c = (\gamma_c/\varepsilon) \sum_i D_i \delta n_1^{(i)}, \quad \delta\gamma_e = \gamma_e(1/\varepsilon + 1/kT) \sum_i D_i \delta n_1^{(i)}. \tag{B.36}$$

Linearizing Eq. (B.34) with respect to fluctuations $\delta\gamma_c$, $\delta\gamma_c$, and δN_f yields

$$\frac{d\delta N_f}{dt} + \frac{\delta N_f}{\tau} = -\Delta N_f N_{eff} \delta\gamma_e + (\Delta N - \Delta N_f) n \delta\gamma_c. \tag{B.37}$$

Implementing the equilibrium relation $\Delta N_f N_{eff} \gamma_e = (\Delta N - \Delta N_f) n \gamma_c$ and substituting expressions for $\delta\gamma$ from Eq. (B.36) gives the final kinetic equation

$$\frac{d\delta N_f}{dt} + \frac{\delta N_f}{\tau} = n(\Delta N - \Delta N_f)\gamma_c \sum_i \frac{D_i}{kT} \delta n_1^{(i)}. \tag{B.38}$$

Here the sum on the r.h.s. represents a random quantity. If Eq. (B.38) is written in the terms of a change per center, $(\delta N_f/\Delta N)$, then the latter sum represents the

effect of a random DWP environment on a given center.

Performing the Fourier transform yields,

$$(\delta N_f)_\omega = \frac{\tau n(\Delta N - \Delta N_f)\gamma_c}{1 + i\omega\tau} \sum_i \frac{D_i}{kT} \delta(n_1^{(i)})_\omega. \tag{B.39}$$

Taking into account the relationships

$$\tau_c = \frac{1}{\gamma_c n}, \quad \frac{\Delta N - \Delta N_f}{\tau_c} = \frac{\Delta N_f}{\tau_e} = \frac{\Delta N}{\tau_e + \tau_c} = \frac{\Delta N}{\tau_c}(1 - f),$$

and using

$$f(1 - f) = kT \frac{\partial f}{\partial E},$$

Eq. (B.39) can be written in the form

$$\frac{(\delta N_f)_\omega}{\Delta N} \equiv \delta f = \frac{\partial f}{\partial E}(\delta E)_\omega, \tag{B.40}$$

where δf is the change in the occupation number that is a maximum

$$(\delta f)_{\max} = \frac{(\delta E)_\omega}{4kT}$$

at $E = E_F$, and where we have introduced the Fourier transform of the effective energy fluctuation

$$(\delta E)_\omega = \frac{1}{1 + i\omega\tau} \sum_i D_i \delta(n_1^{(i)})_\omega. \tag{B.41}$$

Because the product $f(1 - f)$ is a sharp maximum of width kT at the Fermi energy, the concentration of significantly contributing electron centers can be estimated as

$$\Delta N_T \approx g(E_F)kT.$$

We then neglect the term $\omega\tau$ in the denominator reflecting the fact that the

electron states are relatively shallow and have rather short relaxation times; hence,

$$(\delta f)_{\max} = \sum_i \frac{D_i}{4kT} \delta(n_1^{(i)})_\omega. \tag{B.42}$$

The latter random quantity characterizes an arbitrary electron center with a given two-level system (TLS) pattern in its proximity.

The dispersion in the number of charged carriers localized on $\Delta N_T V$ electron centers is estimated as

$$\begin{aligned} \Delta N_T V \langle [(\delta f)_{\max}]^2 \rangle = \\ \Delta N_T V \sum_i \langle \left(\frac{D_i}{4kT} \right)^2 [\delta(n_1^{(i)})]_\omega^2 \rangle \approx \\ \Delta N_T V N_{TLS} R^3 \langle \left(\frac{D}{4kT} \right)^2 \rangle \langle [\delta(n_1^{(i)})]_\omega^2 \rangle, \end{aligned} \tag{B.43}$$

where we have introduced the average number of two-level-systems $N_{TLS}R^3$ in the volume of the localized electron wave function, and approximately decoupled the frequency dependent fluctuations in TLS occupation numbers from the static interaction parameters D_i.

The latter quantity is directly related to the dispersion in the number of charge carriers. Indeed, the above used condition $\omega\tau \ll 1$ means that important localized charge carriers are in the state of thermal equilibrium. Correspondingly, the change in the occupation number of the free carriers is by the factor $\exp(-E_F/kT)$ smaller than $\Delta N_T V \langle [(\delta f)_{\max}]^2 \rangle$. Its relative value, of primary interest here, is given by

$$\begin{aligned} \frac{\langle (\delta I)_\omega^2 \rangle}{I^2} &= \frac{\langle (\delta n)_\omega^2 \rangle}{n^2} \\ &= \frac{\Delta N_T N_{TLS} R^3}{N_{eff}^2 V} \langle \left(\frac{D}{4kT} \right)^2 \rangle \langle [\delta(n_1^{(i)})]_\omega^2 \rangle \end{aligned} \tag{B.44}$$

where we have expressed the average number of free carriers as $N_{eff} V \exp(-E_F/kT)$.

We use the already described procedure of averaging [see Eqs. (B.31), (B.32)]

$$N_{DWP}\langle[\delta(n_1^{(i)})]_\omega^2\rangle = \frac{\pi}{4}\frac{PkT}{\omega}.$$

As a result we get the $1/f$ noise spectrum in the form of

$$\frac{\langle(\delta I)_\omega^2\rangle}{I^2} = \frac{\pi}{4}D^2Pa^3g(E_F)\frac{\Delta\omega}{\omega V N_{eff}^2}. \tag{B.45}$$

Its corresponding Hooge parameter is given by

$$\alpha = \frac{D^2Pa^3g(E_F)n_c}{8N_{eff}^2}. \tag{B.46}$$

B.3 Generation-Recombination Noise

Following Ref. [169], a partial electric current fluctuation related to a group of trap levels of certain energy, is given by

$$\delta I = \frac{I}{n_c V}\nu \tag{B.47}$$

where ν is the average number of electron emissions from that level per unit time; the multiplier $I/(n_cV)$ gives the current per carrier whose average concentration in volume V is n_c.

Consider electron (hole) levels in a small energy interval ΔE. They can be treated as a monoenergetic level of concentration $\Delta N(E) = g(E)\Delta E$. Let ΔN_f be the equilibrium concentration of filled energy levels in that same interval. It is determined by the balance equation

$$\frac{\Delta N_f}{\tau_e} = \frac{\Delta N - \Delta N_f}{\tau_c} \tag{B.48}$$

where τ_e is the time constant for emission from a filled level, and τ_c is the time

constant for the capture by an empty level.

A useful relationship between τ_e and τ_c follows when the corresponding rates are written as $\Delta N_f N_{eff}\gamma_e$ and $(\Delta N - \Delta N_f)n_c\gamma_c$, respectively, where N_{eff} is the effective density of states in the valence (conduction) band. The coefficients γ_e, γ_c do not depend on the particle concentrations and their ratio $\gamma_e/\gamma_c = \exp(-E/kT)$ is found from the equilibrium relations $n_c/N_{eff} = \exp(-E_F/kT)$ and $\Delta N_f/(\Delta N - \Delta N_f) = \exp[(E - E_F)/kT]$. As a result

$$\tau_e/\tau_c = \exp[-(E_F - E)/kT],$$

which translates into

$$\tau = f\tau_c \quad \text{with} \quad f = \{1 + \exp[(E_F - E)/kT\}^{-1}. \tag{B.49}$$

If the concentration of filled levels is slightly perturbed from equilibrium by δN_f, it relaxes back to ΔN_f according to

$$\frac{d\delta N_f}{dt} = -\frac{\delta N_f}{\tau} \quad \text{with} \quad \frac{1}{\tau} = \frac{1}{\tau_e} + \frac{1}{\tau_c} \tag{B.50}$$

where t is time. The corresponding temporal dependence $\delta N_f \propto \exp(-t/\tau)$ translates into the current fluctuations caused by one trapping/detrapping event decaying similarly as

$$\delta I(t) = (I/n_c V)\nu \exp(-t/\tau).$$

Its frequency component is

$$\delta I(\omega) = 2\int_0^\infty \delta I(t)\exp(i\omega t)dt = \frac{2I\tau}{n_c V(1 + i\omega\tau)} \tag{B.51}$$

Since the average number of emissions per second is

$$\nu = \frac{\Delta N_f V}{\tau_e} = \frac{\Delta N V}{\tau_e + \tau_c}, \tag{B.52}$$

the relative partial noise spectrum becomes

$$\frac{\langle (\delta I)^2 \rangle}{I^2} = \nu \frac{(\delta I)^2}{I^2} = \frac{4\Delta N \tau^2}{n_c^2 V (\tau_e + \tau_c)(1 + \omega^2 \tau^2)}, \tag{B.53}$$

where the angle brackets indicate the Fourier transform. Integrating the latter result over the band tail spectrum yields Eq. (4.26).